

MECHANICAL CHARACTERIZATION OF DAMAGE AND FAILURE IN
POLYMERIC FOAMS AND GLASS/EPOXY COMPOSITES

Thesis by

Theresa Hiromi Kidd

In Partial Fulfillment of the Requirements for the
degree of

Doctor of Philosophy

CALIFORNIA INSTITUTE OF TECHNOLOGY

Pasadena, California

2006

(Defended [June 8, 2006])

© [2006]

[Theresa Kidd]

All Rights Reserved

To my wonderful family

Mom, Dad, Amy and Christian

ACKNOWLEDGEMENTS

It is to my great chagrin that I am not able to thank everyone who I have had the pleasure of knowing in my four years here at Caltech. These people have enriched my life and I am very grateful for the time they shared with me in an academic setting as well the time spent just having fun. Thanks to all of you for your time and friendship.

The people who I have to thank the most are my parents. Their unwavering love and support are why I have been able to achieve things that I never thought possible. My sister Amy has always been there for me and always encouraged me when I was feeling down. Her encouragement during the last few weeks of writing was the driving force in helping me to complete my dissertation. I also want to say thank you to my boyfriend, Christian, for bringing me snacks when I worked late and generally helping me to enjoy the time that I wasn't in the lab.

The person who first introduced me to experimental mechanics was Prof. Lambros at the University of Illinois. He was the one who put me on the path of pursuing my Ph.D. and for that I am eternally grateful.

The Aeronautics department's staff is comprised of the most helpful and friendly people you will ever meet. Denise Thobe, Cythia Garza, Dimity Nelson, Lydia Suarez and Donna Mojahedi were an immense help in learning how to work in GALCIT. On a personal note, without them I would have been perpetually locked out of my office. The machine shop has been an invaluable resource while doing my research at Caltech. Joe Haggerty, Brad St. John and Ali Kiani have gone to great lengths to get me the parts that I needed when I needed them, even when I came to them with a drawing at 4:30pm on a Friday. Petros Arakelian has been immensely helpful in conducting my experiments. He has helped me find parts that I needed and helped me assemble and disassemble my setups. His expertise and advice have helped me to learn about and utilize the wide variety of testing equipment in the GALCIT solid mechanics labs. A special mention must go to my two MURF students, Rita Suarez and Judy Cruz. Their help during my first two summers at Caltech is truly appreciated. Everyone in my research group at one time or another has

helped me in my research. Christian Franck, Winston Jackson, Sam Feakins, Dr. Min Tao, Dr. Shiming Zhang and Dr. Murat Vural have all graciously given their time, for which I am thankful. Dr. Soonsung Hong's expertise on optical measurement systems and advice on proper optical method techniques has been invaluable, and his help is acknowledged. Finally, I want to thank my two fellow inmates, Shannon Browne and Emilio Graff. Their camaraderie has helped me to survive at Caltech.

I have had the privilege of working with and taking classes from a wonderful group of Professors at Caltech. I would particularly like to thank Prof. Knauss for taking the time to edit some of my papers and teach me the importance of proper technical writing. Additionally, while working with him on several consulting projects, I learned how to identify the important parameters of an experiment and draw proper conclusions from data gathered. I believe these experiences have made me a better researcher. Prof. Shepherd has always been on hand when I needed help with anything from fundamental concepts to computer problems. I appreciate all the help he has given me over the last four years. I would also like to thank those professors who sat on my candidacy committee, Prof. Nadia Lapusta, Prof. Rob Phillips, and Prof. Oscar Bruno, and also those who will sit on my thesis defense committee, Prof. Nadia Lapusta, Prof. Shepherd, and Prof. Bhattacharya. Most of all, I would like to thank my advisor Prof. Ravichandran. He has given me the freedom to pursue all the topics that have interested me, and provided me with the resources to do so. He has also given me the opportunity to attend several conferences during my study. These experiences have allowed me to hone my scientific communications skills and to meet prominent scientists in my field. I am grateful for the time, advice, and support he has given me over the past four years.

My research has been funded by the Office of Naval Research (Dr. Y.D.S. Rajapakse, Program Manager). The financial support is gratefully appreciated. In addition, this year I have been the recipient of a PEO scholar's award, and I would like to thank Grace Verburg for sponsoring me for the award.

ABSTRACT

The mechanical characterization including evolution of damage and failure of foams and composites are becoming increasingly important, as they form the basic components of sandwich structures. Sandwich structures consist of two faceplates that surround a core material. In many modern applications, faceplates and cores are typically comprised of composite materials and polymeric foam, respectively. Knowledge of the failure behavior of these individual components is necessary for understanding the failure behavior and design of sandwich structures. A systematic investigation of the damage evolution and failure behavior of foams and composites was conducted using a variety of experimental techniques.

In-situ ultrasonic measurements were used to track the damage behavior in PVC polymeric foams with densities ranging from 130 to 250 kg/m³. The wave speeds were measured by two quartz piezoelectric shear transducers with a resonant frequency of 5 MHz in the transmission mode. A fixture was developed and constructed to protect the transducers during compression, while allowing them to take sound speed measurements of the sample along the axis of the load train. This fixture was placed in a servo-hydraulic MTS (Materials Testing System) machine, where the load-displacement response of the foam was recorded. A digital image correlation (DIC) method was used to capture the progression of failure under compression. Two dominant failure modes, elastic buckling and plastic collapse, were identified – and their onsets corresponded to the change in elastic wave speeds in the material, measured by the in-situ ultrasonic technique.

The transverse response of S-Glass/Epoxy unidirectional composites was investigated under varying degrees of confinement and strain rates. The experimental setup utilizes a fixture that allowed for independent measurement of the three principal stresses in a confined specimen. A servo-hydraulic materials testing system and a Kolsky (split Hopkinson) pressure bar generated strain rates between 10⁻³ to 10⁴ s⁻¹. Post-test scanning electron microscopy (SEM) observations suggest that under transverse loading at low-strain rates, confinement contributes to localized band formation. In addition, micrographs indicated that macroscopic transverse failure is dominated by shear stress, and occurs within these localized bands. These shear dominated failure bands were found inclined in a

direction approximately 35° to the direction of loading. Implications of this orientation deviation of failure bands from maximum shear trajectories at 45° are discussed in reference to the state of confinement.

TABLE OF CONTENTS

Acknowledgements	iv
Abstract	vi
Table of Contents.....	viii
List of Illustrations and/or Tables	x
Nomenclature.....	xvii
Chapter I: Introduction	1
1.1 Motivation	1
1.2 Review	3
1.2.1 Cellular Materials.....	3
1.2.2 Composite Materials	8
1.3 Approach and Objectives	15
Chapter II: In Situ Characterization of Damage in Polymeric Foams under Mechanical loading	18
2.1 Introduction.....	18
2.2 Materials	19
2.3 Ultrasonic Characterization Technique for in-situ measurement of wave speeds.....	23
2.4 Experimental Procedure	26
2.5 Simultaneous Measurement of Longitudinal and Shear Wave Speeds.....	28
2.6 Experimental Results and Discussion.....	40
2.7 Modeling for cell failure	49
2.8 Digital Image Correlation	58
2.8.1 Digital Image Correlation Algorithm	59
2.9 Digital Image Correlation Results	63
2.10 Summary.....	65
Chapter III: Characterization of Composite Materials	68
3.1 Introduction	68
3.2 Material.....	70
3.3 Failure Models	72
3.4 Low Strain Rate Experimental Set up	77
3.5 High Strain Rate Experimental Set up.....	77
3.6 Confinement	79
3.6.1 Low Strain Rate confinement method.....	79
3.6.1.1 Varying Confinement with polycarbonate Pads Inserts .	84
3.6.1.2 Measuring Confinement with Strain gages	86
3.6.1.3 Indentation	89
3.6.2 High Strain rate Confinement method.....	90
3.7 Experimental Results for Low Strain Rate Tests	93

3.8 Microstructural Characterization	106
3.9 High Strain Rate Results	116
3.10 Strain Rate Effect	121
3.11 Summary.....	122
Chapter VI: Conclusions	124
4.1 Summary	124
4.1.1 Foam	124
4.1.2 Composites	126
4.2 Recommendations for Future Work.....	127
Bibliography	131
Appendix A: Sandwich Structures	136
Appendix B: High strain rate setup	138

LIST OF ILLUSTRATIONS AND/OR TABLES

<i>Number</i>	<i>Page</i>
Table 2.1. Selected Physical and mechanical properties of DIAB PVC foam	20
Figure 2.1. SEM micrograph of H130 foam, where wall thickness is measured as ~11 μm	20
Figure 2.2. SEM micrograph of H160 foam, where wall thickness is measured as ~13 μm	21
Figure 2.3. SEM micrograph of H200 foam, where wall thickness is measured as ~30 μm	21
Figure 2.4. SEM micrograph of F250 foam, where wall thickness is measured as ~100 μm	22
Table 2.2. Dimensions of the cell diameter and wall thickness of the DIAB foam	22
Figure 2.5. Loading fixture and protective housing of ultrasonic transducers for in-situ measurements of wave speeds while subjecting the specimen to uniaxial compression.....	27
Figure 2.6. Input Signal from a shear transducer and output signals of the longitudinal and shear receiving transducers from experiments on aluminum are plotted as a function of time. The output from the receiving shear transducer shows an anomalous peak that corresponds to the arrival of the longitudinal wave.	29
Figure 2.7. Input Signal from a shear transducer and output signals of the longitudinal and shear receiving transducers from experiments on copper are plotted as a function of time. The output from the receiving shear transducer shows an anomalous peak that corresponds to the arrival of the longitudinal wave.	30
Figure 2.8. Input Signal from a shear transducer and output signals of the longitudinal and shear receiving transducers from experiments on steel are plotted as a function of time. The output from the	

receiving shear transducer shows an anomalous peak that corresponds to the arrival of the longitudinal wave.	31
Figure 2.9. x-t diagram of experimental setup indicating total travel time of longitudinal wave through the first spacer the specimen and the second spacer	32
Table 2.3. Measured wave speeds for selected engineering solids under no loading	35
Figure 2.10. Comparison between Ultrasonically-measured and mechanically measured Young's Moduli of Steel, Polycarbonate, Copper and Aluminum.....	36
Figure 2.11. Comparison between Ultrasonically-measured and mechanically measured Poisson's Ratio of Steel, Polycarbonate, Copper and Aluminum	46
Figure 2.12. (a)Displacement versus time graph for the aluminum compression experiment (b) Compliance corrected displacement versus time graph for the aluminum compression experiment	38
Figure 2.13. Young's Modulus, Shear Modulus and Poisson Ratio for Polycarbonate during Uniaxial Compression.....	40
Figure 2.14. Young's Modulus, Shear Modulus and Poisson Ratio for Aluminum during Uniaxial Compression.....	41
Figure 2.15. Young's Modulus, Shear Modulus and Poisson Ratio for Copper during Uniaxial Compression	42
Figure 2.16. Young's Modulus, Shear Modulus and Poisson Ratio for Steel during Uniaxial Compression	43
Figure 2.17. Plot of Ultrasonic Data for the low density foams 130 kg/m ³ density foam (a) Apparent Modulus (b) Apparent Poisson Ratio.....	46
Figure 2.18. Plot of Ultrasonic Data for the low density foams 160 kg/m ³ density foam (a) Apparent Modulus (b) Apparent Poisson Ratio.....	47
Figure 2.19. Plot of Ultrasonic Data for the low density foams 200 kg/m ³ density foam (a) Apparent Modulus (b) Apparent Poisson Ratio.....	48

Figure 2.20. Plot of Ultrasonic Data for the low density foams 250 kg/m ³ density foam (a) Apparent Modulus (b) Apparent Poisson Ratio	48
Figure 2.21. Ultrasonically-measured modulus at 0 strain and published values of modulus for various densities	49
Figure 2.22. Schematic of 2D Regular Hexagonal Cell	51
Figure 2.23. Illustration of the deformed regular hexagonal cell under (a) Plastic Collapse (b) Elastic Buckling	51
Figure 2.24. A plot of the Young's Modulus as a function of time is shown, with the drop in modulus due to drop in cell height at t_{crit} indicated.	54
Figure 2.25. A plot of the Young's Modulus as a function of time is shown, for the case of plastic cell collapse failure mode.	54
Figure 2.26. (a) A diagram of the 2D hexagonal cell indicating the 4 hinges A B C and D, and the rotation angle ϕ (b) A Free Body Diagram of a single side of the hexagon indicating the Work done, W , the moment at the hinge, M , the interior angle of the cell, θ , and the length of the cell wall, l	56
Figure 2.27. Experimental Set up for the Digital Image Correlation Technique	60
Figure 2.28. (a) Schematic of undeformed image area with undeformed subset indicated by shaded box (b) deformed image area with deformed subset indicated by cross hatch box	61
Figure 2.29. (a) Plot of peak location on x-y plane with displacement indicated by u and v (b) Plot of correlation function as a function of x position, showing the ideal d function peak in the case of little noise and the broader peak generated by correlation of noisy data	63
Figure 2.30. (a) Schematic of subset in image area with subset length and width indicated in pixels (b) pixel dimensions of image area given along with interval between image subsets (c) number of subsets in image plane along length and width indicated useable area of image indicated by smaller box.	64
Figure 2.31. Low Density Foam 130 kg/m ³ –Compression Results (a) before compression (b) after compression.....	66

Figure 2.32. High Density Foam 250 kg/m ³ –Compression Results (a) before compression (b) after compression.....	67
Figure 3.1. SEM Micrograph of virgin specimen of S2/8552 glass/epoxy composite.....	70
Figure 3.2. Schematic of specimen indicating length width and height.	70
Figure 3.3. Schematic of unidirectional composite specimen with its axes defined.	71
Figure 3.4. Positive and negative shear stress acting along principal material directions (adapted from Daniel,1994)	73
Figure 3.5. Tsai-Wu Failure Envelope for s2/8552 glass/epoxy composite.....	74
Figure 3.6. Schematic of the compression fixture used for quasi-static compression of confined and unconfined composite specimen.....	77
Figure 3.7. Schematic of Kolsky (Split Hopkinson) bar setup for high-strain-rate testing of materials	78
Figure 3.8. Schematic of the layered structure of the specimen and stress axis definition.	79
Figure 3.9. (a) Photograph of quasi-static confinement fixture (b) Schematic of the top view of the confinement fixture used for the quasi static test to introduce lateral confinement	80
Figure 3.10. Cross section of experimental setup, showing the transversely aligned fingers and the specimen	81
Figure 3.11. (a) Perspective view of testing assembly, (b) section view of the testing assembly, (c) magnified view of testing assembly.	82
Figure 3.12. Photograph of the confinement fixture (a) without maraging steel adapter, (b) Picture with maraging steel adapter.	83
Figure 3.13. Schematic of cross section of fixture showing finger, and polycarbonate pad and specimen	84
Figure 3.14. Typical result of nominal stress-strain data for transverse loading of S2/8552 glass/epoxy composite at a strain rate of .001/s	85

Figure 3.15. Cross Section of fixture showing finger, adapters, specimen and strain gauge location	86
Figure 3.16. Schematic of finger with applied loads and boundary conditions used in finite element simulation.	86
Figure 3.17. Location of monitoring sets in the finite element model	87
Figure 3.18. Contour plot of Mises stress in aluminum finger under simulated loading.....	87
Figure 3.19. Plot of nominal stress-strain curve at element #38 and element #3.	88
Figure 3.20. Indentation of inserts by the composite specimen	88
Figure 3.21. Effect of insert location on compressive strength.	88
Figure 3.22. Schematic of confinement fixture used in the dynamic test to introduce varying levels of confinement.	90
Figure 3.23. Photograph of the confinement fixture used in the dynamic test to introduce varying levels of confinement.....	90
Figure 3.24. Sample output from Dynamic tests, showing incident and transmitted pulse determined from the Hopkinson bar strain gages and longitudinal and transverse strain gage output on the confinement fixture.	91
Figure 3.25. Stress strain curve of uniaxial compression of S2/8552 glass/epoxy composite	92
Figure 3.26. Typical result of typical nominal stress strain data from a quasi-static test conducted at .001/s	93
Figure 3.27. Axial Stress-strain response of S2-glass/epoxy unidirectional fiber composite with aluminum finger in longitudinal direction and varying pad thickness in transverse direction	94
Figure 3.28. Axial Stress-strain response of S2-glass/epoxy unidirectional fiber composite with aluminum finger in transverse direction and varying pad thickness in longitudinal direction	95
Figure 3.29. Axial strength as a function of longitudinal strength for pad/finger tests	96

Figure 3.30. Axial Stress-strength of S2-glass/epoxy as a function of transverse strength for pad/finger tests	96
Figure 3.31. The transverse confining stress, σ_2 , as a function of the longitudinal confining stress, σ_1	97
Figure 3.32. A comparison of the Tsai-Wu, and Christensen Envelopes with experimental data gathered	98
Figure 3.33. Axial Stress Strain curves for aluminum finger in longitudinal fiber direction	99
Figure 3.34. Axial Stress Strain curves for Copper finger in longitudinal fiber direction	100
Figure 3.35. Axial Stress Strain curves for Steel finger in longitudinal fiber direction.....	100
Figure 3.36. Axial Strength as a function of longitudinal confining stress of composite material for various finger combinations.....	101
Figure 3.37. Axial Stress as a function of Transverse confining Stress of composite material for various finger combinations	102
Figure 3.38. Absolute value of transverse stress as a function of absolute value of longitudinal stress of composite material for various finger combinations	102
Figure 3.39. The stress strain curves for steel in the transverse direction with longitudinal confinement being varied by changing confining finger materials from aluminum, copper and steel and finally no confinement in the transverse direction	103
Figure 3.40. (a) Photograph of specimen with aluminum finger longitudinal confinement and aluminum finger transverse confinement. (b) Photograph of specimen with aluminum finger longitudinal confinement and copper finger transverse confinement.	104
Figure 3.41. Finite element model of deforming specimen with copper transverse finger confinement.	105
Figure 3.42. (a) Photograph of specimen with all around aluminum confinement (b) SEM micrograph of boxed area in (a) with angle of shear failure indicated	106

Figure 3.43. SEM micrograph of specimen confined by aluminum at varying magnifications (a) 232X, (b) 728X and (c) 5.88 KX	108
Figure 3.44. (a) Photograph of specimen for aluminum confinement test (b) SEM micrograph of boxed region in (a)	109
Figure 3.45. SEM micrographs of specimen in Fig. 3.49 at (a) 289X, (b)3200 X and (c) 14640X	111
Figure 3.46. (a) Photograph of composite specimen confined by steel (b) SEM Micrograph specimen at higher magnification.	112
Figure 3.47. SEM micrographs of specimen confined with steel fingers in both the longitudinal and transverse fiber direction: (a) 114X (b) 2970 X (c) 15690 X	114
Figure 3.48. Schematic of the finger used in the high strain rate test: (a) front view (b) side view. The side view also indicates the location of the strain gauge.	115
Figure 3.49. (a) Misses stress contour on side view of deformed finger section (b) plot of axial stress at element #37 and element #28. whose locations are marked in (a).....	116
Figure 3.50. Axial Stress as a function of longitudinal confining stress.....	117
Figure 3.51. Axial Stress as a function of transverse confining stress.....	118
Figure 3.52. Transverse confining stress as a function of longitudinal confining stress	118
Figure 3.53. Stress-strain response of S2-glass/epoxy unidirectional fiber composite for various confinements and strain rates.	119
Figure 3.54. The effect of confinement and strain rate on the maximum axial stress (transverse strength) of the composite	120

NOMENCLATURE

E Young's Modulus

E_{11} Young's modulus in fiber direction

ν : Poisson's Ratio

ρ : density

σ . Stress

ϵ . Strain

c_d . Longitudinal Wave Speed

c_s . Shear Wave Speed

t_d . Longitudinal Wave transit time

t_s . Shear Wave transit time

$t_{d_{total}}$. Longitudinal Wave transit time for wave to travel through 2 spacers and specimen

$t_{d_{spacer}}$. Longitudinal Wave transit time for wave to travel through spacers

$t_{d_{sample}}$. Longitudinal Wave transit time for wave to travel through specimen

$t_{s_{total}}$. Shear Wave transit time for wave to travel through 2 spacers and specimen

$t_{s_{spacer}}$. Shear Wave transit time for wave to travel through spacers

$t_{s_{sample}}$. Shear Wave transit time for wave to travel through specimen

H_{sample} Height of sample

h_0 undeformed sample height

n rotational stiffness of node where cell walls meet

$\dot{\epsilon}$ Strain rate

A Cross sectional area of sample

h_{cell} height of cell

m mass of sample

E_s Young's Modulus of cell wall

I moment of inertia of cell call

b depth of cell

T thickness of cell wall

M_p Moment at the hinge of two cell walls

P pressure force

ϕ Rotation angle

θ Internal cell wall angle

l length of cell wall

σ_{ys} yield stress

T_{crit} cell wall thickness below which elastic buckling occurs and above which plastic collapse occurs

C Correlation function

b_0 undeformed subset region

b_1 Deformed subset region

w length of subset side

d distance between points evaluated in image

T_{11} Tensile strength of composite in fiber direction

T_{22} Tensile strength of composite in matrix direction

C_{11} Compressive strength of composite in fiber direction

C_{22} Compressive strength of composite in matrix direction

L length of aluminum finger in biaxial tests

f_{12} biaxial tensile strength in composite

Chapter I: Introduction

1.1. Motivation

Cellular materials such as foams and fiber-reinforced composites were developed independently, and can be used independently in numerous applications. When combined, their unique characteristics result in an ideal combination for sandwich structures.

Sandwich structures pair a low density core material with a high strength composite. Two composite face plates sandwich a low density core, consisting usually of a cellular material such as foam or balsa wood, thus increasing the moment of inertia of the material system. This combination provides high bending stiffness while adding little additional weight to the system. Sandwich structures can also be tailored to specific applications by pairing different face plates and core materials. For example, choosing a specific core material can improve crash behavior and vibration damping characteristics or provide fire and noise insulation. The high stiffness to density ratio allows for significantly lighter structures without sacrificing their overall strength.

Fairbairn introduced the first sandwich structure in 1849 for bridge construction in London (Vinson). Nearly 100 years passed before the sandwich structure was used again – this time in a vastly different form, the fuselage of the Vultee BT-13 Valiant. The fuselage of the Valiant consisted of a fiberglass inner and outer tube, with balsa wood as the core. Balsa wood is just one example of a cellular material that can be used as the core of a sandwich structure.

Sandwich structures can easily be molded into complicated shapes due to their fabrication method. The face sheets, usually consisting of composite materials, are made by laying prefabricated flexible sheets called “laminates” onto a mold, layering them until the desired thickness is achieved. The laminate is then placed in a pressurized oven where the resin is cured, in a process also known as autoclaving. After the curing procedure, the mold is removed, leaving the rigid composite structure. Foams may also be molded into specific shapes by using a variety of machining methods.

An area of great potential interest for sandwich structures as structural materials is in marine structures. Ship size and speed have always been limited by the materials available to ship designers and builders. Lumber, the first ship construction material, though buoyant and plentiful, limited designs by its physical properties. The introduction of steel to the ship building industry produced larger vessels able to carry larger payloads with improved the defensive capabilities. Ship grade aluminum, the next material to revolutionize ship design, allowed for lighter ships while retaining the strength of heavy steel ships, making it ideal for high-speed boat design. Today, sandwich structures, a new class of materials, are on their way to becoming the next great leap in ship construction. The naval industry's interest in sandwich structures lies in the advantages they offer in critical applications where shock attenuation and impact damage protection are of concern. Because structures are exposed to numerous extreme conditions during their lifetimes, the materials used to construct them need to thoroughly evaluated. Sandwich structures consist of two different materials, composite and cellular, both of which are far less understood than the metals typically used in ship construction. These constituent materials must be individually studied under a wide range of conditions to gain understanding of their properties and thus facilitate their utilization in naval applications.

Due to the rapid advancement in computational power, computational solid mechanics can aid in the design of increasingly complex structures. Abaqus, Ansys, Nastran, Marc and COMSOL Multiphysics are a prominent few of the many programs currently used to test and validate engineering designs. These computer programs require models that accurately predict the response of materials under various loading conditions. Experimental results and the fundamentals of solid mechanics aid in the development of such models. As experimental results emerge, models can be modified to more accurately portray the damage mechanisms involved in a certain set of loading conditions. A variety of experimental techniques is necessary for exploring all aspects of a material's failure behavior. The following section 1.2 will illustrate the need for models consistent with the behavior exhibited by both foams and composites for the effective utilization of sandwich structures.

1.2. Review

1.2.1 Cellular materials

Cellular materials have long been a human necessity. Wood, a naturally occurring cellular material, has been used to construct shelter, boats and tools. The word *material* itself is derived from the Latin *materies*, meaning tree trunk (Gibson and Asbhey). In 1660, Robert Hooke became the first to inspect a cellular material under a microscope, namely, cork. In *Micrographia*, Hooke identifies the basic unit of biological structures, which he names cells, after the Latin *cellula*, meaning small room. Until 1909, only naturally occurring cellular materials such as wood, coral and sponge, were utilized by man,

In 1909, Leo Baekeland discovered and patented a process to make phenol-formaldehyde resin. His invention heralded the commencement of the plastics industry (Skochdople). In the next decade, sponge rubber became the first commercially available synthetic cellular material. During WWII, German scientists developed the first polyvinyl chloride (PVC) foam. PVC foams, waterproof and nonperishable – unlike wood – made them ideal for marine applications. At the end of the war, German patents for the PVC foam were brought back to the United States, where the technology to produce and manufacture these materials developed further. (Plastics Engineering Handbook, 1976). By the early 1950s, synthetic cellular materials became a mainstream, commercially viable material used in four general areas: thermal insulation, packaging, load bearing, and buoyancy.

Throughout the 1950s and 1960s, the foaming processes and manufacturing mechanisms of plastic foams were developed. The Plastics Engineering Handbook (1976) provides an overview of the foaming methods and extrusion processes developed from the 1940s to 1976. Early work on the characterization of cellular materials was conducted by Gent and Thomas (1963), Shaw and Sata (1966), and Patel and Finnie (1970).

Gent and Thomas (1963) attempted to model the foam as a 3D network of strings attached at their end points to form a cubic lattice. They then related the length of the cell wall to the thickness of the string and the modulus of the plastic from which the foam was made. No attempt was made to incorporate the effects of non-homogeneity of real foam in

their model. However, their tensile and compressive tests yielded results that correlate reasonably with predicted theoretical values, and this model is still used to predict the strength of foam materials.

Shaw and Sata (1966), concerned with how deformation occurs in foam, observed that deformation concentrates at a row of cells and then propagates through the material, much like the Luders bands seen in steels. This behavior was related to the tearing of the cell wall under deformation. They also turned to a 2D hexagonal cell representation of the random 3D network of cells in foam to derive yield criterion for foamed polystyrene.

Patel and Finnie (1970) investigated the creation of quantitative relations between the properties of foam and the properties of the plastic from which the foam was made. They found that cell size and density affected the strength of the foam. These relationships were derived by modeling the foam unit cell as a two dimensional hexagonal shape. This became a common approach, as modeling a complex three dimensional structure such as foam is quite difficult.

In 1980, Suh and Skochdopole authored one of the first reviews of the literature on the mechanics of cellular materials. From 1981 to 1988, an immense number of publications by L. J. Gibson arose, on the characterization of two dimensional cellular materials (1982) and also on three dimensional cellular materials (1982).

Gibson and Ashby's *Cellular Materials* was published in 1988. It provided a comprehensive look at the work on cellular materials and attempted to "unify the ideas about cellular solids" (Gibson, 1988). Gibson and Ashby propose three criteria to fully characterize foam: open or closed cell structure, relative density, and the ratio of anisotropy of the material (Gibson, 1988). "Open" celled foam can be thought of as a matrix of window frames with the window pane removed, while closed cell foams would appear to have window panes intact. This distinction also accentuates the fact that the closed cell foams have a pressurized gas within each cell, the importance of which lies in the linear elastic response of these materials. Fluid can flow through open cell foams; they do not trap air inside them. The relative density of the material is the ratio of the foam density to the density of the cell wall, i.e. the density of the constituent material. For example, the cell wall density of PVC foam is the density of solid PVC. In most cases of polygonal cells,

cell wall length and thickness can be related to the relative density of the foam. Most cellular materials tend to be anisotropic. Wood has elongated cells in the longitudinal direction of the tree trunk, and foamed cells are slightly elongated in the rise direction of the foaming. Much like bread, foams are formed in molds, and when subjected to chemical foaming agents, grow upward to fill the mold, creating elongated cells in the direction of the rise. In *Cellular Solids*, Gibson and Ashby choose to ignore this effect when evaluating cells; however, they do provide an Appendix explaining how this property can be incorporated in the evaluation of cellular materials.

After the criteria for foam characterization were established, the mechanical behavior of foams was presented in *Cellular Solids*. At low stress and strain levels, foams behave as linearly elastic materials and can be treated as such. Only when a load is increased beyond the “yield” stress of the material does foam behavior differ from typical linear elastic materials.

When considering the behavior of cellular materials beyond the linear elastic regime, the foam’s microstructure must be considered. A homogeneous material under uniform stress typically deforms uniformly (Weaire and Fortes). A cellular material, however, may not behave in this manner. The trouble with characterizing cellular materials – particularly foams, is that they are amorphous and have a complicated cell structure. In order to understand the behavior of cellular materials under stress, Gibson (1982) first considers the simplest cellular foam to analyze: a 2D hexagonal array of cells. These ideas are then extended to regular polygonal shapes in 3D, also an idealization of the true nature of foams.

The deformation behavior of 2D structures has been experimentally investigated in a number of papers on a number of topics, including the compression of a chain of rings (Reid 1983, Wang 1987 and Reddy 1991), compression of a stack of metal pipes (Reid and Reddy 1978, Reid 1983, Shim and Strong 1986 1987), the compression of a stack of drinking straws (Poirier 1992), and the 2D deformation behavior of regular honeycomb structure (Gibson and Ashby 1981). These studies all demonstrate that deformation concentrates in a weak or over-stressed region of the structure, and then propagates throughout the material. Compression experiments carried out on common cellular

materials (Shim 1992, Vaz and Fortes 1993) showed the same result, localization and propagation of a deformation band.

Meanwhile, tests were still being conducted on the deformation behavior of cellular materials using conventional methods. Maiti *et al.* (1984) published a study of elastic, plastic and brittle foams, and developed a mechanism mode map. This map was designed to help select the optimal foam for a specific load-bearing or energy-absorbing application.

Triantafillou *et al.* conducted an experimental investigation in the behavior of foams under multi-axial loading (1989). Their aim was to develop a failure surface for two open cell and two closed cell polyurethane foams. A complex failure envelope was proposed and experiments were conducted to characterize foams under multi-axial loading. Their study showed that the failure envelopes proposed agreed well with the gathered experimental data. The work of Triantafillou *et al.* highlighted the complex nature of foam failure behavior and the inadequacy of the maximum principle stress criterion used for failure characterization up to that point.

A Marine Composites Symposium was held in 1993 to discuss the research on and development of sandwich structures. Chevalier presented creep and fatigue properties of balsa wood and PVC foam, and showed that balsa wood has 2 to 9 times longer fatigue life than PVC core materials. Schmidt, however, asserted that polyetherimide foams had superior strength, stiffness and moisture resistant properties.

In 1994, Papka and Kyriakides revisited Gibson and Ashby's work on the collapse of a 2D honeycomb structure. This study focused much more on the material response after the initial yield point in the compressive stress strain curve. They found that deformation tended to localize in one row of the cells that collapse. Once the top and bottom face of the cell wall were in contact, the deformation in that row was arrested and deformation spread to other rows in the material. These results compared well with computer simulations of the collapse of these materials. Once all cells had collapsed, a sharp rise in the stress strain response of the material was observed, known as densification.

Weaire and Fortes published an attempt at a numerical simulation of the collapse of cellular materials in 1995. Their study concentrates not only on the behavior of solid foam,

but also on liquid foam, and addresses the fact that 2D phenomenological models are inadequate for comprehensive modeling of the disorder in cellular materials. Zhang *et al.* (1997) examined the strain rate dependence and temperature effects on the polymeric foams subjected to high rate impact loading. Models were developed, presented, and implemented in a finite element program. The models showed that polymeric foams were extremely strain-rate and temperature-dependent and it found that while foam may behave in a ductile manner under compression, it may fail as a brittle material in tension or shear. In 1998, Bastawros applied digital image correlation (DIC) to analyze the deformation mechanism in closed cell aluminum alloy foams. He also identified the three stages of deformation similar to the observations by Papka (1994) for honeycomb structures. Andrew *et al.* (1999) worked on relating the creep behavior of 2D honeycombs and foam structures to their cell wall properties and relative density.

A significant portion of the research on the use of ultrasonic techniques to characterize foams focuses on the molten polymer foam extrusion process. The manufacture of polymeric foams is critical for the resultant strength of the polymer. As it is costly to test each batch of material produced, PVC foam manufacturers desire a real time evaluation of the foam while still in its molten state to create a better, more uniform product, with less material waste and time spent mechanically testing the finished foam. In 1984, Erwin and Dohner used focused ultrasound measurements to determine the dispersion of an additive in a polymer melt. Kryukov et al (1997) used a rolling ultrasonic setup to detect voids in rigid polyurethane foams. This device was primarily used for quality control and did not attempt to relate ultrasonic wave propagation speeds to material properties. Sahnoune (1997) described an ultrasonic technique for monitoring the properties of foaming in polymers. This study showed that easily implemented ultrasonic measurements could be used to test bubble formation, phase transformation, and the dynamics of phase separation. These measurements could all be implemented during the manufacturing process and used as quality control. Freemantle et al (1997) developed an ultrasonic measurement technique able to monitor the modulus of an adhesive during curing. This method utilized both the longitudinal and shear wave speeds for characterization of the adhesive and was calibrated on aluminum and copper samples. An

ultrasonic pulse applied at an angle to the specimen to be measured excited the shear wave. Sahnoune (1998) used ultrasonic characterization to obtain the rheology parameters of polymer foams. Piche (1999) expanded on this work by developing an on-line process monitoring the rheology of the foam using an ultrasonic technique. Abu-Zahra *et al.* (2002) further expanded this idea to include the on-line monitoring of PVC foam density using ultrasound waves and artificial neural networks. Rizzo *et al* (2005) used ultrasonic characterization to evaluate the elastic constants of the material. They developed a model to predict the wave speed in the material; however, the experimental results showed that the model underestimated the wave speed in the material. Their paper concludes that more accurate and robust models are needed to address the complex behavior of ultrasonic wave propagation in cellular materials.

Digital Image Correlation has been used by Wang and Cuitino to obtain full field measurements on open cell polymeric foams. The results of their work support the hypothesis that the deformation of open cell polymeric foams is a phase transition phenomena. Gioia *et al* also used digital image correlation to explore the compression of open-cell solid foams. They found that the deformation in uniaxial stretches foams exhibited a phase transformation behavior as well. They created a numerical model of stratified mixture of phases within the cell which propagated. This model compared well with the digital image correlation test results. Numerical work by Overaker *et al* found that the optimal strut angle for regular hexagonal foams bonded to two plates was 100° . The effect of cell strut angle on the relative density makes the angle significant. They concluded that foams with negative Poisson's ratio could simply be rotated to exhibit a positive Poisson ratio effect. Therefore the angle at which the load is applied to the foam will dramatically effect is structural properties. Additional work can and must be done to understand the complicated phenomena in characterizing cellular materials.

1.2.2 Composite materials

The most rudimentary description of a structural composite material is simply a combination of a strong “reinforcement” material and a weaker, more flexible “matrix”

material. Humans have used this concept for millennia to construct bricks, combining the stiffer straw “reinforcement” material with the weaker mud or “matrix” material, to create a material system both stiff and flexible. The mortar used to build the Roman Coliseum, for example, was reinforced with horse hair fibers. From the twentieth century onward, iron rods were used to reinforce concrete in the construction of buildings and bridges (Daniel, 1994).

The development of modern composites can be traced to the invention of fiberglass and plastics. As mentioned above, the plastics industry emerged in 1909 with Baekeland’s discovery of a method for making phenol-formaldehyde resin. In 1938, Russell Games Slayter of Owens-Corning invented fiberglass, for the purpose of insulation. The first modern composite material was created when the stiff fiberglass fibers were added to polyester plastics for reinforcement. The first use of fiberglass/epoxy composite was in the nose radar domes of WWII aircraft, to replace the heavier, less electromagnetically transparent plywood and canvas-urea domes (Vinson, 1975). The material later found use in naval applications, when in 1942, the first boat made from fiber glass was introduced (Daniel, 1994). The first laminates, pre-impregnated polyester resin with fiberglass fibers, were also introduced that year. The laminate contained a series of long, parallel fibers within a sheet of epoxy. The laminate sheet, though strong along the fiber axis, was weak along the transverse axis. Manufacturers overcame this deficiency, however, by easily aligning the sheets’ fiber axis with the structure’s load-bearing axis. Previously, composite materials contained short segments of randomly aligned fibers. Though this configuration was homogeneous, it lacked the strength of composites, whose fibers aligned in a single direction. By 1946, the United States government had patented the first filament winding process, which took pre-impregnated tape and wound it around a mandrel surface in a precise geometric pattern. Layering fibers in specified directions made tailoring a structure for a specific application possible. This process was particularly useful in the construction of missile casings. With the development of new plastics and improved fiber fabrication processes in the early 1950’s, composites found use in a diverse group of industries. In 1956, fiberglass/epoxy laminates were used for manufacturing printed circuit boards. Chevrolet and Boeing utilized reinforced plastics in designing the Corvette and the 727.

Composite materials were also employed to produce fishing rods, bathtubs and helicopter fuselages (Vinson, 1975). In the early 1960's, boron and high strength carbon fibers were introduced for composite use, and the fuselage section of the F-111 was constructed from boron/epoxy composites (1967).

Experimental investigation into the mechanical behavior of composite materials began in the mid 1960's. Reviews of this early work can be found in Lenoë (1970), Prosen (1969), Bert (1975), Chiao (1976) and Agarwal (1980). The ability to predict failure from a specified state of stress became important for the growing number of industries using these new materials in structural applications. In 1965, Stephen Tsai of the Air Force materials laboratory presented the first failure criterion for composite materials, as simply the yield criterion of an orthotropic, ideally plastic material, given by Hill (1948). While this model only required easily obtained measurements for the coefficients, it was based on the assumption that isotropic stress had no effect on failure. Later, in 1967, Hoffman (1967) added linear stress terms to the Tsai model to account for the unequal failure stress in tension and compression. Tsai and Professor Wu of Washington University endeavored to examine the emerging strength criteria for composite materials, and proposed their own general unified theory on the subject in 1970 (Tsai *et al.* 1970). Their aim was not to identify the mechanisms of FRC (Fiber Reinforced Composites) failure, but simply to create a useful tool for composite material characterization. Construction of a composite's failure envelope requires the strength parameters in both unidirectional and multi-axial stress states. The paper encouraged experimental investigation of the combined stress state, which at the time of the publication was scarce. Pipes and Byron (1973) attempted to investigate the combined stress state by conducting off-axis strength tests on boron/epoxy composites. While their results agreed with the Tsai-Wu model predictions, Pipes and Byron reported difficulty in obtaining multi-axial stress states in compression, and recorded widely varying results in tension. They stressed the need for more investigation into the strength of composites under multi-axial loading (Jones, 1975).

The disadvantage of the Tsai-Wu model is its dependence of a single coefficient on the multi-axial strength of the material. Experiments to determine this coefficient were costly, and results from these tests varied widely for multi-axial compression and tension.

Therefore, Hashin (1973) presented a fatigue failure criterion for composites in plane stress, which had a smooth, piecewise form, and each smooth branch represented distinct failure modes: fiber dominated tensile and compressive modes, and matrix dominated tensile and compressive modes. The fully realized version of this failure criterion was published by Hashin in 1980. This model relied only upon unidirectional tensile and compressive failure data of composites, along with axial and transverse shear failure data, all of which could easily be obtained experimentally.

Important to note is that Narayanaswami (1977) performed a numerical study on the significance of the multi-axial strength coefficient in the Tsai-Wu model, and found that the error due to simply neglecting it would be no greater than 10%. The paper offered no physical argument as to why the term could be ignored. However, Narayanaswami's finding may explain why the Tsai-Wu model is the most widely used to predict failure in composite materials, in that if multi-axial strength is ignored, the Tsai-Wu model requires fewer parameters than the Hashin model.

While resin and fiber technology advanced throughout the 1970's and 1980's, the manufacturing process used to construct composite structures remained relatively static. These processes typically involved time-consuming lay-up of pre-impregnated epoxy tapes and a lengthy autoclave procedure. As a result, construction of composite materials was 5 to 10 times more expensive than their metal counterparts, although composite materials provided significant weight savings to a structure. The Resin Transfer Molding (RTM) process developed in the 1980s eased the automation and reduced the cost of the manufacturing process, thus greatly increasing the number of sizes and shapes composite structures could attain (Rackers, 1998). Unlike the standard autoclaving process of layering epoxy tapes pre-impregnated with fibers, to create an object, RTM separately constructs a fiber form, into which it then injects a resin. This new manufacturing method piqued naval interest in creating thick composite materials for use in sandwich structures.

By the early 1980's, experimental investigation of composites ranged from simple uniaxial tensile compressive and shear tests to speckle interferometric techniques, moiré methods, thermal cycling, and moisture control test methods (Whitney 1982). The area of failure characterization of composites focused on laminates, a system of several layered

lamina. The method of layering composite laminates in multiple directions was developed to create a composite strong along multiple axes, unlike a unidirectional composite with fibers along only one axis and strong only in one direction. Laws *et al.* (1988) studied progressive transverse cracking in composite laminates. Lim published a study of the prediction on transverse cracking and stiffness reduction in cross-ply laminated composites in 1989. Tsai built upon Laws' *et al.* and Lim's findings, with an investigation into the progressive matrix cracking of cross-ply composites under biaxial loading (1990). Daniel (1991) studied the cracking in composite laminates under biaxial loading and later experimentally investigated the behavior of cracked cross-ply laminates under shear loading (1992). As a response to the interest in the post failure behavior of composites, Walter (1995) investigated the post-failure behavior of silicon carbide fiber/ceramic matrix composites. The study used a combination of ultrasonic, acoustic emissions, as well as stress-strain data to determine the "zones of deformation," which identify the onset of different failure mechanisms of the material.

Christensen (1997) revisited stress-based yield/failure criteria for fiber composites and proposed a new model that follows the piecewise smooth decomposition of the Hashin criterion, but combines the fiber-dominated tensile and compressive modes into a single fiber-dominated mode. The matrix-dominated tensile and compressive modes are similarly combined. Christensen uses strength parameters generated by Parry and Wronski (1982) and compares the failure prediction to data gathered from Parry and Wronski (1985). His model is consistent with the experimental data, but most significantly it predicts the effect of pressure upon the yield of the tensile and compressive stress in the fiber direction.

As the size of composite structures increased, so did the relevance of specimen size. Winsom *et al.* (1999), in studying the failure strength of carbon and glass epoxy materials, found that there is a size effect. These size effects must be taken into account when using smaller size coupons for the characterization of larger structures. The study concluded that the strength of the composite is inversely proportional to species volume. The data gathered in the test conformed to the Weibull strength theory and suggested that strength is controlled by defects, especially voids and machining damage. The paper indicated that

great care must be taken to ensure the manufacturing process minimizes the level of voidage in composite materials.

Oguni and Ravichandran (1999) presented a study of the micromechanical failure of unidirectional composites and a model to predict their behavior. Oguni's model was compared with the Tsai-Wu failure envelope; the former estimated a much lower compressive failure load and a much greater transverse fiber failure mode than the latter. Several conclusions about fracture in composites were made as a result of this analysis; most importantly, that failure is governed by the dominant crack in a given loading condition. In 2002, Oguni and Ravichandran presented an energy-based model for predicting the compressive strength of unidirectional fiber-reinforced composites that fail by longitudinal (axial) splitting. Their proposed model lead to three conclusions; first, composites with larger fracture energy and small fiber diameters result in higher strength, second, the degree of anisotropy plays a significant role in influencing the compressive strength of a material, and finally, the effect of confining pressure on compressive strength is relatively weak. The paper successfully tied the compressive strength of the composite to its material properties including surface energy, fiber volume fraction, fiber diameter and lateral confining pressure.

Following Tsai and Wu's 1970 call for further experimentation on the failure behavior of composites under a combined stress state, several articles were published on both the response of composite materials under biaxial stress and 3D stress states. Work on the failure behavior of composites under biaxial stress states had been investigated by Soden (1998), and early work on applying a 3D stress state to a composite material involved a combination of hydrostatic stress and simple unidirectional stress. These experimental investigations revealed the strong effect of hydrostatic pressure on the strength properties and failure modes of the material. However, these experimental investigations did not offer information on the behavior of composites under a 3D stress state. Zinoviev (2001) attempted to address this issue and understand the behavior of high strength unidirectional composites under tension with superimposed hydrostatic pressure. He published a set of comparative experimental investigations of carbon, glass, and organic fibers in an epoxy matrix. The studies found that while the longitudinal modulus of the

composite was unaffected by the hydrostatic pressure, the longitudinal failure strength of the composite had a non-monotonic dependence on it., The study also determined that there was a tendency for failure zones to localize with increasing hydrostatic pressure.

Recently, O'Brian published several papers on the experimental investigation and numerical simulation of S2-8552 glass/epoxy composite, which focuses on the transverse strength of the unidirectional variety of S2-glass/epoxy composite materials. The 2001 study reported the influence of specimen preparation and specimen size on composite transverse tensile strength and found that polishing had a detrimental effect on the strength of composite material. The study also determined that the Weibull scaling law over predicts changes in the transverse tension strength of three point-bend tests and underpredicts transverse tension strength in four-point bend tests, thus leading to the conclusion that the Weibull Scaling Law does not adequately predict the transverse tension strength of composite materials. O'Brian's next publication discussed the numerical optimization of specimen size to generate a fully-constrained plane strain state in a composite sample during 3-point and 4-point bending tests. They found that a longer span between base nodes produced a uniform plane strain state in 3-point bending tests, and a longer span between inner and outer nodes produced a uniform plane strain state for 4-point bending tests (2001). These results were used to make specimens for O'Brian's later experiments to determine the transverse tension fatigue life characterization of S2/8552 glass epoxy composite and Im7/8552 composite samples (2001). Among the papers's major findings, was that the transverse tensile strength of S2/8552 glass epoxy could be predicted using the Weibull scaling law. This finding is significant for the characterization of failure of composite materials, since transverse tensile strength is one of the parameters needed to construct the Tsai-Wu failure envelope.

Basu also used computational modeling to simulate the damage behavior of composite materials. His model was based on the extended Schapery theory, based on a thermodynamically consistent internal state variable formulation. The model allows for the analysis of compressively loaded composite structures in the presence of locally unstable material response, such as kinking. The model also demonstrated the little dependence it had on the mesh size, beyond the characteristic element size.

The transverse failure of thick S2-glass/epoxy fiber-reinforced composites was addressed in an experimental investigation by Vural *et al* (2003). The study conducted quasi-static and dynamic tests on thick composite materials under multi-axial confinement to investigate their failure behavior. Multi-axial confinement was provided by a metal cylindrical sleeve affixed around a unidirectional test specimen. While the tests were not able to measure the principle stresses on the material independently, a qualitative failure behavior for these materials was presented. The results suggested that an increase in the confinement of the material greatly increased the maximum attainable failure stress and the strain. Additionally, scanning electron microscopy of the recovered specimens revealed localized shear failure. A Mohr-Coulomb failure criterion was suggested to represent the observed transverse failure. Vural *et al.* (2005) presented work on the dynamic compressive failure of unidirectional fiber-reinforced composites under confinement. The results of these tests were again qualitative because the principle stresses could not be measured independently. However, the results of the tests indicated that as confinement increased, maximum attainable failure stress, as well as failure strain, increased.

In an interesting approach to unifying the failure behavior theory of composite materials, Yerramalli and Waas (2004) attempted to summarize the results of previous studies on glass and carbon fiber/epoxy composites. They compiled the various failure mechanisms proposed with their dependences on different material properties, and presented a non-dimensional number to classify composite compressive failure. This parameter was used to make predictions of failure, which were compared with experimental data and found to coincide. They concluded that this parameter could be used to predict compressive failure in composites.

The strain rate effect on in-plane shear strength of S2 glass/epoxy composites was presented by Tsai *et al.* in 2005. This paper presented experimental results that indicated that shear failure strength increases with increasing strain rate; however, the failure strain of the material decreases with increasing strain rate. Inspection of the recovered specimens revealed that specimens with an off-axis orientation of less than 10° showed fiber micro-buckling failure behavior, orientations between 15° and 45° showed in-plane shearing, and orientations greater than 45° displayed out-of-plane shear failure behavior. The analysis

concluded that the presence of transverse normal stresses had little effect on the shear strength of the material. Schultheisz and Waas present a broad review of the compressive failure of composites in their two part review published in 1996. These reviews not only discussed the issues related to compression testing of composites and their failure models as well as the experimental studies conducted to understand the micromechanics influences on the compressive strength of the material.

In the republication of *Mechanics of Composite Materials*, Christensen expresses his frustration over the lack of even an approach toward consensus of failure characterization, since the early failure criteria were made in the early 1970s (2005). It is in this framework that the present study discusses the results of an experimental investigation that seeks further information into to basic inquiries, such as the transverse response of unidirectional composites under varying degrees of confinement and strain rates.

1.3. Approach and Objectives

The characterization of sandwich structures requires knowledge of the failure behavior of their constituents. Therefore, a two-pronged investigation was launched into the failure behavior of both polymeric foams and composite materials. The major objective of the present study is to characterize and develop a fundamental scientific understanding of the mechanical response and deformation behavior of cellular core materials such as polymeric foam, and fiber-reinforced composites such as S2-glass/epoxy, under transient dynamic loads and to develop reliable constitutive models over a wide range of strain rates and multi-axial loading conditions of relevance to structural applications.

Chapter 2 presents the investigation of polymeric foams, specifically; closed cell PVC foam manufactured by DIAB, with densities ranging from 130 to 250 kg/m³. This foam was chosen because of its wide use in sandwich structures. The study of these materials involved *in-situ* ultrasonic measurement to track damage during deformation. The results indicated a separate failure mode for the lower density and higher density foams. Models of single cell failure behavior were used to predict macroscopic failure behavior. A

digital image correlation method was coupled with ultrasonic measurements to visualize the macroscopic failure behavior of the foam. The outcomes of these experiments agreed with the predictions made by the unit cell models for failure. The cell wall thickness was found to be the relevant parameter in the prediction of failure behavior of foams made from the same constituent material, but with varying densities,

Chapter 3 centers on the examination of a unidirectional fiber-reinforced composite material. The material chosen for investigation was a unidirectional S2/8552 glass/epoxy composite. The approach adopted for this study was (i) to utilize instrumented multiaxial quasi-static and dynamic experimental methods for the measurement of mechanical response and (ii) to conduct post-mortem scanning electron microscopy (SEM) on recovered specimens for a comprehensive understanding of the mechanics of deformation and failure modes at the microstructural level. The results indicate that the mechanical response and the strength of composite are a function of the transverse confining pressure and mainly governed by the properties of matrix material. Post-test scanning electron microscopy (SEM) observations suggested that under transverse loading, confinement contributes to the homogenization of shear failure at low-strain rates but does not have a significant effect at high strain rates. It was also observed that macroscopic transverse failure is dominated by shear stresses and occurs within localized bands through multiple fiber-matrix interface failures at the microscale. These shear-dominated failure bands are found to be inclined in a direction approximately 35 degrees to the direction of loading. Implications of this deviation in the orientation of failure bands from maximum shear trajectories at 45 degrees are discussed with reference to confinement stresses and strain rate. The final chapter summarizes the findings of this study and highlights the several issues that require further investigation.

Chapter II: In-situ Characterization of Damage in Polymeric Foams under Mechanical Loading

2.1 Introduction

While cellular materials have been one of the oldest materials used by man, mainly in the form of wood, studies concerning characterization of their failure behavior have been limited. The fundamental understanding and modeling of cellular materials is necessary not only on their elastic state, but also their damage behavior. In the present work, *in-situ* experimental techniques were developed to explore the damage behavior of polymeric foams while subjected to mechanical loading. All experiments were conducted on PVC foams manufactured by the DIAB Corporation. These materials are closed cell foams, and samples of four densities from the H grade donated by DIAB were used in this study. The foams were all tested in uniaxial compression at “low” ($\sim 10^{-3} \text{ s}^{-1}$) strain rates, using a Materials Testing System (MTS). Failure modes of these materials were inferred based on the measurements and observations obtained using a wide array of investigative tools, including *in-situ* ultrasonics and digital image correlation.

There are numerous studies on the failure behavior of cellular materials, as presented in Chapter 1. The research on the accumulation of damage and the failure behavior of cellular materials relies on mechanical testing and post mortem evaluation of the exterior surfaces of cellular specimens. Typically, ultrasonic characterization has been used as a window into the internal behavior of optically opaque materials. However, it is difficult to apply this method to cellular materials, because the ultrasonic signal loses energy as it propagates through a material due to spreading, scattering and absorption (Abu-Zahra 2002). Despite these difficulties, Ashman (1987) has successfully measured the mechanical properties of cancellous bone (a cellular material). Although there has been work by Abu-Zahra (2002) on the measurement and use of the longitudinal wave speed in molten PVC foam, for determining the density of the material, there has not been an

attempt to measure the mechanical properties of PVC foam using the ultrasonic measurements.

This chapter is organized as follows; first, the material used in the investigation is described, followed by an introduction to the ultrasonic method developed for the *in-situ* investigation of foams. This section details the newly developed ultrasonic characterization of materials, the design of the fixture and the validation of the experimental technique. The results of the experiments performed on the foam samples using the ultrasonic technique are then presented along with the proposed failure mechanisms responsible for the macroscopic observations. An optical technique developed for tracking the cell collapse in foams is then presented along with the digital image correlation technique used to analyze the images. The results of these tests are then discussed in relation to the results found earlier using the ultrasonic technique. The chapter concludes with a brief summary of the present work.

2.2 Materials

The H-grade PVC foams studied here were manufactured by the DIAB Corporation (DeSoto, TX), and are commonly used in sandwich structure applications such as the ones described in Chapter 1. The foam samples were all semi-rigid foams with a closed cell structure. PVC has a density of 1.5 g/cm^3 , a Young's Modulus of 2.4 GPa, and yield strength of 40 MPa. The foam has many desirable characteristics for its use in marine sandwich structure applications, including its closed cell nature and hence its imperviousness to water. The DIAB Corporation provided 4 sheets of material, H130, H160, H200 and H250 for the study. The number designation following the H represents the density of the material; for example, H130 has a density of 130 kg/m^3 . The samples received were 1-foot-square pieces that were of 0.4 inches in thickness. Cubical samples were cut from the foam by a band saw and then polished with 400 grit sand paper. The prepared samples were 0.95 cm cubes with highly planar surfaces on the sides of cube.

Table 1 lists the data for selected physical and mechanical properties found on the DIAB website.

Table 2.1. Selected physical and mechanical properties of DIAB PVC foams

Grade	H130	H160	H200	H250
Density kg/m ³	130	160	200	250
Compressive Strength (MPa)	2.5	3.4	4.4	5.8
Compressive Modulus (MPa)	175	230	310	400
Poisson Ratio	0.32	0.32	0.32	0.32

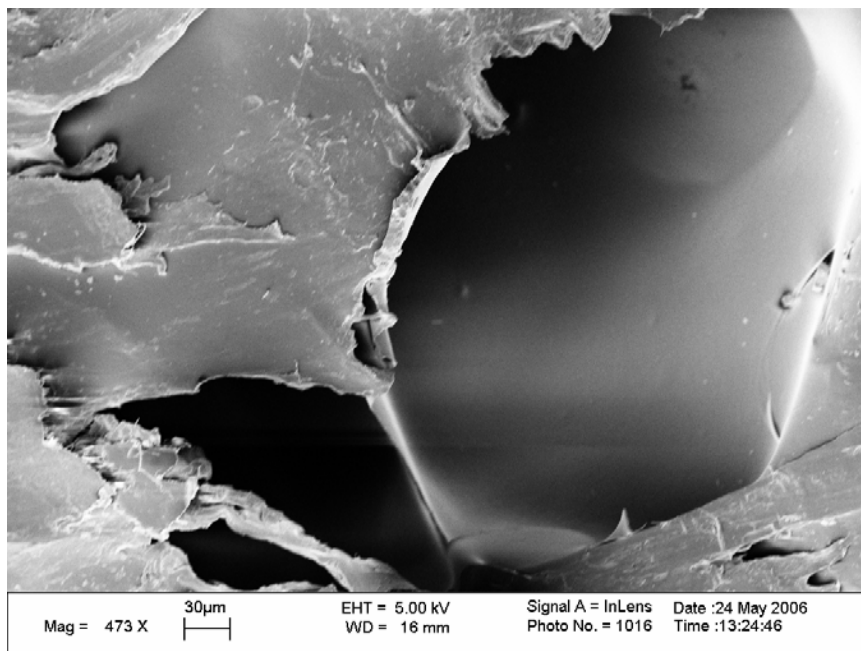


Figure 2.1 SEM micrograph of H130 foam, where cell wall thickness is measured as $\sim 11\mu\text{m}$

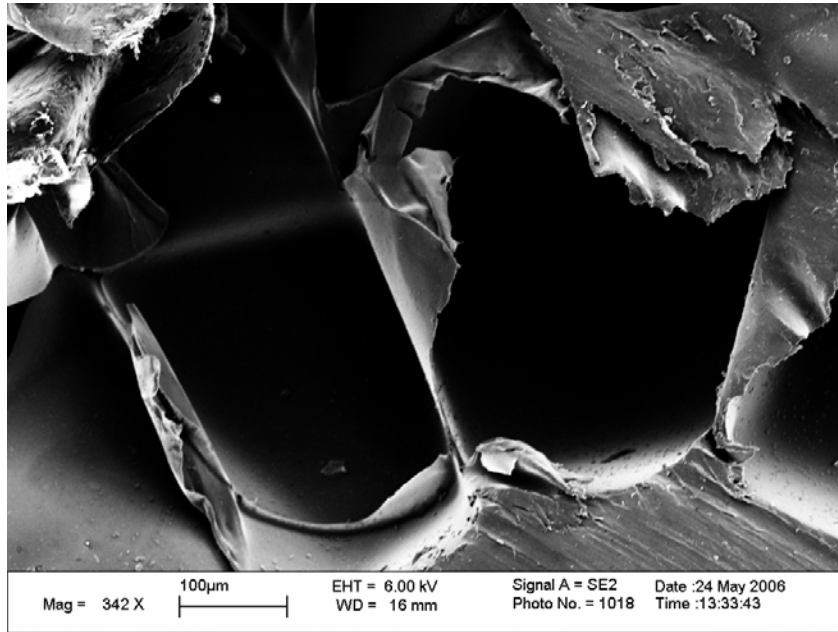


Figure 2.2. SEM micrograph of H160 foam, where cell wall thickness is measured as $\sim 13\mu\text{m}$

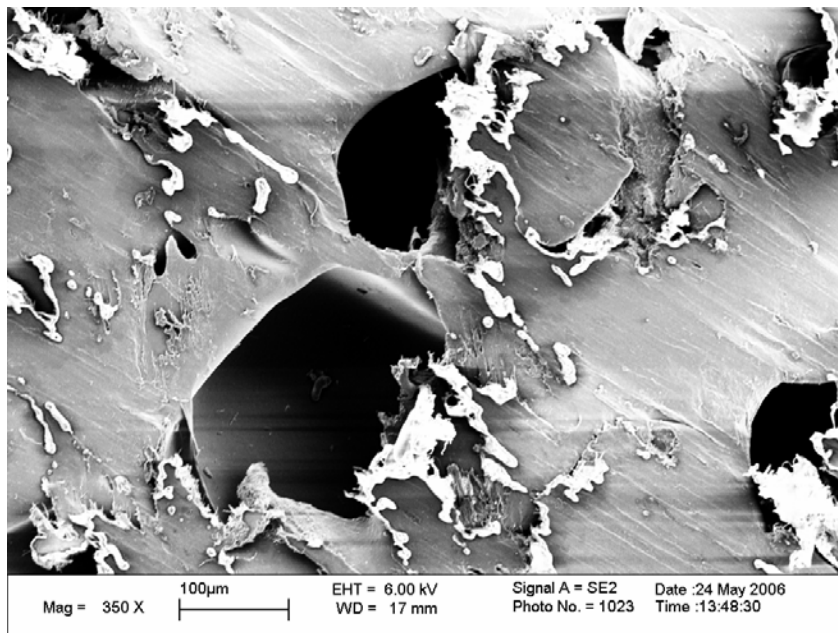


Figure 2.3. SEM micrograph of H200 foam, where cell wall thickness is measured as $\sim 30\mu\text{m}$

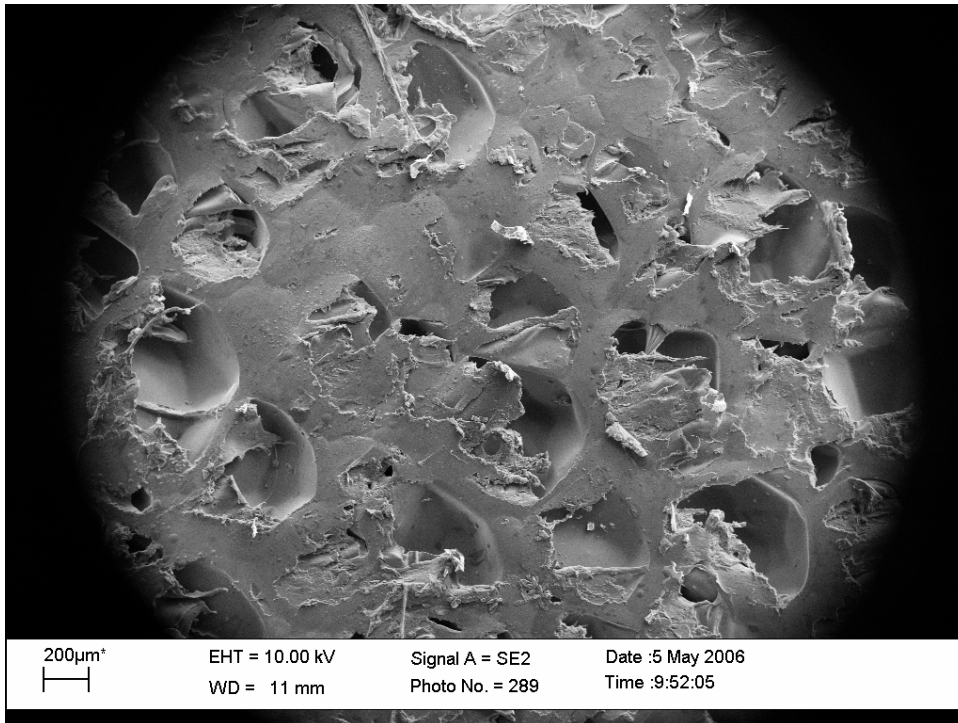


Figure 2.4. SEM micrograph of H250 foam, where cell wall thickness is measured as ~100 μm

Table 2. Dimensions of the cell diameter and wall thickness of the DIAB foams

	H130	H160	H200	H250
Cell diameter (μm)	130	160	200	250
Cell wall thickness (μm)	11	13	30	100

2.3 Ultrasonic Characterization Technique for in-situ Measurement of Wave Speeds

Ultrasonics generally refers to sound waves in solids with a frequency higher than 20 kHz. Ultrasonic testing of materials has been used extensively since its introduction in the early 1940s (Krautkramer, 1969). The principle behind ultrasonic testing is that a material's sound wave speeds are intrinsically associated with its physical and mechanical properties. Therefore, the material properties can be calculated by measuring the time an ultrasonic wave takes to travel through a known distance in the sample of a material. Most importantly, this information can be obtained without damaging the material itself in a nondestructive manner.

Ultrasonic techniques have been extensively used in the characterization of the elastic properties of crystalline solids. Two examples from the vast literature in this field are the papers by Hiki *et al* (1981) and Nikitin *et al* (1983). Hiki *et al* (1981) used ultrasonic testing to determine the higher order elastic constants of crystalline solids, and Nikitin *et al* (1983) measured the third order moduli of polycrystalline copper. More recently, Walter *et al* (1995) used two ultrasonic transducers *in-situ* to track longitudinal and shear wave speeds in unidirectional ceramic composites subjected to uniaxial tension, which were then used to identify damage zones in those materials. The transducers in their study were mounted transverse to the specimen while it was being subjected to uniaxial tension. Ashman *et al.* (1987) used the continuous wave mode to measure the elastic modulus and shear modulus of cancellous bone under loading. The speed at which the longitudinal and shear waves travel through a material can be used in the characterization of materials. Longitudinal (L) or dilatational (D) or primary (P) waves are those which produce oscillations in the direction of propagation of the wave. Shear (S) or equivoluminal or secondary waves are waves which produce oscillations perpendicular to the direction of propagation. For further discussion of wave propagation in solids, one may refer to the books by Kolsky (1949).

There are several different methods for producing ultrasonic waves, including piezoelectricity, electrostriction, magnetostriction, and laser irradiation. Piezoelectric effect,

discovered by the Curie brothers in 1880, is the most commonly used method of generating ultrasonic waves. The piezoelectric effect is the phenomena that when a potential is applied between two opposing faces of a piezoelectric crystal, a strain is induced in the material. An ultrasonic transducer is a device that contains a piezoelectric element sandwiched between two metallic plates that act as electrodes and can also support stress. Piezoelectric elements are cut from an oriented crystal chosen so that either the longitudinal or transverse waves are emitted perpendicular to the flat faces of the transducer. Commercially available transducers send and receive their signals through an integrated connector. Further details of ultrasonics and measurements can be found in the book by Krautkramer (1969).

Since each transducer can both produce and receive an ultrasonic pulse, several different transducer configurations have been used to acquire the transit times of sound waves in solids. The pulse echo (PE) mode is one of the more popular methods for measuring sound wave speeds. The method uses a single transducer to send and receive the longitudinal or shear pulse through a material. A variation of this method is the transmission mode, (TM) which uses two ultrasonic transducers: the first sends a pulse, and the second receives the corresponding transmitted pulse after having propagated through the solid.

Ultrasonic waves travel through metals easily because of the uniform and dense structure of the material. However, cellular materials such as foams are inhomogeneous and have large voids in them that hinder waves from traveling easily through such a material, causing scattering. The ultrasonic signal is highly attenuated in these types of materials. The most common method of ultrasonic characterization, the pulse echo mode, will be relatively ineffective in the characterization of foams because the signal must travel from the transducer, through the sample, reflect off the opposite face of the sample and then return to the transducer to be measured. Due to the high attenuation of the foam material, the signal would be highly attenuated before it returned to the pulser. A better choice for characterizing foams is to make use of ultrasonic testing in the transmission mode (TM). This method requires the ultrasonic wave to travel from one transducer (pulser) through the material and be captured by another transducer (receiver) located on

the other side of the material. This would require the signal to travel only once through the material, therefore minimizing the amount of scattering and attenuation of the signal.

Even with the reduced attenuation from the transducers being used in transmission mode, the material must be relatively thin to minimize the extent of attenuation. This presents some difficulty in the placement of the transducers because the transducers themselves have finite dimensions. The smallest transducers that are readily commercially available are 1/8" in diameter. The specimens to be inspected using these transducers must therefore have at least 1/8" diameter. If the transducers are to be used *in-situ* to track damage in the materials during loading, the transducers must be small enough so as not to interfere with the fixture used to load the material. To track changes accurately in a material without interfering with its deformation process, it was determined that the transducers themselves must be aligned with the load train. This presented unique challenges for ultrasonic testing of materials under applied loading, including protecting the transducers during compression, and transferring the load around the transducers to the sample.

Longitudinal (c_d) and shear (c_s) wave speeds can be used to determine the two elastic constants, Young's modulus (E) and the Poisson's ratio (ν), for linearly isotropic, homogeneous materials, assuming the density (ρ) of the material is known independently. The two wave speeds can be expressed as

$$c_d = \left[\frac{(1-\nu)E}{(1-2\nu)(1+\nu)\rho} \right]^{1/2} \quad \text{Eq. (2.1)}$$

and

$$c_s = \left[\frac{E}{2(1+\nu)\rho} \right]^{1/2} \quad \text{Eq. (2.2)}$$

In order to determine the Young's modulus and Poisson's ratio for a material, both the longitudinal and shear wave speeds must be known. From Eqs. (2.3) and (2.4), the Young's modulus and Poisson's ratio can be determined

$$E = \rho c_s^2 \left(\frac{4c_s^2 - 3c_d^2}{c_s^2 - c_d^2} \right) \quad \text{Eq. (2.3)}$$

$$\nu = \frac{c_d^2 - 2c_s^2}{2(c_d^2 - c_s^2)} \quad \text{Eq. (2.4)}$$

2.4 Experimental Procedure

The ultrasonic fixture for simultaneously measuring the wave speeds of materials under compression is illustrated in Fig. 2.5. This fixture was developed to simultaneously apply a load to a specimen while protecting the transducers themselves from any type of mechanical loading. The fixture consists of two identical transducer case assemblies, one for the pulser transducer (located on top of the specimen) and one for the receiver transducer (located on the bottom of the specimen). The assembly itself consists of a cylindrical steel casing with a circular hole on one end that fits around the loading rod. A smaller opening on the opposite end is covered by a spacer. Inside the steel casing, a steel housing with a central hole holds and protects the ultrasonic transducer. The loading force from the loading rod is transferred through the steel housing and spacer to the specimen, leaving the transducer free from carrying any loading force. The ultrasonic wave from the top shear transducer passes through the first spacer, the specimen, the second spacer, and then finally reaches the receiver transducer. A compressed spring is located behind each of the transducers to maintain contact between the transducer face and the sample. A setscrew behind the spring can be used to adjust the amount of pressure applied to the transducer, while also holding the spring in place.

The spacer located between the pulser transducer and specimen splits the shear wave into both longitudinal and shear waves, therefore allowing the simultaneous measurement of both waves during the experiment. This wave splitting occurs due to mode conversion of the incident shear (SV) wave due to the couplant that is used between the pulser transducer and the spacer. The couplant that is typically used is honey, a high-viscosity fluid. This results in a small amplitude P-wave (longitudinal) and a relatively larger amplitude SV-wave (shear). These two waves propagate through the sample and are then sensed by the receiver. The discovery of the wave splitting and the resulting simultaneous measurement of the longitudinal and shear waves are described in the following section. The signals from the pulser and the receiver can be seen in Fig. 2.6.

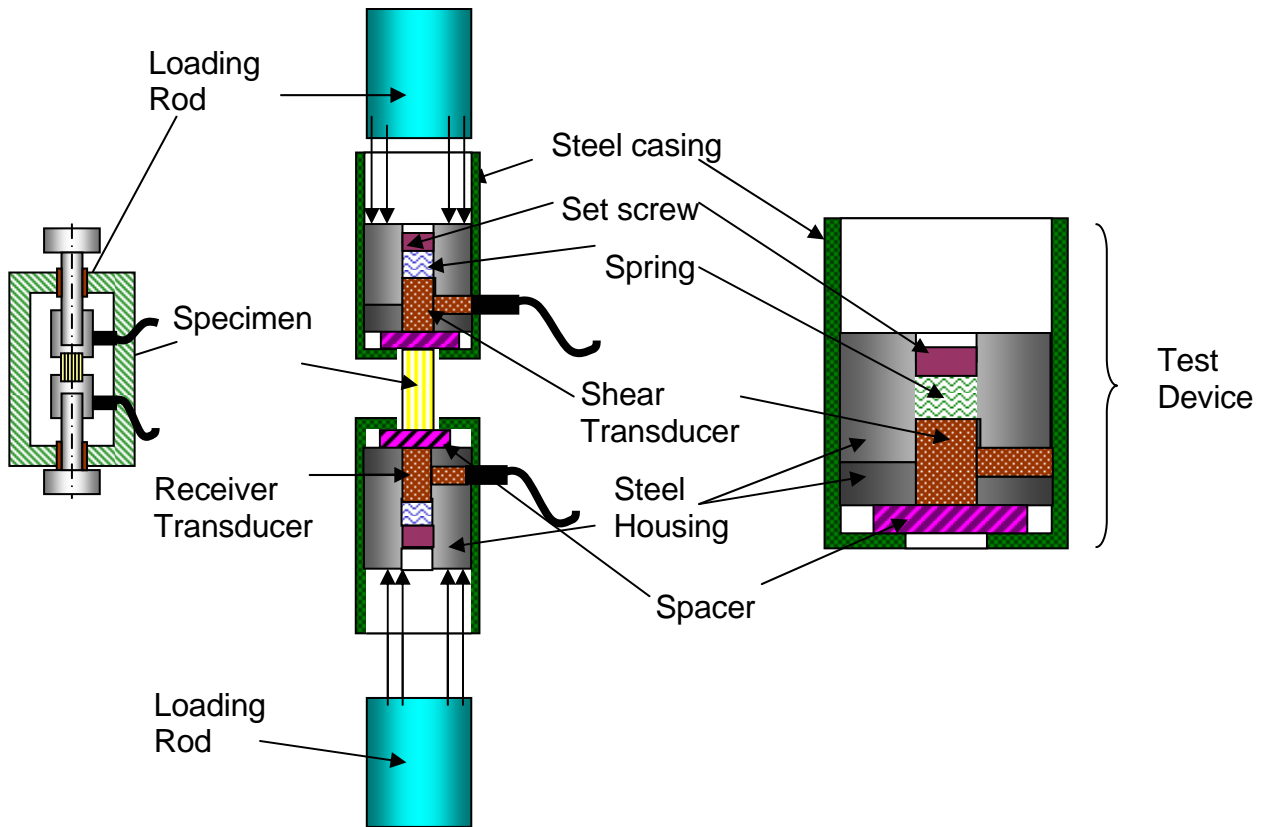


Figure 2.5. Loading fixture and protective housing of ultrasonic transducers for in-situ measurement of wave speeds while subjecting the specimen to uniaxial compression.

The spacers used in the transducer assembly are typically tungsten disks with a nominal thickness of 1 mm. The dimensions of all the samples studied were cylindrical and had a height of $9.46 \pm .12$ mm and diameter of $9.48 \pm .03$ mm, thus having a length to diameter ratio of ~ 1 . Two 5 MHz piezoelectric shear transducers with a face diameter of 1/8 inch, manufactured by Parametrics, Inc. (Waltham, MA) were used in this experiment. The pulse generator model# 5052A, also manufactured by Parametrics, Inc., has a peak voltage output of 300 V. The data acquisition card that recorded the signals from the transducers was the Gage model# 8200G (Montreal, Canada), which had a sampling rate of 1 GSample/s. The software used to control the card was GageScope, Professional Edition 1.0. The MTS (Materials Testing System, Model# 110.19, Eden Prairie, MN), the device used to load the fixture, had a maximum load of 3 kip or 13,344 N. All tests were performed at a nominal strain rate of 10^{-3} s^{-1} . Ultrasonic measurements were initiated 10 seconds after loading of the material, and ultrasonic readings were then taken every 10 seconds until the end of the test.

2.5 Simultaneous Measurement of Longitudinal and Shear Wave Speeds

The longitudinal and shear wave speeds of a sample were measured experimentally during *in-situ* uniaxial compression of various materials. A transducer casing was developed to protect the transducer, while it took sound speed measurements through a material under compression. The design (Fig. 2.5) of the fixture, is discussed in the section above, called for a metal spacer between the sample and the transducer to prevent damage to the transducer from compression. Two transducers were operated in the transmission mode. The first test of the casing was conducted with a pair of shear transducers, on an aluminum sample. During this test, a small and yet discernible peak was observed prior to the expected arrival of the shear wave signal at the receiving transducer. Initially, the wave speed calculated from this small peak corresponded to the longitudinal wave speed of the material. In order to verify that the small peak discovered in the test was indeed longitudinal, a pair of longitudinal wave transducers was placed in the fixture to record the longitudinal wave signals of the same aluminum sample. The output signal of this test was

then compared to the output of that of the shear wave transducer, on the aluminum sample. The output data of both tests are shown in Figure 2.6. The time at which the peak is observed in the shear transducer receiver signal directly coincides with the time of the peak from the receiving longitudinal transducer. Notably, since the experiment was carried out using the transducers in the transmission mode, the longitudinal pulse must have originated at the interface between the pulser transducer and spacer, and traveled through the entire sample. This experimental discovery led to the development of a methodology for measuring both longitudinal and shear wave speeds simultaneously in a material either under *in-situ* loading conditions or without load for measuring elastic constants of materials.

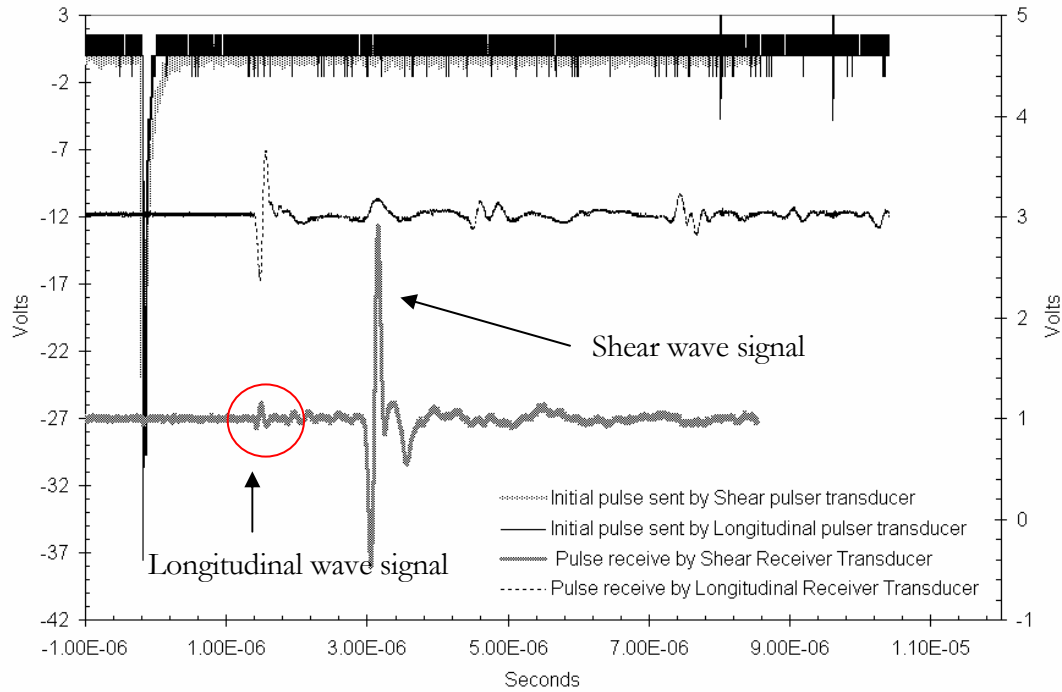


Figure 2.6. Input signal from a shear transducer and output signals of the longitudinal and shear receiving transducers from experiments on aluminum are plotted as a function of time. The output from the receiving shear transducer shows an anomalous peak that corresponds to the arrival of the longitudinal wave.

Additionally, Fig. 2.6, shows that there is a there a blip corresponding to the shear wave arrival in the longitudinal receiver signal as well. Tests were performed on copper and steel (Figure 2.7 and 2.8) as well and the anomalous longitudinal pulse in the shear signal as well as the anomalous shear signal in the longitudinal pulse were observed.

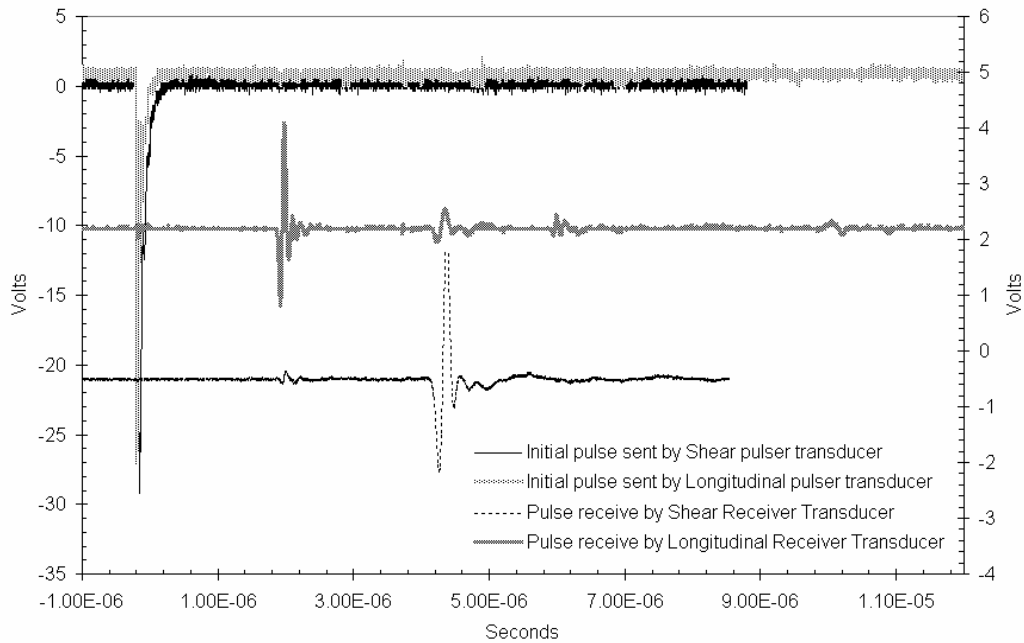


Figure 2.7. Input signal from a shear transducer and output signals of the longitudinal and shear receiving transducers from experiments on copper are plotted as a function of time. The output from the receiving shear transducer shows an anomalous peak that corresponds to the arrival of the longitudinal wave.

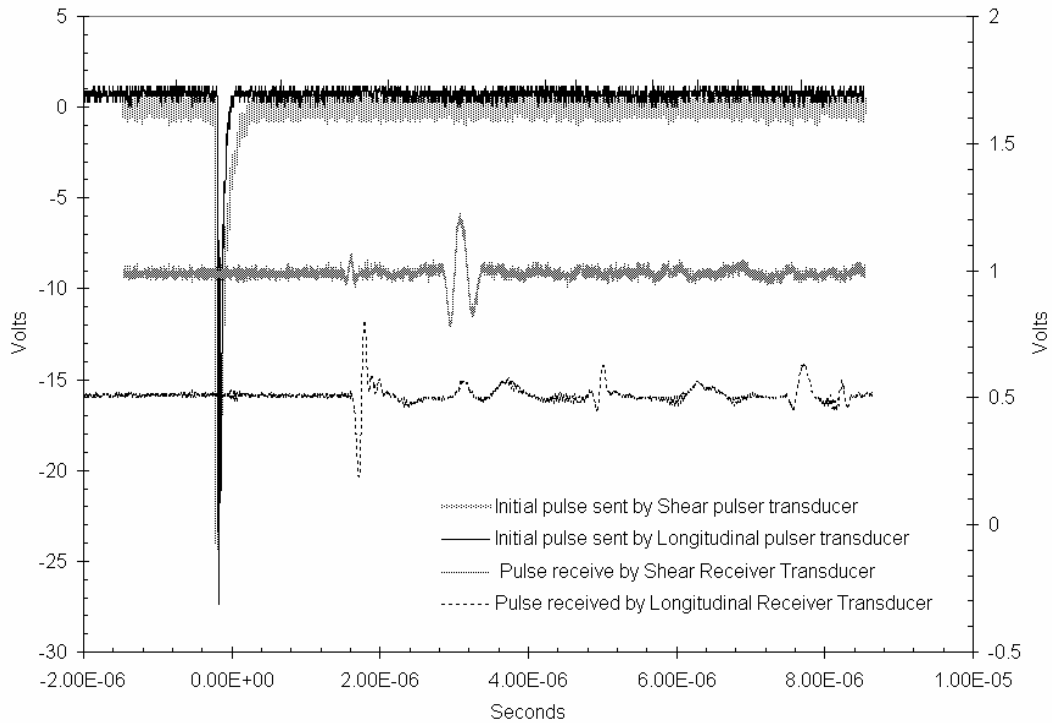
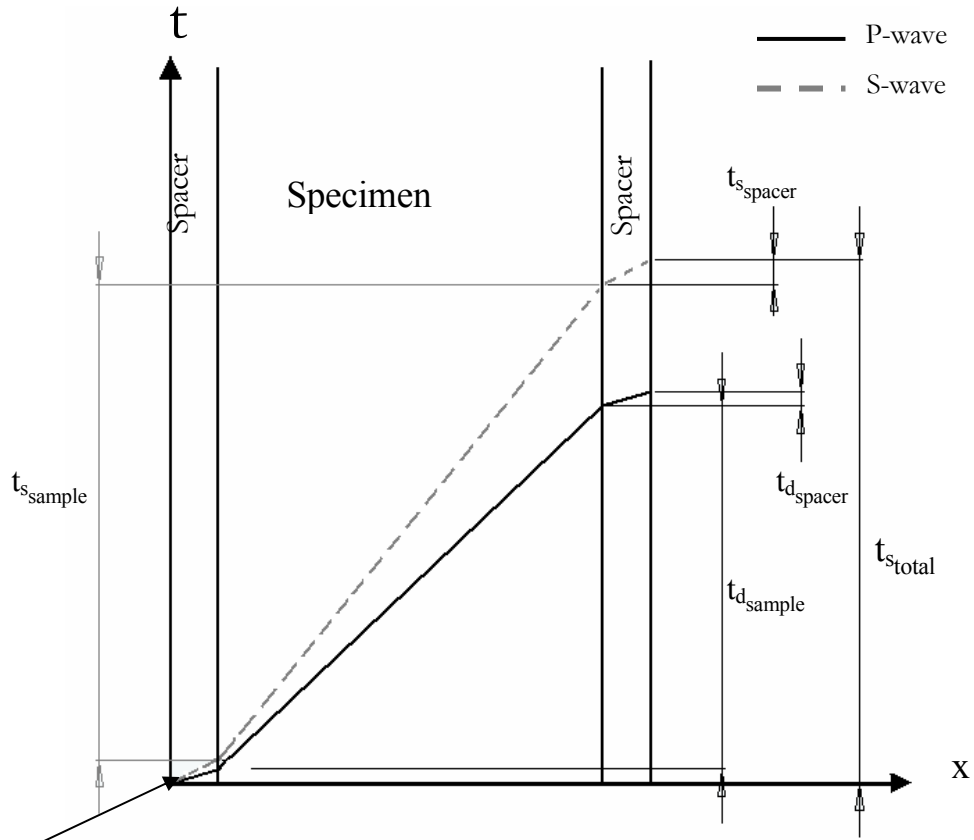
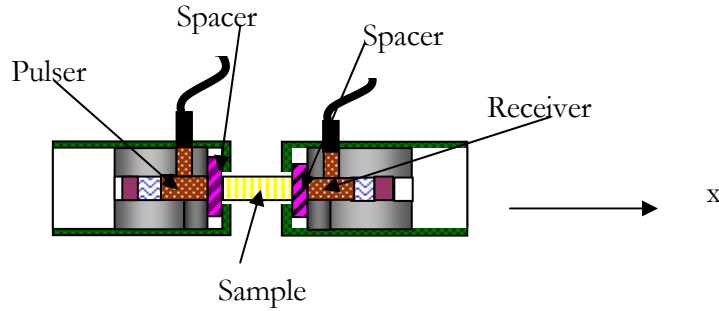


Figure 2.8. Input signal from a shear transducer and output signals of the longitudinal and shear receiving transducers from experiments on steel are plotted as a function of time. The output from the receiving shear transducer shows an anomalous peak that corresponds to the arrival of the longitudinal wave.

An x (distance)- t (time) diagram was constructed for the wave propagation in the experimental setup consisting of the spacers and the material. Figure 2.9, shows a small schematic of the test fixture on its side. As stated previously, there are spacers located between the pulser and the sample and the sample and the receiver, and the shaded region the x - t diagram corresponds to the sample location. The total longitudinal transit time of the longitudinal wave through the spacers and sample, $t_{d_{total}}$, is labeled in Figure 2.9. The transit time in the spacer, $t_{d_{spacer}}$, for both spacers is also labeled in Figure 2.9 along with the transit time in the sample, $t_{d_{specimen}}$. The shear transit times in the spacers, $t_{sspacer}$, and the sample $t_{sspecimen}$, are shown in Figure 2.9 as well as the total shear transit time, t_{stotal} . As the x - t diagrams indicates, it was hypothesized that while the piezoelectric crystal in the pulser shear transducer is polarized to generate only a shear wave, a small amplitude longitudinal

wave is also generated at the interface between the spacer and the transducer due to mode conversion, which propagates through the material and the spacer adjacent to the receiver.



Pulse Sent by Shear Transducer

Figure 2.9: x-t diagram of the experimental setup indicating total travel time of longitudinal wave through the first spacer the specimen and the second spacer

If this hypothesis was correct, the total transit time of the longitudinal pulse, $t_{d_{total}}$, measured by the shear transducer, should be the sum of the transit time in the specimen, $t_{d_{sample}}$, and twice the transit time of the spacer, $t_{d_{spacer}}$ of the longitudinal wave. To verify this relationship, true longitudinal wave transit time of the sample, without the spacers, was measured separately using a set of longitudinal wave transducers. Longitudinal transit times of the spacers alone, $t_{d_{spacer}}$, were also measured separately by using the longitudinal transducers. The total longitudinal transit time measured by the shear transducers was then compared to the longitudinal transducer measurement of transit time of the longitudinal wave in the sample alone. The difference between these two measurements was compared to the longitudinal transit times in the spacers. After making numerous measurements on aluminum, copper, polycarbonate and steel, the total transit time was indeed determined to be twice the transit time in the spacer, plus the transit time in the sample of the longitudinal wave.

Equation (2.5) demonstrates the relationship between the transit times of the longitudinal pulse measured by the shear transducers and those measured by the longitudinal transducers of the sample *and* the spacers. The relationship between the shear wave *transit* time measured by the shear transducer and the transit time measured by the shear transducer of the sample alone and the spacer alone, is described by Eq. (2.6). The equation shows that the shear transit time measured by the shear transducer is twice the transit time in the spacer plus the transit time in the sample of the shear pulse.

$$t_{d_{sample}} = t_{d_{total}} - 2t_{d_{spacer}} \quad \text{Eq. (2.5)}$$

$$t_{s_{sample}} = t_{s_{total}} - 2t_{s_{spacer}} \quad \text{Eq.(2.6)}$$

Once the transit times for the longitudinal and shear waves are gathered, their wave speeds can be calculated. Eqs. (2.7) and (2.8) demonstrate the method for determining the wave speeds (c_d and c_s) by dividing the specimen height by the transit time.

$$c_d = \frac{H_{sample}}{t_{d_{sample}}} \quad \text{Eq. (2.7)}$$

$$c_s = \frac{H_{sample}}{t_{s_{sample}}} \quad \text{Eq. (2.8)}$$

Equations (2.1) and (2.2) show that wave speeds can be used to calculate the Young's modulus and Poisson ratio of a material. Longitudinal and shear wave speeds calculated exclusively from shear transducer's (receiver) output (Fig. 2.6) were then used to calculate the Young's modulus and Poisson's ratio of the specimens using Eqs. (2.3) and (2.4).

To determine the wave speeds of a material at a given instant of time, it was necessary to capture both the incident pulse sent by the pulser transducer and the longitudinal and shear pulses captured by the receiver transducer. Since the longitudinal and shear wave speeds of the materials of interest were in the 890 to 6,300 m/s range, as presented in Table X, the ultrasonic frequencies needed to measure these speeds were in the megahertz (MHz) range. Hence, the signals needed to be measured at a very high rate. The device used to capture the signals, the Gage Scope 82G, had a sampling rate of 1 Gigasample/sec. Each digitized signal consisted of 1960 8-bit data points, and the time to acquire this data was around 1 ns.

Table 3. Measured wave speeds for selected engineering solids under no loading.

	Polycarbonate m/s	Aluminum m/s	Copper m/s	Steel m/s
c_d	2300	6300	5100	5900
c_s	890	3100	2500	3200

The results of the experiments on aluminum, polycarbonate, copper and steel at 0 strain can be seen in Figs. 2.10 and 2.11. In order to verify the accuracy of the Young's modulus calculated from the transducers, the results were compared with mechanically obtained Young's modulus. Compression tests were performed on aluminum, polycarbonate, copper and steel at a strain rate of $10^{-3}/s$ in a materials testing system (MTS, Model# 662.10A-08) without the ultrasonic fixture. The measured load-displacement data were corrected for compliance and then the Young's modulus was calculated from the slope of the linear portion of the nominal stress-strain curve. The results of the compression tests were compared with those from the ultrasonic tests in Fig. 2.10 and Figure 2.11. The figure shows that the methodology developed here with the pair of shear transducers accurately measured the Young's modulus of the materials of interest.

The axial and lateral strains were measured using strain gages mounted on the samples. The negative of the ratio of the lateral strain to the axial strain in the linear range was calculated to find the Poisson's ratio. The results were plotted against the ultrasonically-measured values of Poisson's ratio in Fig. 2.11, and the data indicate that the ultrasonic measurements for the Poisson ratio were also accurate.

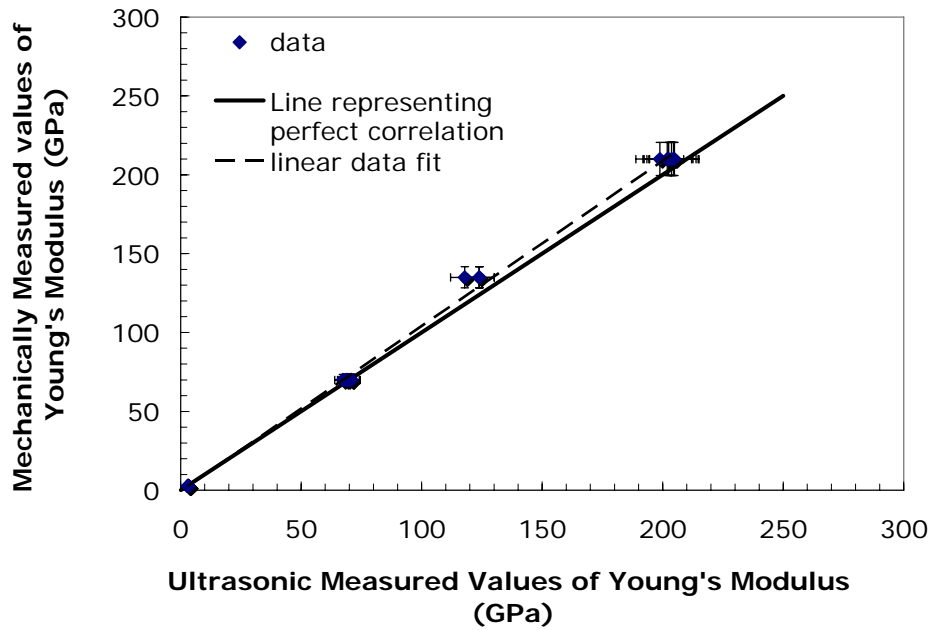


Figure 2.10: Comparison between ultrasonically-measured and mechanically measured Young's moduli of Steel, Polycarbonate, Copper and Aluminum.

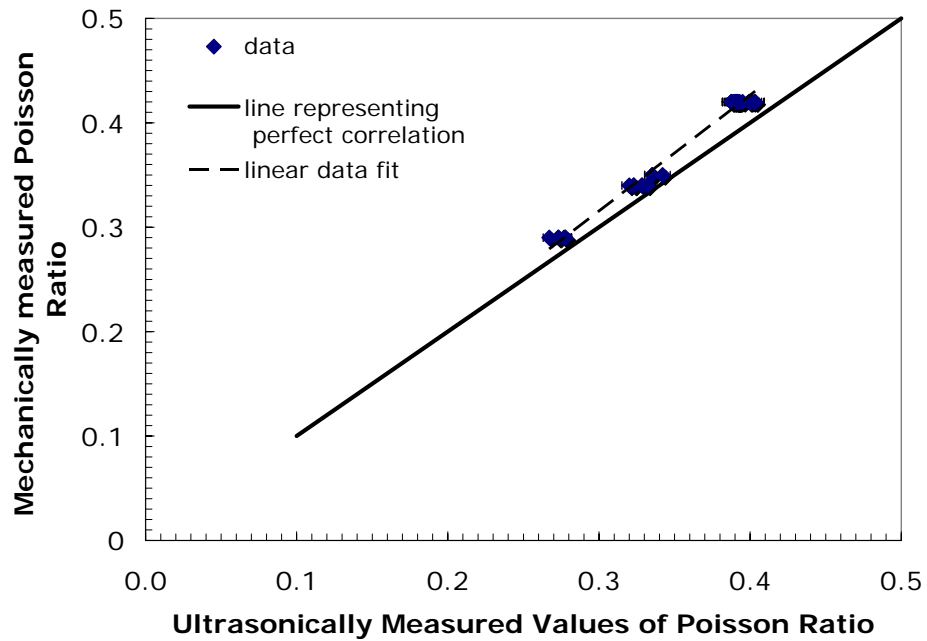
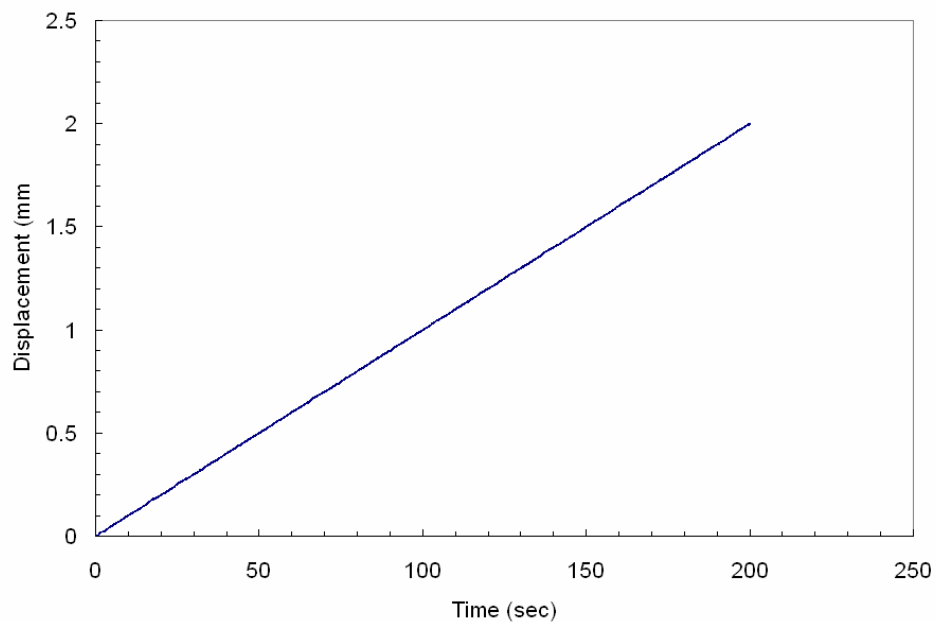


Figure 2.11. Comparison between Ultrasonically-Measured and Mechanically Measured Poisson Ratio of Steel, Polycarbonate, Copper and Aluminum.

The goal of this experimental effort is to measure longitudinal and shear wave speeds simultaneously during compression. During the compression tests, specimen heights decrease which must be taken into account when calculating sound speed for the material. Ultrasonic measurements are initiated 10 seconds after the beginning of the compression test, and subsequent readings are taken every 10 seconds until the test is complete. Figure 2.15a shows displacement as a function of time, as recorded by the materials testing system (MTS). The displacement is then corrected for compliance, the results of which are available in Fig. 2.12b. The specimen height is then subtracted by the amount of displacement at the time of the reading and the resultant height is used in equations 2.7 and 2.8 to calculate the longitudinal and shear wave speeds for the material.



(a)

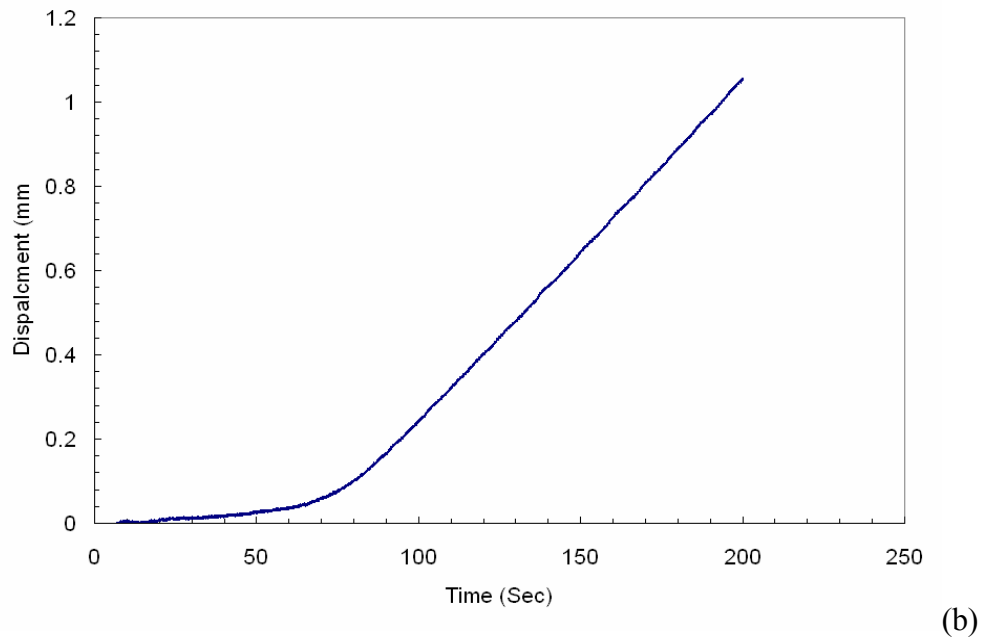


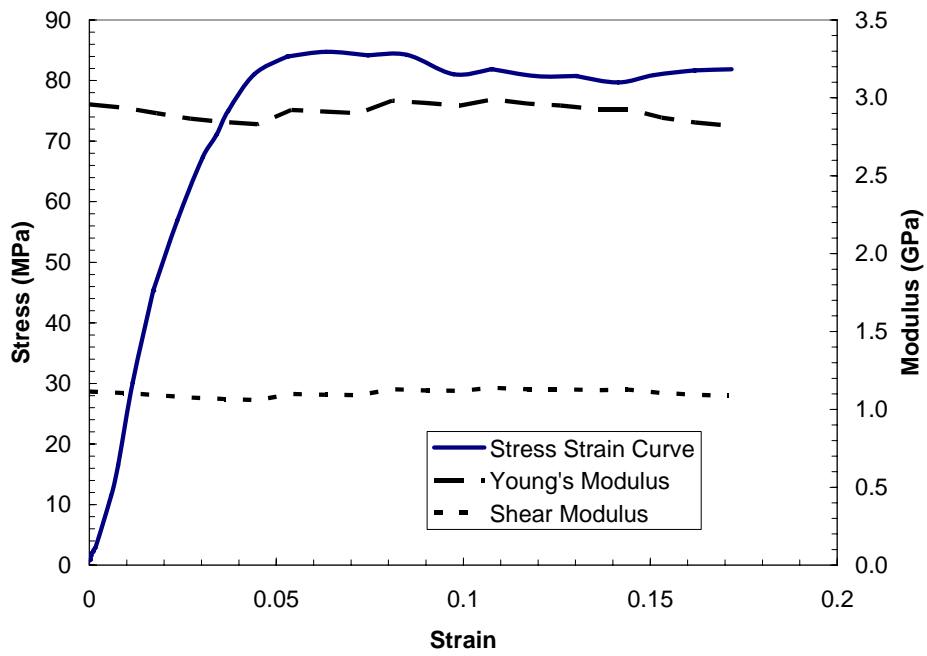
Figure 2.12: (a) Displacement versus time graph for the aluminum compression experiment (b) Compliance corrected displacement versus time graph for the aluminum compression experiment

2.6 Experimental Results and Discussion

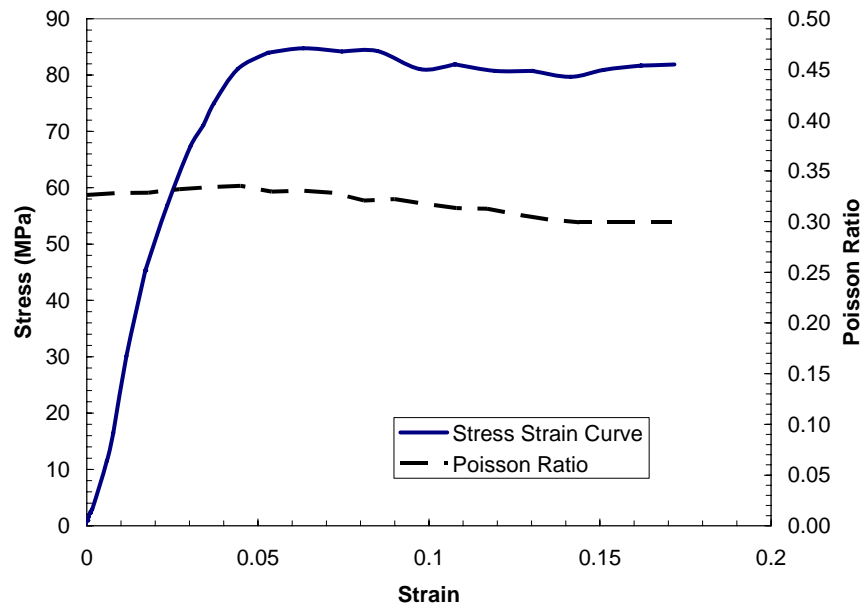
The main purpose of the construction of the in-situ ultrasonics experimental setup was to measure the wave speeds during compression. The wave speeds can then be used to compute the material constants; for example, the Young's modulus and the Poisson's ratio of a linearly elastic material. The test fixture designed to house the transducers was combined with springs and face plates to protect the ultrasonic transducers during compression. Tests to confirm the accuracy of the measurements of both the longitudinal and shear wave speeds during compression were conducted on polycarbonate, steel, aluminum and copper. Measurements of the longitudinal and shear wave speeds in the material were taken every 10 seconds, while the duration of the entire test lasted 200 seconds. After the tests were completed, several files needed to be analyzed. A program

was written in the computer program *Matlab* to automatically track and record the longitudinal and shear wave pulse time for each sample as well as the incident pulse time (Fig. 2.6). The program then subtracts the time of the incident wave from the time of the longitudinal peak, and that is recorded as t_d . The same is done to calculate the shear wave time, t_s , this time using the shear peak arrival time instead of the longitudinal peak time. The transit times of the longitudinal and shear wave in the sample are calculated by using Eqs. (2.5) and (2.6). The wave speeds are then computed using Eqs. (2.7) and (2.8) and using this data, the elastic constants are calculated using Eqs. (2.3) and (2.4).

Figure (2.13) presents the results of the test performed on polycarbonate. The figure on the left is a plot of the stress-strain curve of the material gathered during the test along with the ultrasonically-measured Young's modulus and shear modulus, versus strain, and the plot on the right gives the stress-strain curve and the ultrasonically-measured Poisson's ratio versus the strain. The results of the aluminum, copper and steel tests are presented in Figs. (2.14), (2.15) and (2.16), respectively. Ideally, the Young's modulus and Poisson's ratio of these aforementioned materials should not change during compression through the plastic regime. The experimental results shown in Figs. (2.13) through (2.16) demonstrate that the Young's modulus, shear modulus, and Poisson's ratio do remain constant throughout the elastic-plastic regimes of deformation.

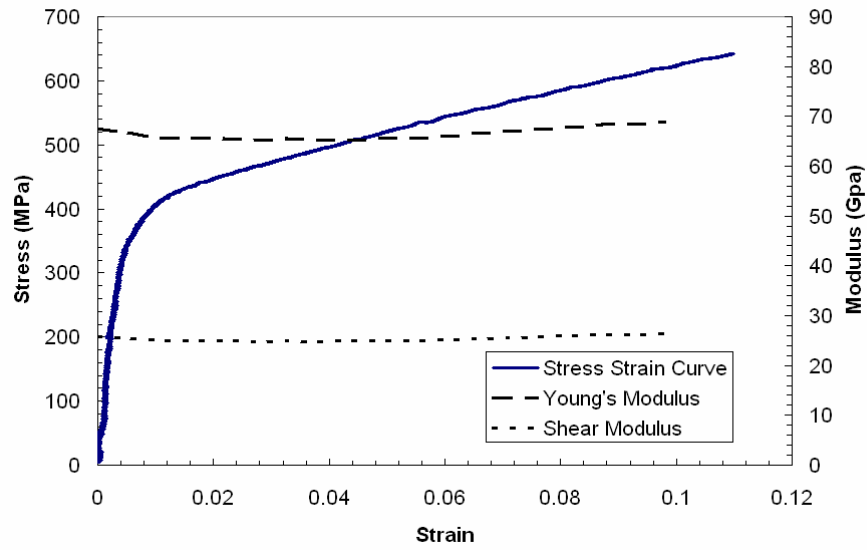


(a)

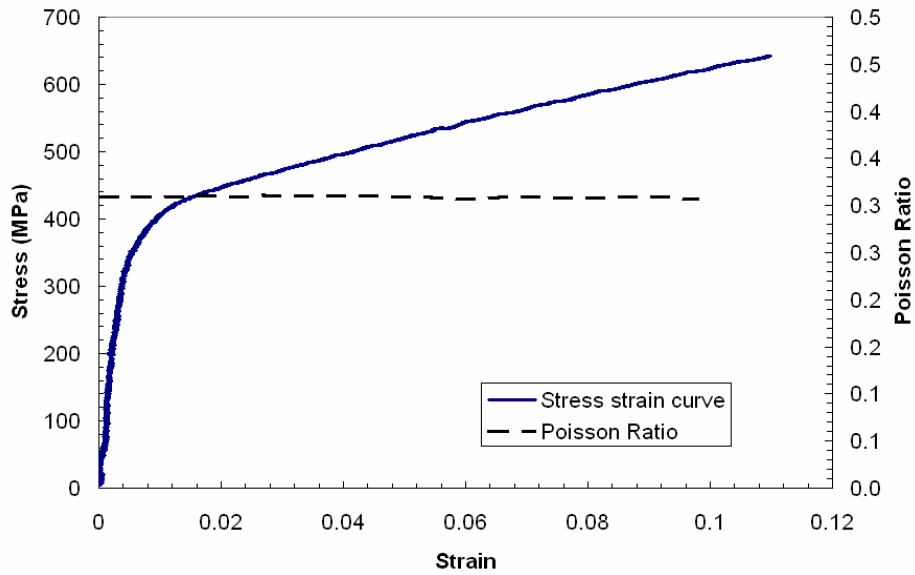


(b)

Figure 2.13. Young's modulus, shear Modulus and Poisson ratio for Polycarbonate during Uniaxial Compression.

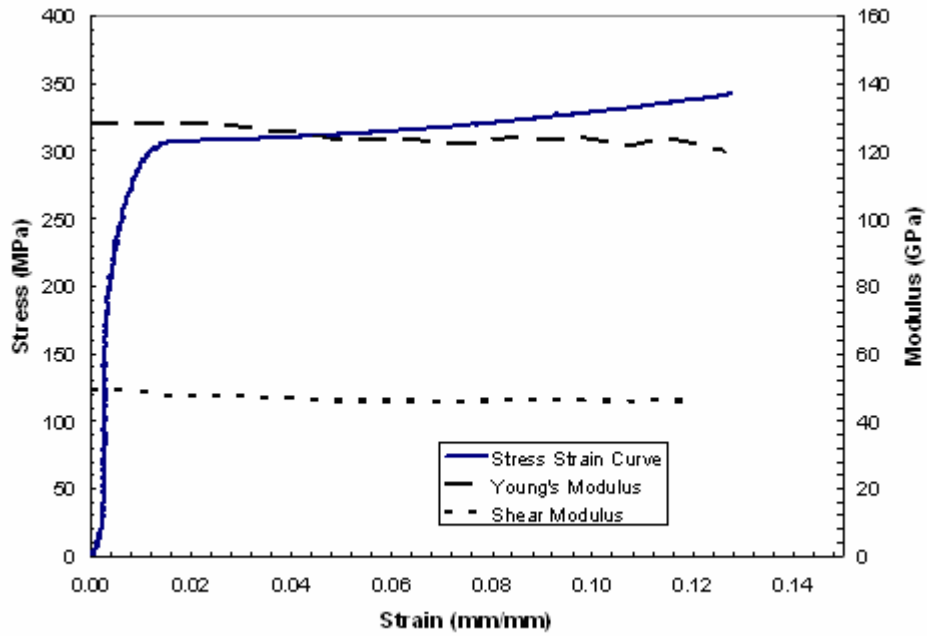


(a)

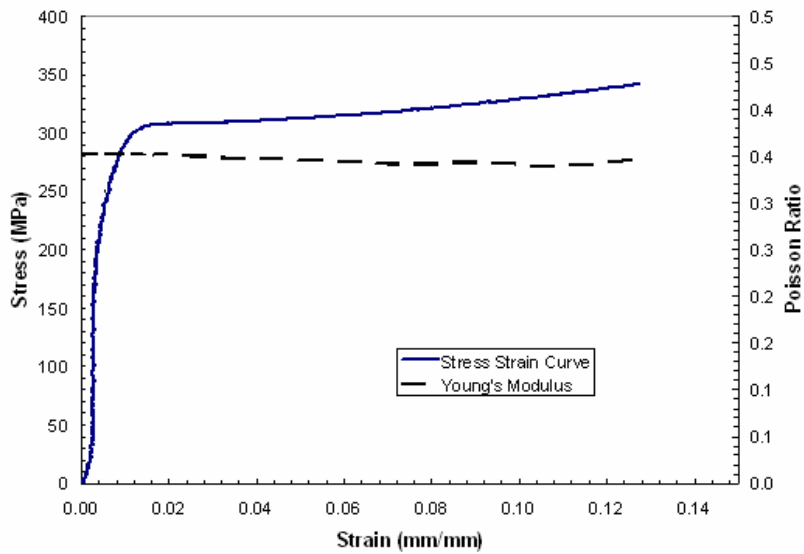


(b)

Figure 2.14. Young's Modulus, shear Modulus and Poisson's ratio for aluminum during uniaxial compression.

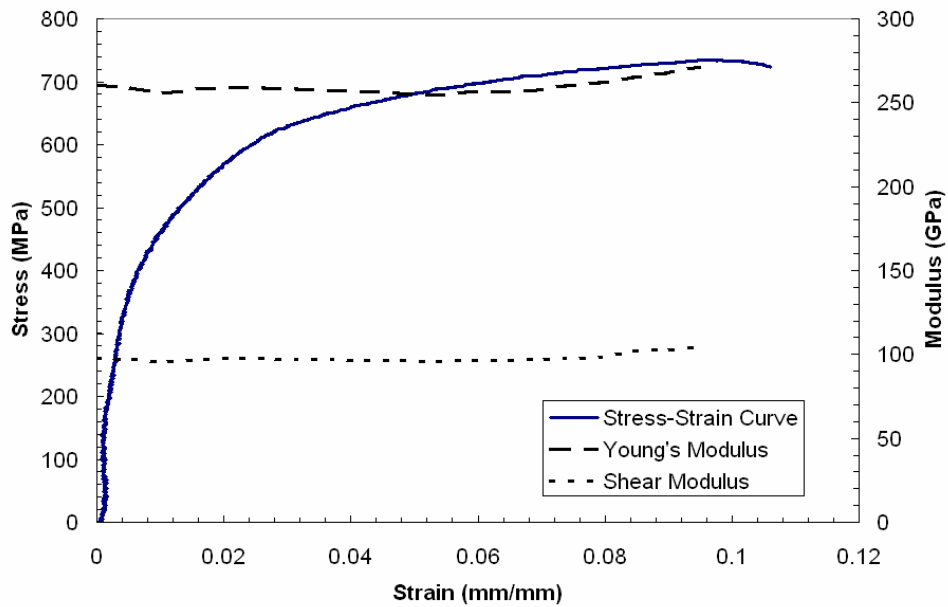


(a)

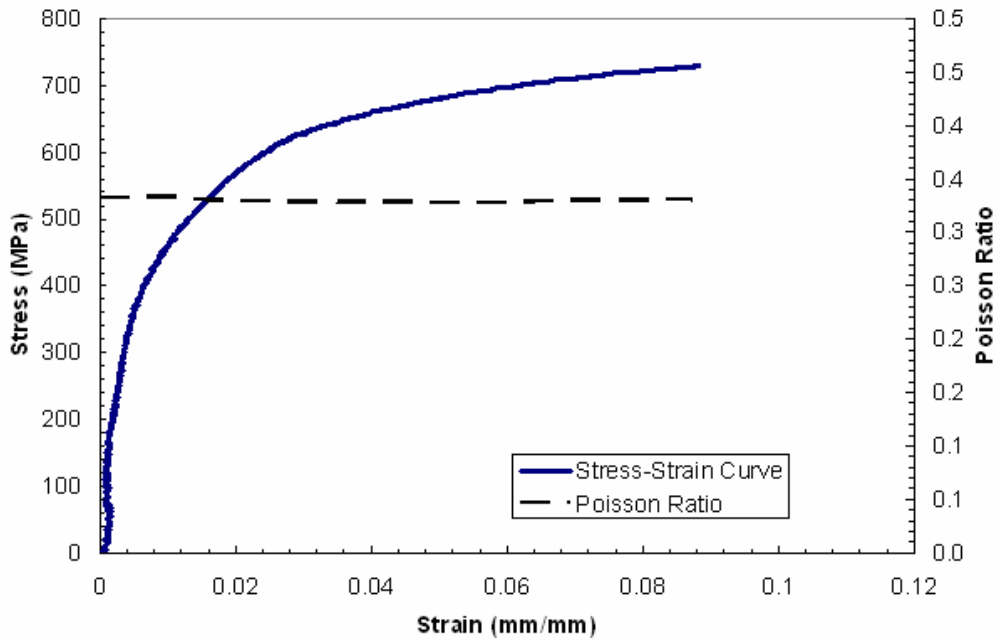


(b)

Figure 2.15. Young's modulus, Shear modulus and Poisson ratio for copper during uniaxial compression.



(a)



(b)

Figure 2.16. Young's Modulus, Shear Modulus and Poisson Ratio for Steel during Uniaxial Compression.

Once the method had been validated for fully dense isotropic solids (where the wave speeds are not expected to be a function of the deformation), the mechanical device was used to perform experiments on a set of polymeric foams ranging in density from 130 kg/m³ to 250 kg/m³. The calculation of the modulus for polymeric foams was similar to that of the isotropic solids, with the exception of the calculation of the density. For the isotropic solids the density remained constant; however, for the foams, the density would increase with compression as the cells full of air collapsed. Therefore, the modified calculation of the modulus is as follows,

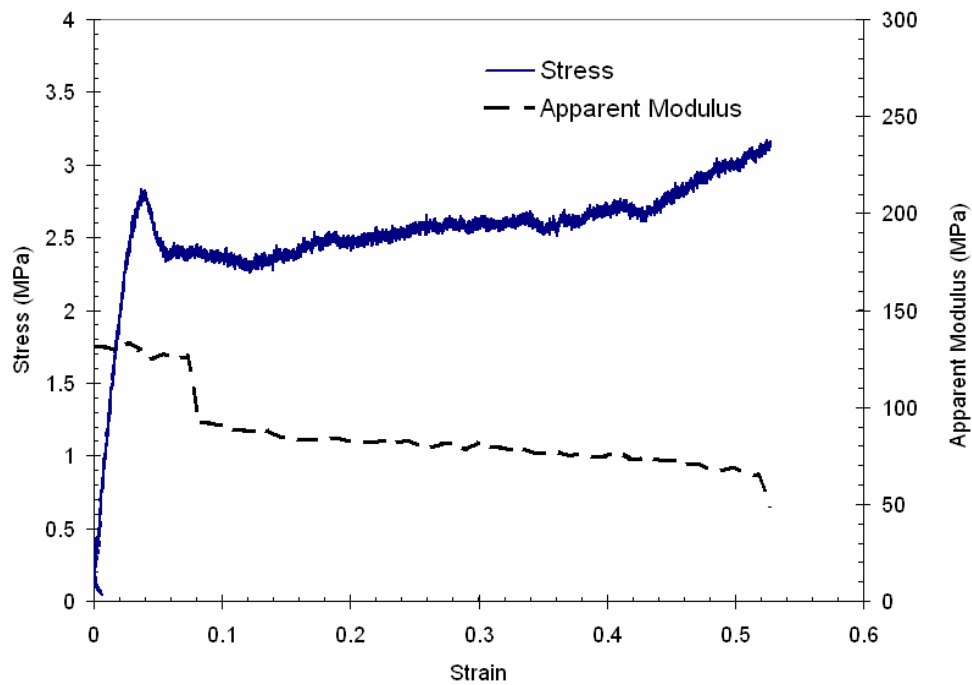
$$E = \frac{m(h_0 - \delta h)}{At_s^2} \left(\frac{4t_d^2 - 3t_s^2}{t_d^2 - t_s^2} \right) \quad \text{Eq. (2.9)}$$

Where m, is the mass of the sample, A is the cross-sectional area of the sample and h₀, is the original height of the sample, which is corrected by the change in height of the sample as read by the MTS machine, corrected for compliance.

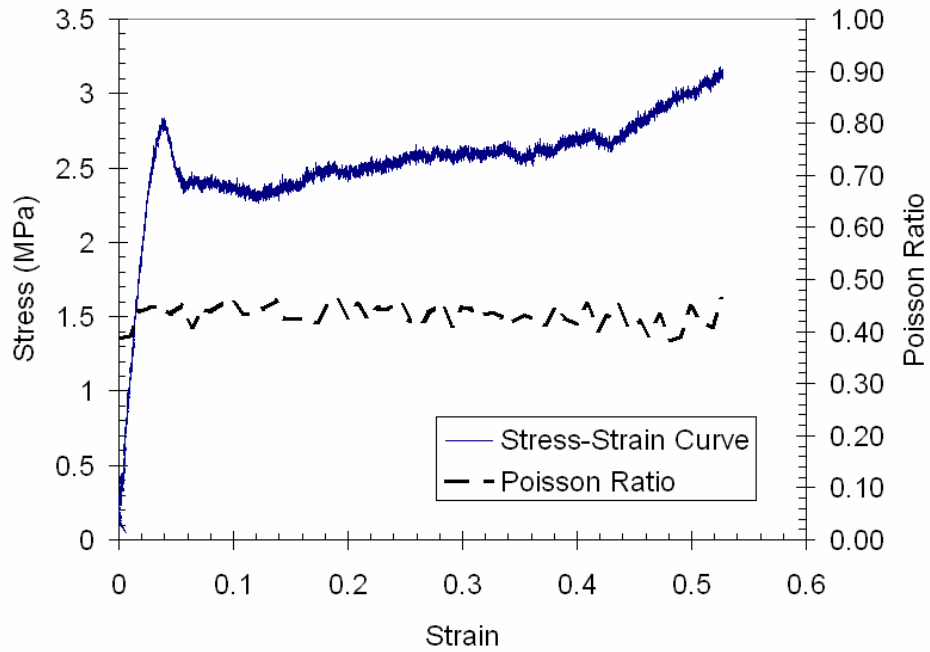
Upon loading each sample into the fixture, an application of honey ensured good contact between the sample and the fixture face plate and the face plate and the transducer face. Representative results for tests conducted on the H130, H160, H200 and H250 samples are presented in Figs. (2.17ab) and (2.18ab). The two lower density materials showed a sharp drop in the modulus during compression, while the higher density foams showed a more gradual decrease in the modulus without any significant discontinuities.

In Figure 2.17b, various states in the stress strain curve of low density foam are labeled. The first label, 1, corresponds to the maximum stress of limit stress of the material. It is at this point that the deformation begins to localize, in the case of elastic buckling. The deformation propagates to other rows of cells in 2 and 3. Finally, at 4, all the cells walls have buckled and then material is said to undergo densification. The steep turn in stress at 4 is due to the fact that the completely buckled sample now behaves as a solid block of the constitutive material of the foam. For the case of H130, the sudden drop in the apparent modulus with the peak in the stress-strain curve, which is known as the strength of the foam and the subsequent drop, are known to be due to elastic buckling. The drop in H160 is occurs at a larger strain than the H130 foam.

The stress strain curve of the two higher density foams is almost identical to the lower density foams. Indeed, from inspection of the stress strain curve alone, the distinction between elastic buckling and plastic collapse could not be observed. The stress strain curve has a maximum stress labeled as 1 on Figure 2.18, followed by the propagation of deformation in 2 and 3, in this case uniform collapse in all cells simultaneously, and finally densification, 4.

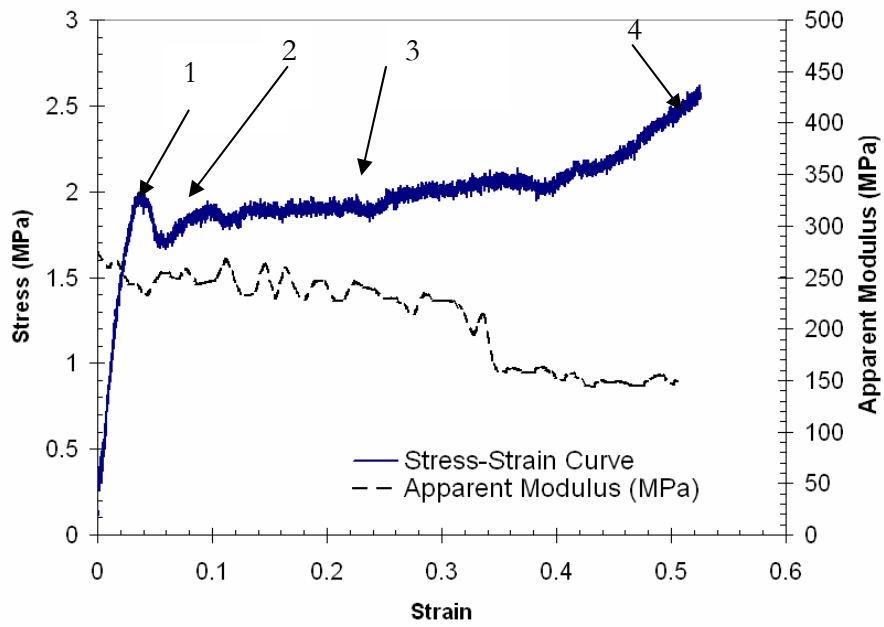


(a)

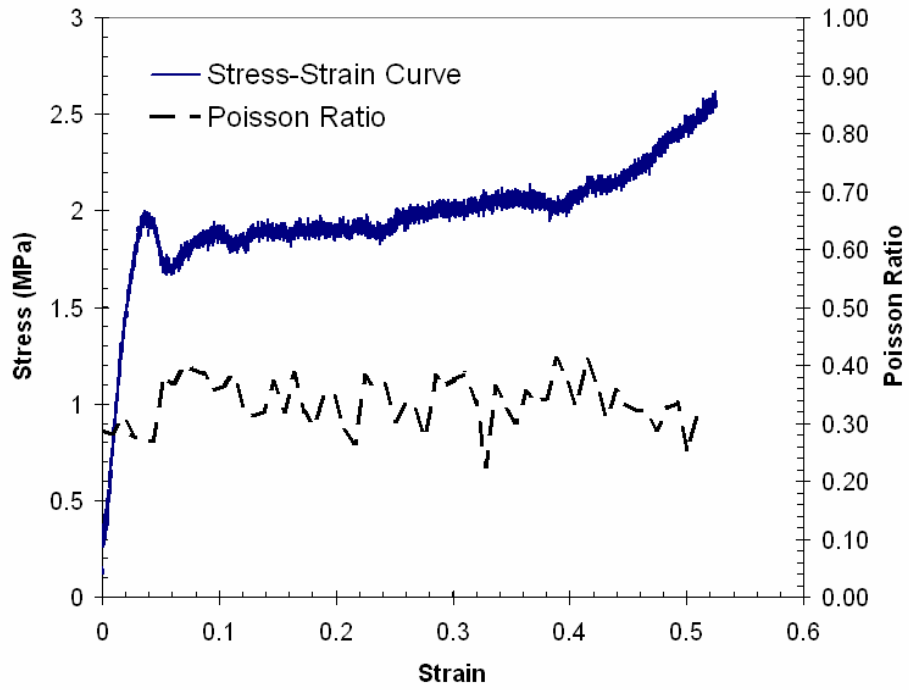


(b)

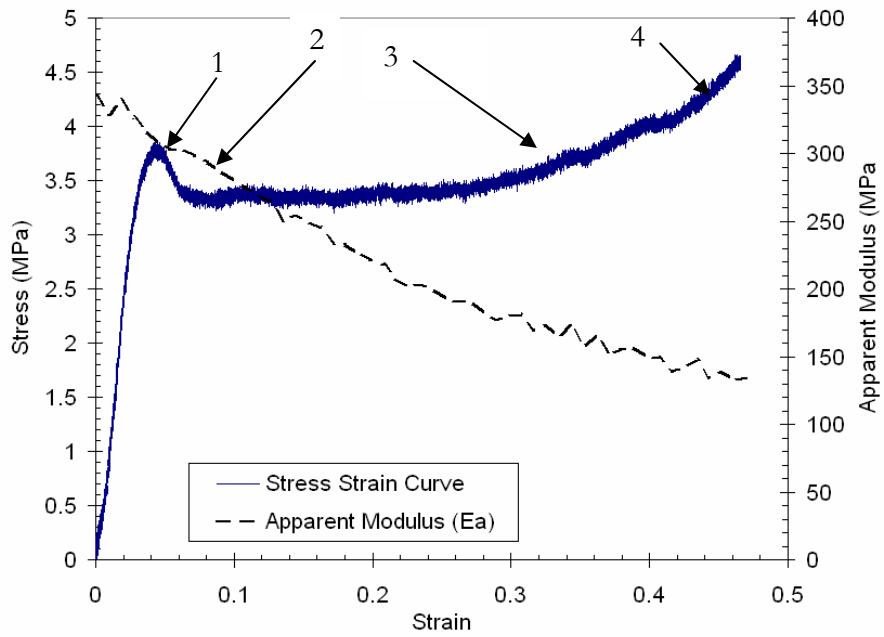
Figure 2.17. Plot of Ultrasonic Data for the low density foams 130 kg/m^3 density foam (a) Apparent Modulus (b) Apparent Poisson Ratio



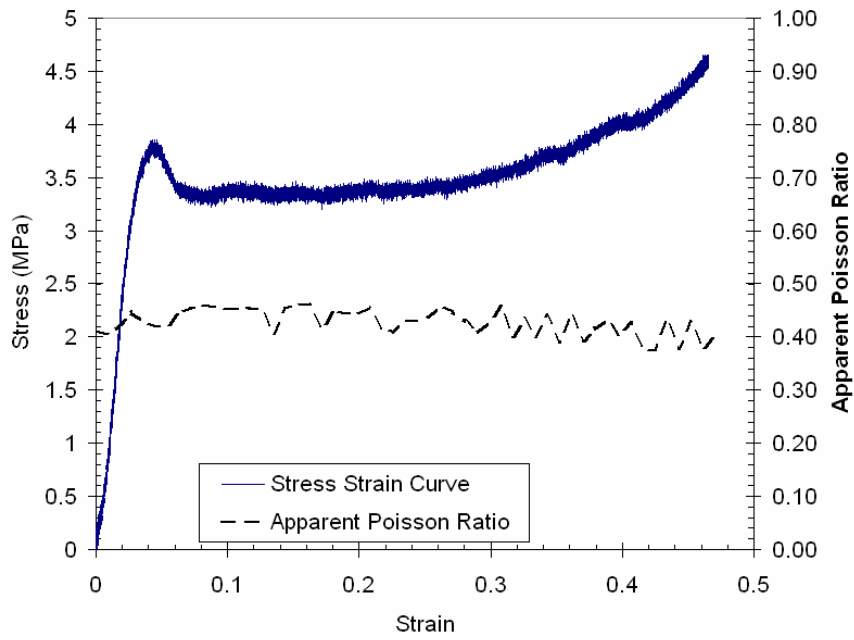
(a)



(b)
 Figure 2.18. Plot of Ultrasonic Data for the low density foams 160 kg/m^3 density foam (a) Apparent Modulus (b) Poisson Ratio

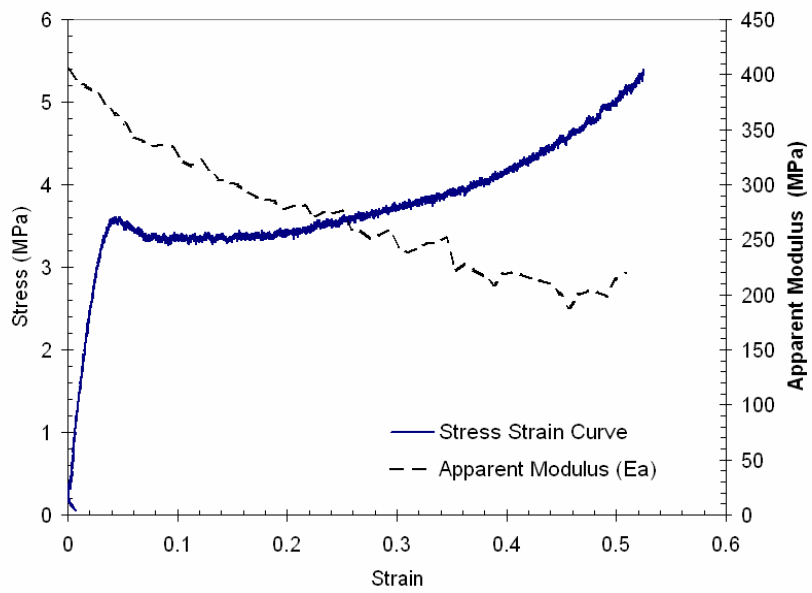


(a)

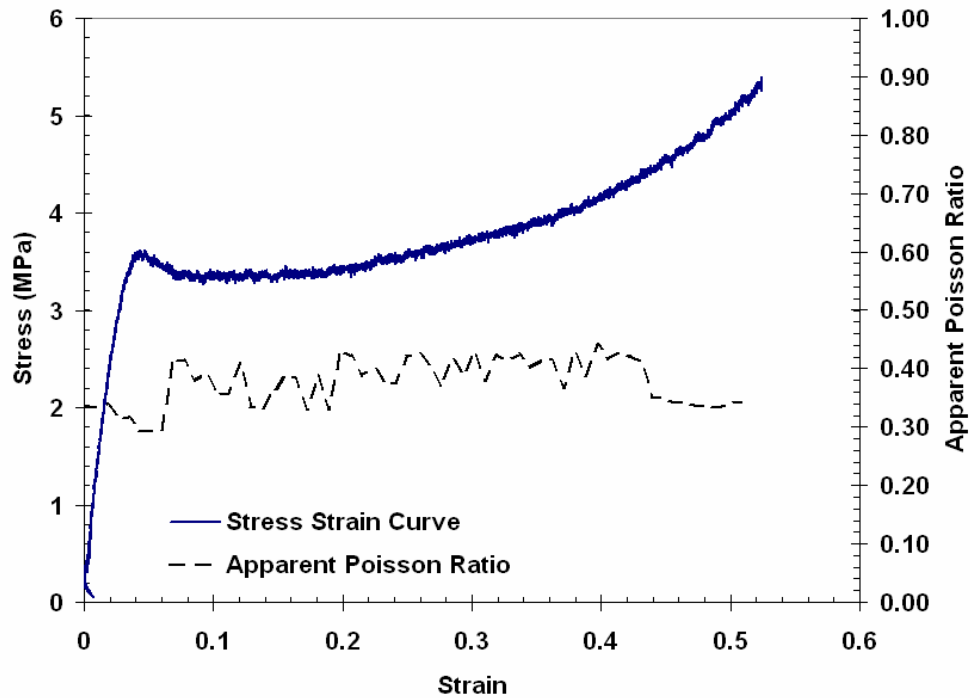


(b)

Figure 2.19. Plot of Ultrasonic Data for the low density foams 200 kg/m^3 density foam (a) Apparent Modulus (b) Apparent Poisson Ratio



(a)



(b)

Figure 2.20. Plot of Ultrasonic Data for the low density foams 250 kg/m³ density foam (a) Apparent Modulus (b) Apparent Poisson Ratio

From Table 2.1 at the beginning of the chapter, DIAB reports the Young's modulus of H130, H160, H200 and H250. A comparison of the ultrasonically-measured modulus at 0 strain and the published values of the Young's modulus of the various density foams is given in Figure 2.21. The ultrasonically-measured modulus at 0 strain is comparable with published values.

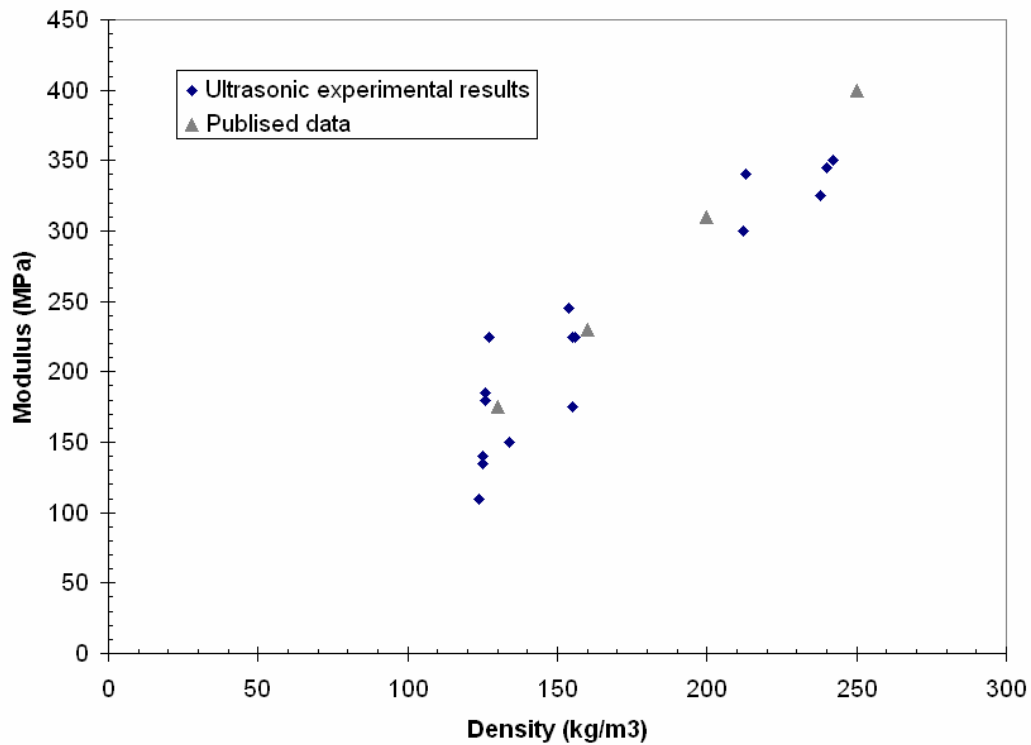


Figure 2.21 Ultrasonically-measured modulus at 0% strain and published values of modulus for various densities.

2.7 Model for Cell Failure

A simple hexagonal cell model from Gibson *et al* (1983) was utilized to understand the apparent jumps in the apparent modulus computed from ultrasonic data on the lower density foams (see Fig. 2.17ab and 2.18ab). A schematic of a two-dimensional hexagonal cell with a side length l , interior angle of 30° , wall thickness T , and depth, b is shown in Figure (2.22). Figure (2.23a) illustrates the deformed shape of the cell after a plastic collapse, while Figure (2.23b) illustrates the deformed shape after elastic buckling.

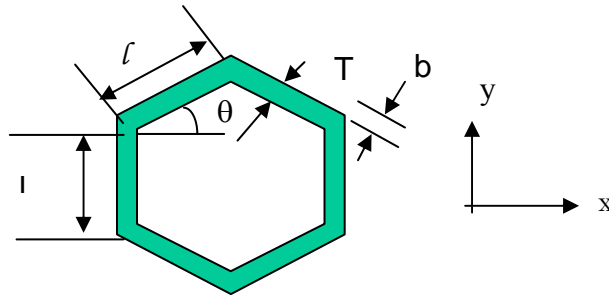


Figure 2.22: Schematic of 2D regular hexagonal cell

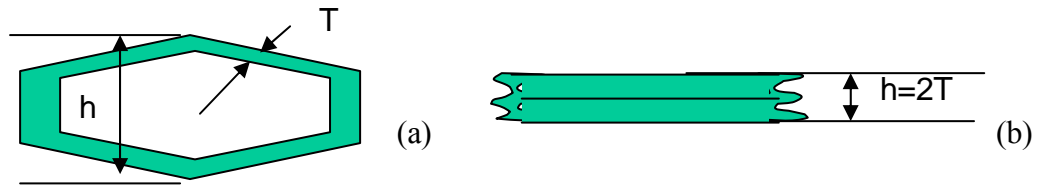


Figure 2.23: Illustration of the deformed regular hexagonal cell under (a) plastic collapse (b) elastic buckling

In the case of plastic collapse, the height of the cell decreases slowly, while under elastic loading, cell height decreases linearly under elastic deformation. Once the critical load is reached, however, the cell buckles and the height jumps to the fully collapsed height of the cell, twice the thickness of the cell wall in the idealized two dimensional case (Fig. 2.23b). The sample height during deformation is necessary for calculating the longitudinal and shear wave speeds in the material, demonstrated by Eqs. (2.7) and (2.8). As mentioned above, the height of the foam is measured by the testing machine, MTS. The resolution of the MTS displacement sensor is $63.5 \mu\text{m}$ while the average cell height is $200 \mu\text{m}$. The sound speeds of the sample is calculated by dividing the height of the specimen, read by the testing machine, by the transit time of the longitudinal and shear wave, read by the ultrasonic transducers. In order to determine the relationship between the height of the sample and the modulus, Eqs. (2.1) and (2.2) had to be rewritten, so that modulus was a

function of the wave speeds. Wave speeds then needed to be written in terms of the sample height and the longitudinal and shear wave transit times. The relationship between sound speed and transit time and height, having already been established in Eqs. (2.7) and (2.8), contributed to the rearrangement seen in equation (2.10). In the case of elastic buckling, the cell row will deform elastically and then buckle. When contact between the top and bottom cell walls occurs, no further compression of the cell is possible and deformation will continue in an adjacent cell row. Equation (2.11) presents the sample height as a function of time. The sample height, $h(t)$, is a function of the original height of the sample, h_0 , strain rate, $\dot{\epsilon}$, and the height of a single cell, h_{cell} . At some time, t_{crit} , the cell wall will buckle and the sample height will suddenly drop, due to the cell height's drop to twice the thickness of the cell wall (top cell wall touching bottom cell wall). The deformation of the sample will continue until the next row of cells buckle. The density of the sample will also be affected by the cell wall buckling, since the density of the sample is a function of the height of the sample Eq. (2.13). Eq. 2.14 presents the density as a function of the mass of the sample, m , the cross-sectional area of the sample, A , and the height of the cell as calculated in Eq. (2.11). Using Eq. (2.11) and Eq (2.14) in Eq. (2.10) the Young's Modulus of the sample as a function of time can be obtained. The Young's Modulus as a function of time for elastic buckling is presented in Eq. (2.15). For demonstration purposes, if $t_d=1$, $t_s=2$, $m=1$, $A=1$, $h_0=10$, $a=1$, $h_{cell}=0.5$, $t_{crit}=1$, the Young's Modulus as a function of time can be plotted as seen in Figure 2.24. The plot shows that at t_{crit} , the height will drop dramatically and then continue smoothly. In the case of plastic collapse, height decreases with increasing strain. However, since the height of the cell decreases gradually without catastrophic jumps as was seen in the elastic buckling case, so the height is represented as Eq. 2.12. The sample density Eq. (2.16) is calculated by using Eq. (2.13) and Eq. (2.12). The Young's Modulus Eq. (2.17) is obtained by using Eq. (2.12) (2.16) in Eq. (2.10). If we again use $t_d=1$, $t_s=2$, $m=1$, $A=1$, $h_0=10$, $a=1$, $h_{cell}=0.5$, $t_{crit}=1$ for demonstration purposes, the Young's Modulus as a function of height can be plotted, as presented in Figure 2.25.

$$E = \frac{h^2 \rho}{t_s^2} \left(\frac{4t_d^2 - 3t_s^2}{t_d^2 - t_s^2} \right) \quad \text{Eq. (2.10)}$$

$$h_{\text{elastic buckling}}(t) = (h_0 - \dot{\epsilon} t - h_{\text{cell}} * H(t - t_{\text{crit}})) \quad \text{Eq. (2.11)}$$

$$h_{\text{plastic collapse}}(t) = h_0 - \dot{\epsilon} t \quad \text{Eq. (2.12)}$$

$$\rho(t) = \frac{m}{A * h(t)} \quad \text{Eq. (2.13)}$$

Elastic Buckling

$$\rho(t) = \frac{m}{A(h_o - \dot{\epsilon}t - h_{\text{cell}} * H(t - t_{\text{crit}}))} \quad \text{Eq. (2.14)}$$

$$E(t) = \frac{m(4t_d^2 - 3t_s^2)(h_0 - \dot{\epsilon}t - h_{\text{cell}} * H(t - t_{\text{crit}}))}{At_s^2 (t_d^2 - t_s^2) * } \quad \text{Eq. (2.15)}$$

Plastic Collapse

$$\rho(t) = \frac{m}{A(h_o - \dot{\epsilon}t)} \quad \text{Eq. (2.16)}$$

$$E(t) = \frac{(h_o - \dot{\epsilon}t)m}{At_s^2} \left(\frac{4t_d^2 - 3t_s^2}{t_d^2 - t_s^2} \right) \quad \text{Eq. (2.17)}$$

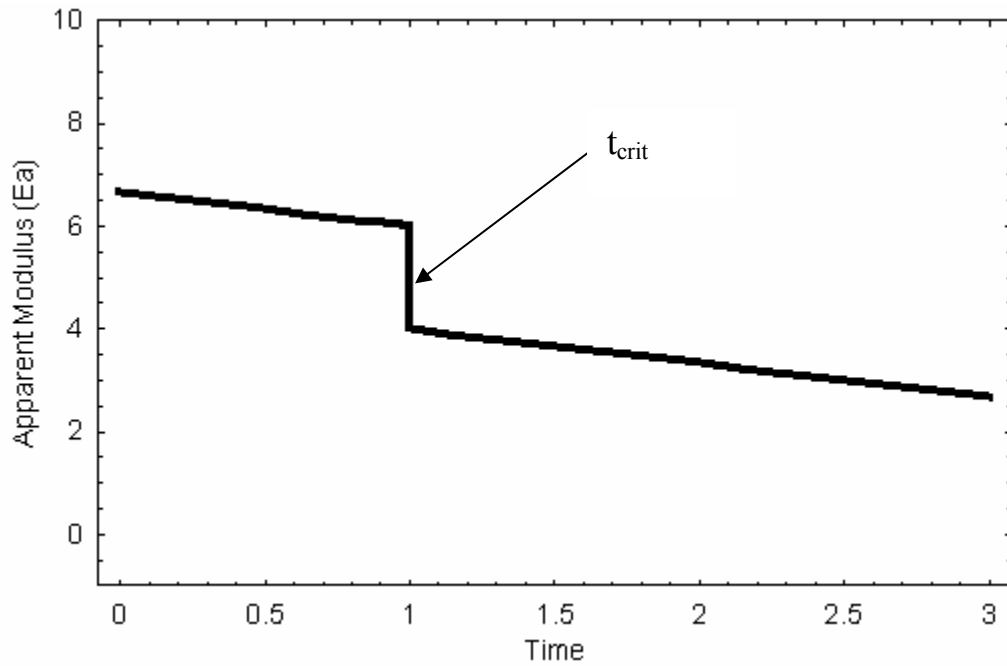


Figure 2.24. A plot of the Young's Modulus as a function of time is shown, with the drop in modulus due to drop in cell height at t_{crit} indicated.

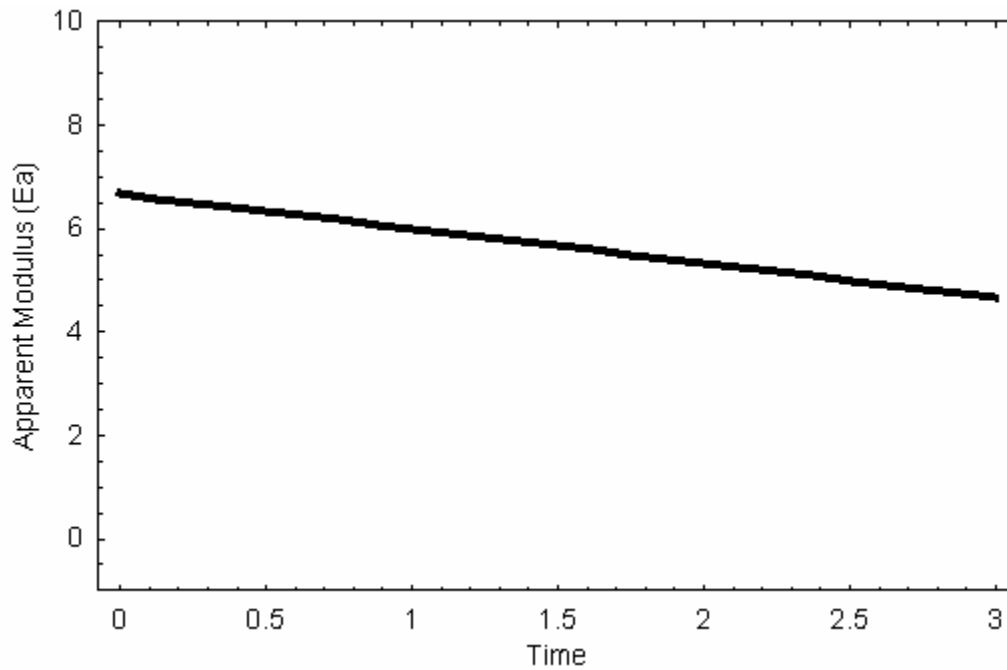


Figure 2.25. A plot of the Young's Modulus as a function of time is shown, for the case of plastic cell collapse failure mode.

According to the above equation, the elastic buckling case should register a step discontinuity in the modulus during deformation, while the plastic collapse case should see a gradual decrease in modulus. A closer look into the two failure modes must be taken to explore why the lower density suffers from elastic buckling and the higher density foams exhibit the plastic collapse.

The following section relies on the model development in the book on cellular solids by Gibson and Ashby and uses extensively the results from this book (1980). For the case of elastic buckling, the critical force needed to buckle the cell is presented in Eq. (2.18), where n is the rotational stiffness of the node, E_s is the modulus of the solid from which the foam was made, I is the moment of inertia, $bT^3/12$, and h is the length of the cell wall. The critical elastic buckling force must equal the applied load, given in Eq. (2.19), the stress applied to the horizontal area of the top of the cell. Eqs. (2.18) and (2.19) may be set equal to each other, to calculate and the critical stress σ_{el} , shown in Eq. (2.20).

$$P_{crit} = \frac{n^2 \pi^2 E_s I}{h^2} \quad \text{Eq. (2.18)}$$

$$P = 2\sigma_2 lb \cos(\theta) \quad \text{Eq. (2.19)}$$

$$\frac{\sigma_{el}}{E_s} = \frac{n^2 \pi^2 T^3}{24 lh^2 \cos \theta} \quad \text{Eq. (2.20)}$$

Given the (known) parameters, Eq. (2.20) can be simplified to Eq. (2.21) (see below): the length and height of the cell for a regular hexagon are equal, the depth of the cell is 1, the internal angle is 30° , and n for a regular hexagon (Gibson, 1980) is equal to 0.69.

$$\frac{(\sigma_{el})}{E_s} = .22 \left(\frac{T}{l} \right) \quad \text{Eq. (2.21)}$$

The critical elastic buckling stress, σ_{el} , is left only in terms of only the thickness of the cell, the length of the cell wall, and the modulus of the material from which the foam was made. The case of plastic collapse invokes the principle of virtual work. Consider the hexagonal cell again, illustrated in Fig. 2.26.

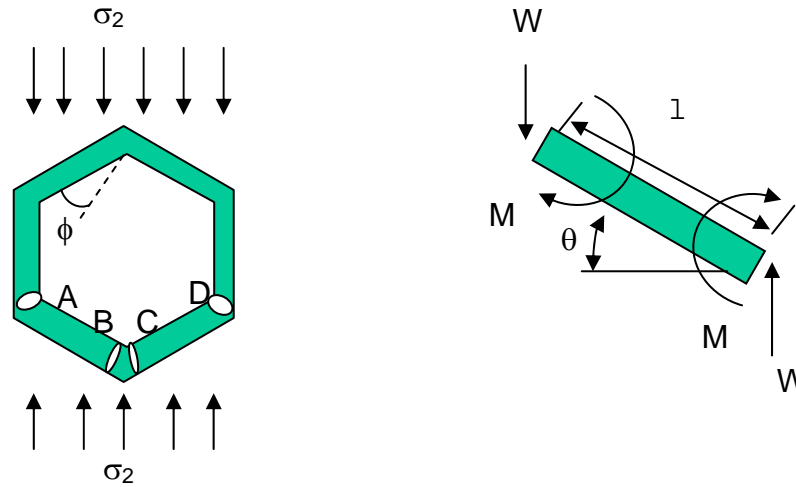


Figure 2.26. (a) A diagram of the 2D hexagonal cell indicating the 4 hinges A B C and D, and the rotation angle ϕ (b) A Free Body Diagram of a single side of the hexagon indicating the Work done, W , the moment at the hinge, M , the interior angle of the cell, θ , and the length of the cell wall, l .

The force applied, P , multiplied by the distance traveled, d , must be equal to the moment at the 4 hinges multiplied by the rotation of the arms, ϕ , as shown in Equation 2.22. Where P is given as the stress applied, σ_2 , multiplied by the area of the top face $2l\cos(\theta)$, as seen in equation 2.23, and d is given by the rotation angle of the side multiplied by the length of the side and the interior angle of the cell, θ , given in equation 2.24.

$$Pd=4M_p\phi \quad \text{Eq. (2.22)}$$

$$P=2\sigma_2l\cos(\theta) \quad \text{Eq. (2.23)}$$

$$d=\phi l\cos(\theta) \quad \text{Eq. (2.24)}$$

Inserting the values of P and d , given in Eqs. (2.23) and (2.24) into (2.22), the moment, M_p , at the hinge can be expressed as:

$$M_p = .5\sigma_2 l^2 \cos^2(\theta) b. \quad \text{Eq. (2.25)}$$

The moment at the hinge, M_p , can also be written as

$$M_p = \left(\frac{1}{4}\right) \sigma_{ys} b T \quad \text{Eq. (2.26)}$$

where σ_{ys} is the yield stress of the solid from which the foam was made, b is the depth of the cell and t is the thickness of the wall.

Equating these two expressions for the moment, M_p , given in Eqs. (2.25) and (2.26), a relation is formed between the applied stress, σ_2^* , and the thickness of the cell wall, length of the cell wall, interior angle, θ , and yield stress of the solid, as seen in Eq. (2.27) below. Given that this is a perfect hexagonal cell, θ can be assumed to be 30° and the expression reduces to Eq. (2.28), where σ_2^* is actually the critical plastic collapse load σ_{pl} .

$$\frac{\sigma_2^*}{\sigma_{ys}} = \left(\frac{T}{l}\right)^2 \frac{1}{2 \cos^2(\theta)} \quad \text{Eq. (2.27)}$$

$$\frac{(\sigma_{pl})}{\sigma_{ys}} = \frac{2}{3} \left(\frac{T}{l}\right)^2 \quad \text{Eq. (2.28)}$$

A relation can now be formed by setting the critical elastic stress, σ_{el} , to the critical plastic stress, σ_{pl} , (Eq. (2.29)) to develop a geometrical criterion by which to judge whether or not the foams will behave in an elastic buckling or plastic collapse mode.

$$\sigma_{el} = \sigma_{pl} \quad \text{Eq. (2.29)}$$

$$\left(\frac{T}{l}\right)_{crit} = 3 \frac{\sigma_{ys}}{E_s} \quad \text{Eq. (2.30)}$$

The material from which the foam is made is PVC, which has a Young's Modulus, E_s , of 2.4 GPa and a yield strength, σ_{ys} , of 40 MPa and the average cell wall length of the 300 μm . Using these values in Eq. 2.30, the critical wall thickness was determined to be 15 μm . From SEM images taken of the various cell samples, the cell wall thickness does range between 10-15 μm for lower density foams, while the denser foams have a larger cell wall thickness, on the order of 100 μm .

While this was an encouraging first step to understanding cell failure, the desire arose to observe the cells as they collapse to further support the elastic buckling versus plastic collapse theory. Figure (2.27a) shows the 2-D undeformed cell configuration, while Fig. (2.27b) illustrates the hypothesized state of the cells after elastic buckling has occurred and Fig. (2.27c) shows the hypothesized cell after they have experienced plastic collapse. If these cell phenomena are observed in the deformation of the foams studied, it would give one more indication that these are the true deformation behavior of these materials. To optically observe the in-situ deformation of the cell walls, a digital image correlation technique was developed and used in conjunction with the ultrasonic materials testing system and compression tests.

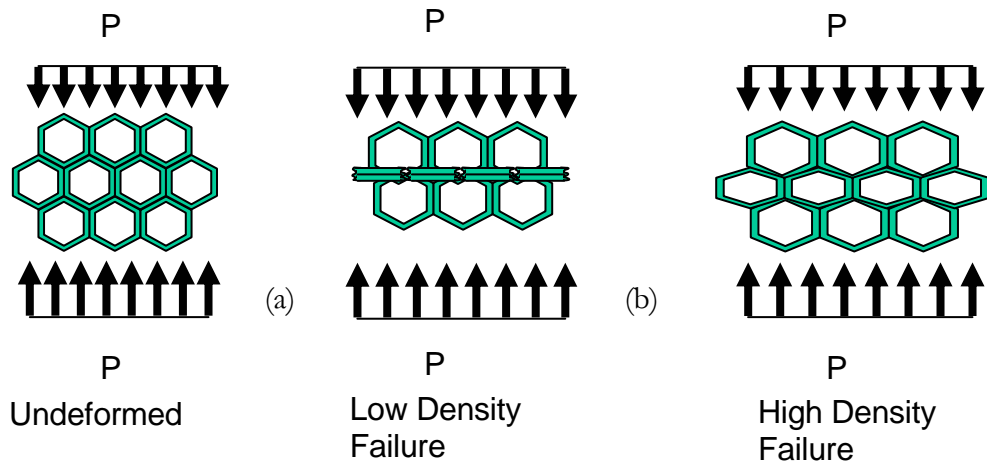


Figure 2.27. (a) Diagram of 2D hexagonal cells in the undeformed configuration (b) Diagram of 2D hexagonal cells in the elastic buckling configuration (c) Diagram of 2D hexagonal cells in the plastic collapse configuration Spatial Magnitudes

2.8 Digital Image Correlation

Digital image correlation (Sutton, 1983) is an optical technique that can determine the displacement of the surface of a sample by correlating an image of the surface before the deformation and an image of the surface after deformation. DIC is a widely-used technique in experimental mechanics ranging from macro to nano-scale applications (Abanto-Bueno 2002, Peters 1982, Peters 1983, Sutton 1983). Wang and Cuitino have used a digital image correlation technique to analyze the compression deformation behavior of open cell polymeric foams. The natural random surfaces pattern on the sample and the non-invasive nature of this technique made it an optimal method for the investigation of deformation mechanisms in cellular solids.

A digital image correlation setup is relatively simple and only requires a camera, light, data acquisition card, acquisition software and a computer. The camera is located outside the immediate test area so as to not interfere with the compression or ultrasonic testing system and can be used in conjunction with these two systems. A schematic of the DIC experimental set up is presented in Fig. (2.28).

A one megapixel, Uniq model# 1030 (Santa Clara, CA) CCD camera was used in conjunction with a 50 mm Nikon zoom lens. A fiber optic ring light mounted onto the end of the lens illuminated the sample. A Bitflow Roadrunner 24 card (Woburn, MA), gathered the data that was recorded by Streams 5, an image capturing software developed by I.O. Industries (London, Ontario, Canada), at a rate of 2 frames per second. The image gathering was initiated at the same time as the compression, so the images could be correlated to the displacement of the MTS machine, as well as the ultrasonic data gathered. The final experiment conducted first compressed the sample, while ultrasonic measurements were being made and images of the sample were being recorded.

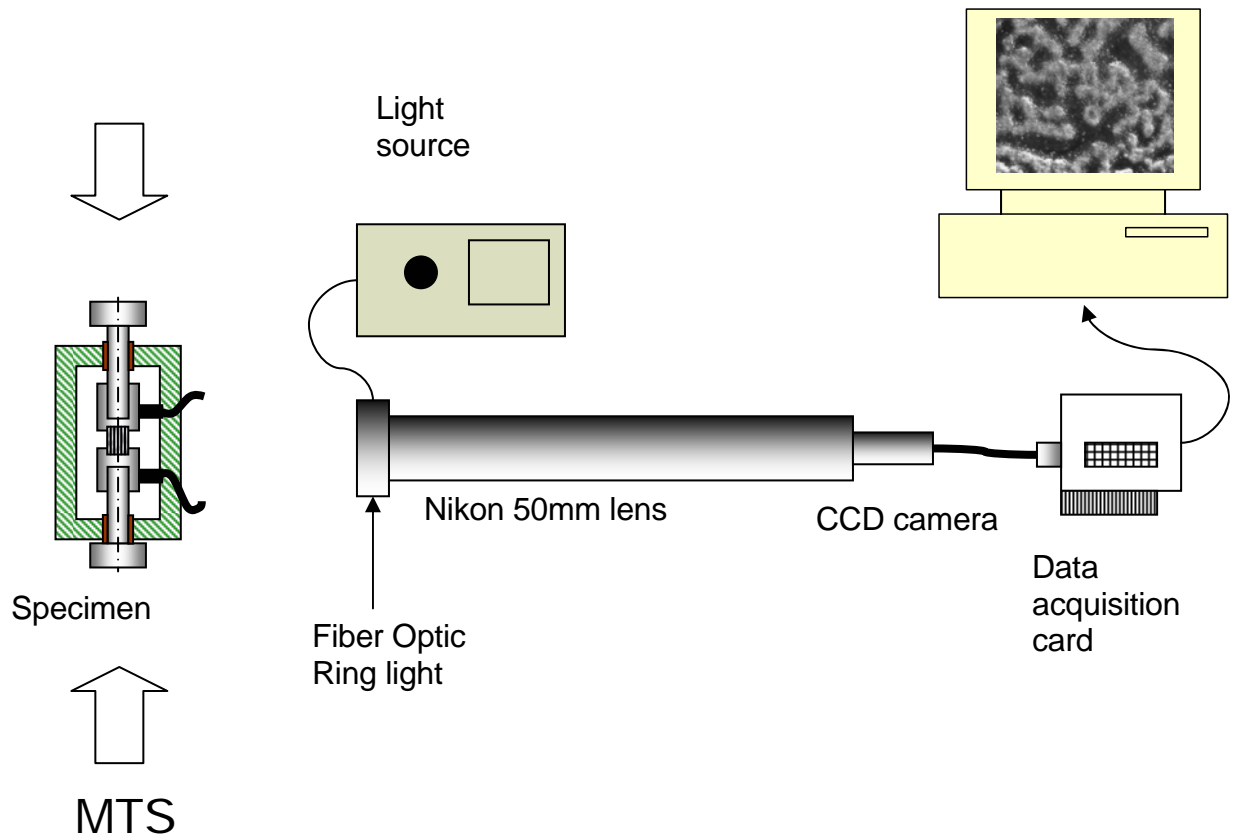


Figure 2.28. Experimental set up for the Digital Image Correlation (DIC) measurements.

2.8.1 Digital Image Correlation Algorithm

Digital image correlation algorithms all depend on some type of correlation function, which is minimized as two images become identical. There are many ways of calculating a correlation function. To discuss the method of calculation used in this study, representative undeformed and deformed images are defined in Fig. (2.29).

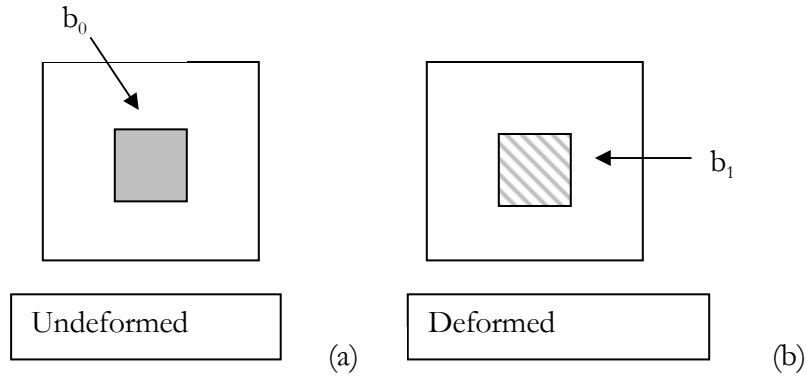


Figure 2.29. (a) Schematic of undeformed image area with undeformed subset indicated (b) deformed image area with deformed subset indicated

Ideally, each point in the undeformed image would be matched to a point in the deformed image. The matching would be carried out by assigning some parameter (gray scale, color, intensity) to the point itself, and finding a point with that same parameter in the deformed image. However, when dealing with multiple points, a single value is not a unique signature of a point. A subset of neighboring points is used to give a unique signature to a point. The size of the subset is determined by the size of the area where the picture is assumed to undergo homogeneous deformation. A deeper study of proper subset selection and definition is covered by Sutton *et al* (1983).

The 2-D correlation function used in this study is

$$C(u, v) = \int b_0(x, y)b_1(x + u, y + v)dxdy \quad \text{Eq. (2.31)}$$

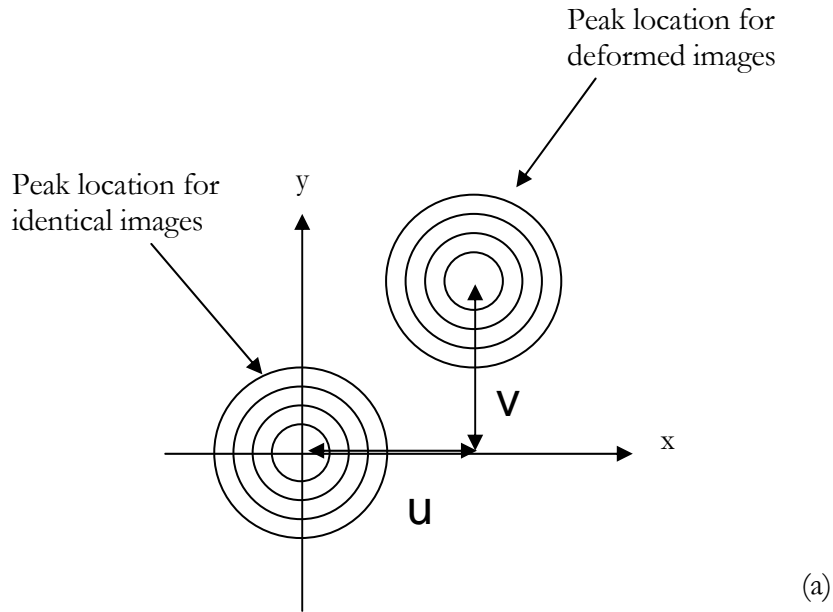
where b_0 is the subset in the undeformed image, b_1 is the subset in the deformed image, x and y are the Cartesian coordinates of the reference point in the undeformed configuration, u and v are the horizontal and vertical displacement between the undeformed and the deformed image respectively.

The software program *Matlab* (MathWorks, Natick, Massachusetts) was used to calculate deformation and of the two imported images by taking the conjugate Fourier

transform of the undeformed image and multiplying it by the Fourier transform of the deformed image:

$$C(u, v) = F^{-1}(F(b_0) * F(b_1)) \quad \text{Eq. (2.32)}$$

The inverse Fourier transform of the product is then taken to calculate the correlation function. If the correlation function is plotted on the x-y plane, it will appear as concentric circles, as sketched in Fig. (2.30a). If the correlations function, of a low noise system is plotted against x or y it will be delta function, as sketched in Fig. (2.30b). If noise is present, the correlation function will have a wider peak. If the two images match perfectly, the peak will be located at the origin, as seen in Fig. (2.30a). If the two images have undergone deformation relative to each other, the peak will be off-center. The distance of the peak from the center determines the amount of deformation between the two images.



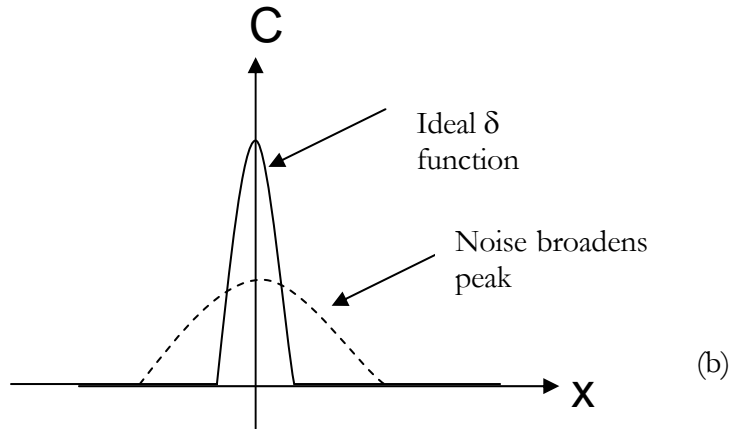


Figure 2.30. (a) Plot of peak location on x-y plane with displacement indicated by u and v
 (b) Plot of correlation function as a function of x position, showing the ideal δ function peak in the case of little noise and the broader peak generated by correlation of noisy data

The displacement is calculated for a specified number of points in an image. The displacement could be calculated at each point in the image, but that would be computationally intensive and expensive. The processing of the entire image is performed in *Matlab* by a user-defined function. The function is given four arguments and returns three values. The first two arguments are the undeformed and the deformed images. The third argument, w , is the length of the side of the subset in pixels. The displacement components are determined only for the center point of this area. The last argument, d , is the distance in pixels between the points where the deformation (displacement) is measured. The *Matlab* program increments through the entire images and records the u and v displacement at each designated data point, along with the value of the correlation function at that point.

The following example seeks to clarify how the input parameters are defined for a typical digital image. The Uniq, UP1030 camera has a $\frac{1}{2}$ " CCD sensor with 1030x1030 pixels on each side of the CCD. The field of view of in the experiment was 13X13 mm which gave an optical resolution of 12 μm /pixel. The subset is defined as a region of which experiences uniform deformation. The displacement is calculated for each subset region.

The subset size chosen to accurately calculate displacement while minimizing computational time was chosen to be, $w = 100$ pixels, as seen in Figure 2.31a. The distance between subsets was taken as, $d = 50$ pixels, as shown in Figure (2.31b). (The displacement at each pixel could be evaluated by setting $d=1$; however, this would be computationally expensive, so a larger value of d is chosen to fully characterize the surface, without overburdened computation.) Under these conditions, a matrix of 21×21 data points will be evaluated by the program. However, as information about the sides to calculate the displacement is insufficient, only 20×20 usable data points will be generated, as depicted in Figure 2.31c.

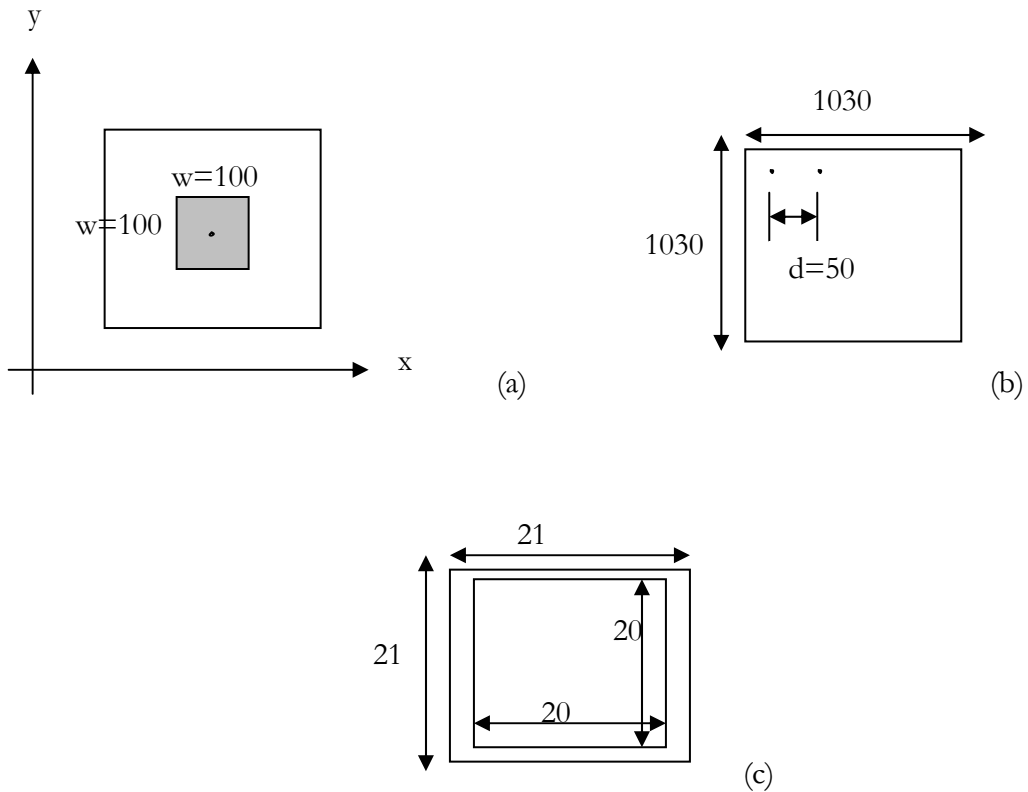


Figure 2.31. (a) Schematic of subset in image area with subset length and width indicated in pixels (b) pixel dimensions of image area given along with interval between image subsets (c) number of subsets in image plane along length and width indicated useable area of image indicated by smaller box.

2.9 DIC Results

The images captured using the CCD during the deformation of foams were analyzed using a DIC code developed *in-house* by Soonsung Hong (2006). The results of the experiment on the H130 foam can be seen in Figs. (2.32abcd). Figure (2.32a) shows the foam at the beginning of the test or in an undeformed state. A grid that tracks the displacement of the material is superimposed during post processing to ease the visualization of the deformation. Figure (2.32b) shows the foam at 20% strain, Figure (2.32c) at 40% strain and (2.32d) at 50 % strain; non-uniform displacement has taken place, visualized by the superimposed collapse of some box in the grid. These results correspond to the model's prediction, that the lower density foam would have a non-uniform buckling behavior in some cells (localization), while others remained elastic, as seen in Fig. (2.32b,c,d). More specifically, Figure (2.32b) corresponds to the initial localization of deformation, due to elastic buckling, Figure (2.32c) shows propagation of the deformation throughout the sample, and Figure (2.32d) shows the almost completely collapsed cells, which signify the initiation of densification.

Figure (2.33) reveals the deformation behavior of the H250 high density foam. Figures 2.33a-d were taken at 0%, 15%, 30%, and 40% respectively. As the plastic collapse theory predicts, all the grids deform uniformly without the discontinuous grid collapse experienced in the H130 results. Once again, the grids are generated with the displacement vectors of the digital image correlation analysis. The lower edge of grids on Figure 2.33b seem to be completely collapsed, but this grid behavior is due to the fact that the numerical analysis encounters greater error at the edge of an image and has difficulty correlating. So, the bottom row of grids can be ignored, since they do not accurately reflect the deformation in the material.

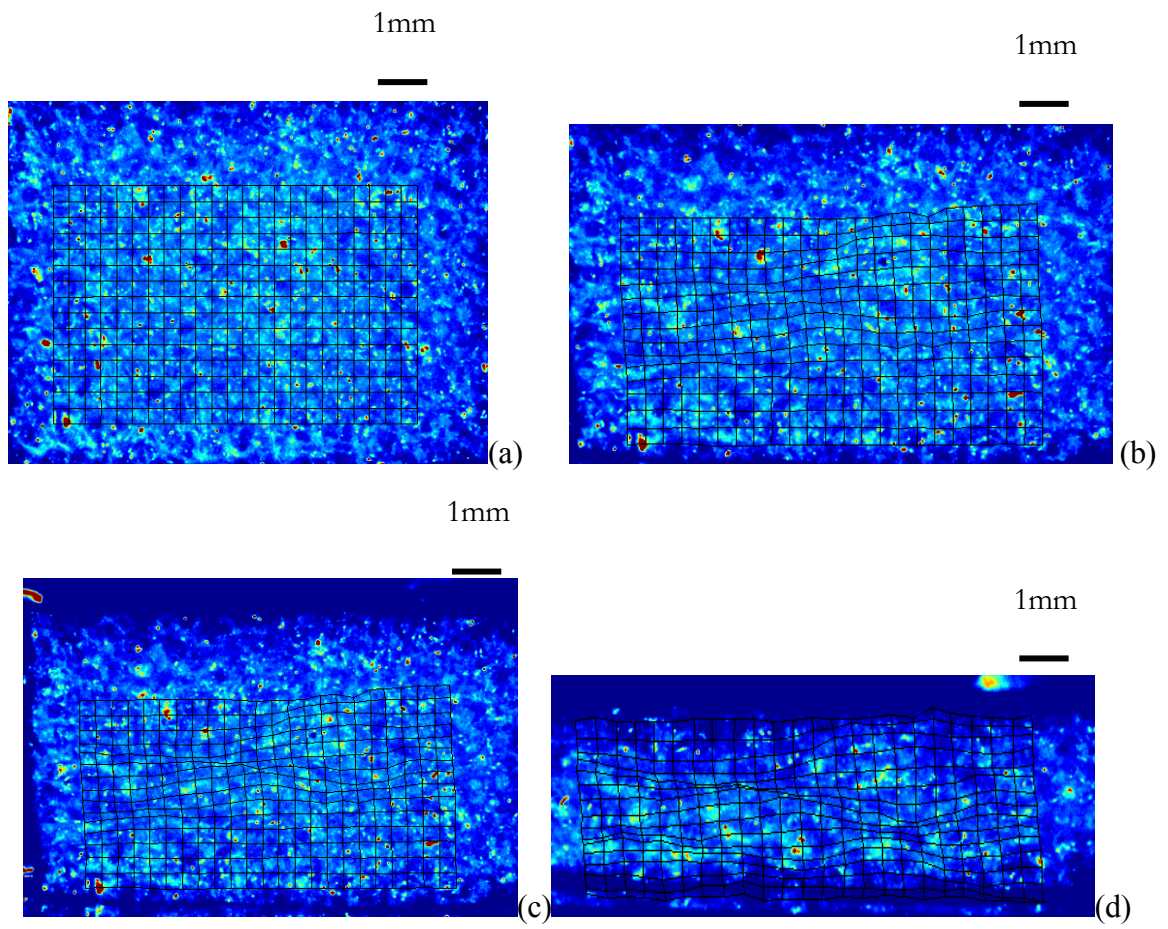


Figure 2.32: Visualization of cell buckling in Foam 130 kg/m^3 at various stages of deformation a) 0 % strain (b) 15% strain (c) 30% strain (d) 40% strain

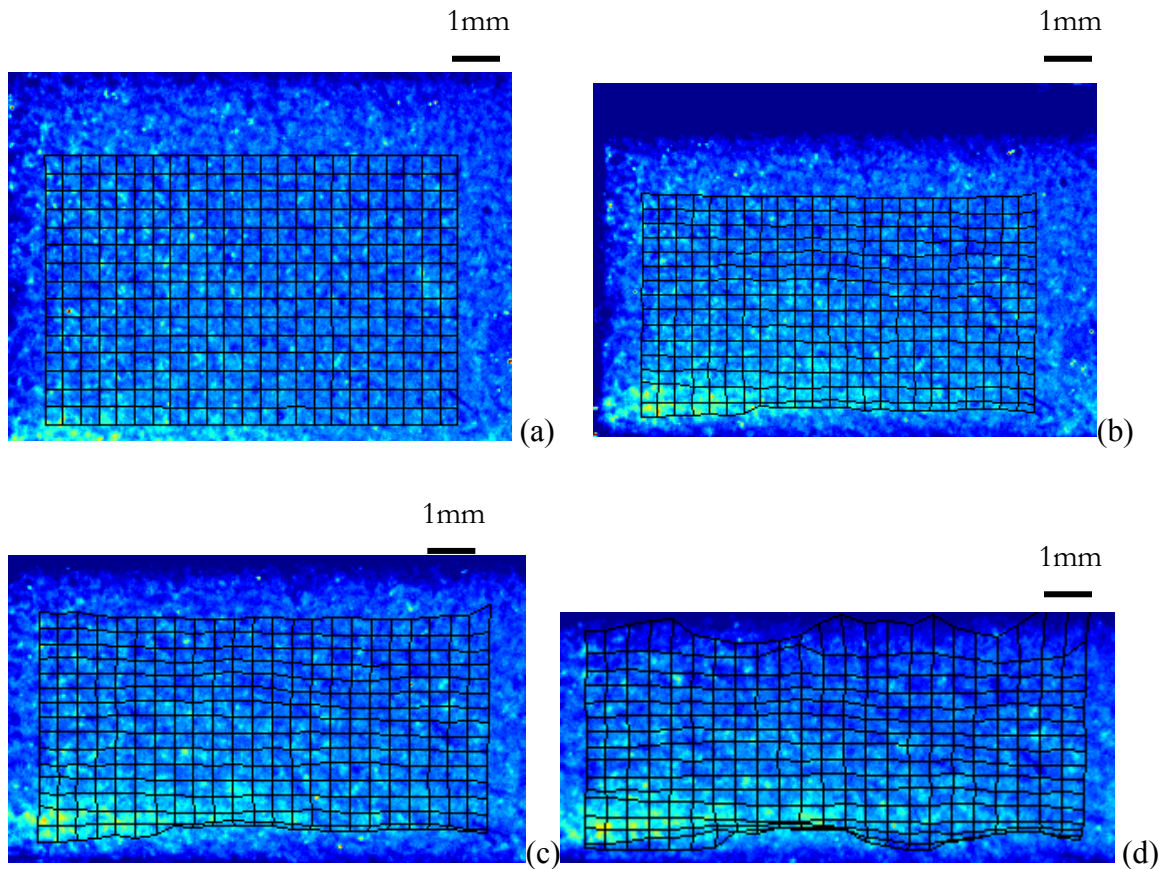


Figure 2.33: Visualization of plastic collapse in Foam 250 kg/m³ at various stages of deformation (a) 0 % strain (b) 15% strain (c) 30% strain (d) 40% strain

Numerous tests were performed on the H130, H160, H200 and H250. For brevity, only the results of H130 and H250 are given. The two lower density foams exhibited the same type of non-uniform collapse, while the two higher density foams displayed a more uniform plastic collapse type deformation. These results provide further evidence that the models of cell deformation for low and high density foams are justified.

2.10 Summary

The failure behavior of polymeric foam materials was investigated using several experimental methods. A novel method was developed to measure simultaneously both the longitudinal and shear wave speeds in a material under uniaxial compression, using a single

set of shear transducers. Experiments were conducted on polycarbonate, aluminum, copper and steel, which demonstrated the accuracy of the new method. The apparent modulus of Polymeric foam samples were placed in the new ultrasonic setup and modulus was tracked during deformation. Further investigation of these materials and their deformation behavior was conducted using a digital image correlation (DIC) technique.

The results of these tests revealed that the lower density materials behaved differently than the higher density materials. More specifically, the ultrasonically-measured apparent modulus of low density PVC foams (i.e. H130 and H160) showed a sharp drop in modulus during compression, while higher density foams (i.e. H200 and H250) showed no drop in modulus during deformation. To understand these results, two-dimensional hexagonal cells under compressive loading were studied. These studies showed that elastic buckling was a possible failure mechanism for lower density materials while plastic collapse was a probably method of defamation for higher density materials. Using established models (Gibson and Ashby (1980)), the critical wall thickness was calculated for the transition from elastic buckling to plastic collapse. This thickness roughly corresponded to the transition of wall thicknesses between the lower density and higher density foams studied. The samples were subjected to a compressive load while ultrasonic measurement and digital images were being taken of the material. The analyzed images revealed that the lower density foams indeed displayed the non uniform compression predicted by the elastic buckling theory of failure, while the higher density foams showed uniform cellular collapse corresponding to the plastic buckling mode.

There are several non-resolved issues in the calculation of modulus from the captured longitudinal and shear wave transit times. Particularly, the modulus was calculated using the equation for linearly elastic, isotropic materials. As stated in the introduction, foams are inherently anisotropic due to their manufacturing process. Additionally the wave must propagate through the cell walls, since the air inside the cell cannot transmit the longitudinal and shear waves. This means that the path traveled by the wave may be greater than the sample thickness. For these reasons, more work needs to be

done to understand how to relate the measured longitudinal and shear transit times to the Young's modulus and Poisson ratio of the sample.

Chapter III: Transverse Failure of Unidirectional Composites Under Wide Range of Confinement and Strain rates

3.1 Introduction

Widespread use of composite materials began in the 1960s in aerospace applications, but due to requirements for lightweight in aerospace applications and high manufacturing costs, composite structures have traditionally been “thin.” Research on these “thin” composite structures was limited to their in-plane behavior. With the development of new construction methods, such as resin transfer molding (RTM) (Rackers, 1998), thicker composites can be produced in an economically efficient manner, making composites usable in a wider range of applications including marine structures.

Marine structures are beginning to employ thicker composites, such as in sandwich structured hulls designed to replace current metal hulls in specialized applications. Hulls made with conventional materials, such as metal, withstand impact loads and provide stiffness to a structure, but increasing its stiffness requires increasing the thickness of the material, and raising the structural weight. Sandwich structures offer a lightweight alternative while still providing the desirable properties of structural stiffness found in traditional materials. These properties are achieved by the unique composition of sandwich structures, typically consisting of two thin faceplates bonded to a thick core material. The faceplates provide protection from foreign object damage to the structures, and are usually metallic or composite materials. The lightweight core consists of metallic or polymeric foams, polymer honeycomb or balsa wood, reduces the overall weight and increases the bending stiffness of the structure. The result is a material with high stiffness-to-density ratio, outperforming traditional counterparts. An important aspect of the sandwich structures is to withstand impact loading, which has not been explored in great detail. Other applications of thick composites include antenna housing decks and submarine sails.

The primary goals of this experimental characterization of thick composites were to determine effects of three-dimensional stress fields and high strain rates on the macroscopic

mechanical response, as well as micro-structural aspects of failure initiation and propagation under transverse loading. Transverse loading refers to loading that occurs in the fiber plane and perpendicular to the fiber axes. To cover the rates of strain from 10^{-3} to 10^4 s^{-1} , both servo hydraulic testing system and a Kolsky (split Hopkinson) pressure bar were used. The material characterized in this study is a composite typically used for the faceplates of sandwich structures, specifically an unidirectional fiber-reinforced S2-glass/8552 epoxy composite, with a fiber volume fraction of $V_f = 65\%$.

Low strain rate tests of S2-glass/epoxy composite were conducted over a wide range of confinements by using a newly developed experimental fixture, whereby the three principal stresses in a confined specimen can be measured independently. Similarly, high strain rate tests also applied a range of confinement on the specimen with a fixture that could measure the three principal stresses in the material.

The experimental results indicate that the mechanical response and the strength of the composite in the transverse direction are functions of strain rate and are principally governed by the properties of the matrix material. However, the effect of stress multiaxiality seems significantly more pronounced on the overall transverse response of composites. Post-test scanning electron microscopy used to identify the transverse failure mode suggests that under transverse loading, any confinement contributes to the homogenization of shear failure at low-strain rates, but fails to exhibit significant effects at high strain rates. It was also observed that macroscopically transverse failure is dominated by shear and occurs within localized bands through multiple fiber-matrix interface failures at the microscale. These shear-dominated failure bands are found to be inclined in a direction approximately 35 degrees to the fiber plane. Implications of this deviation in the orientation of failure bands from maximum shear trajectories at 45 degrees will be discussed with reference to confinement stress and strain rate.

3.2 Material

The material used in this study was a S2/8552 glass/epoxy fiber-reinforced composite (FRC). The material, produced by the School of Aerospace Engineering at Purdue University (courtesy of Professor C.T. Sun), has 0° degree fiber orientation with a nominal fiber volume of 65%. An SEM micrograph of a virgin specimen is shown in Fig. 3.1. The image depicts the face perpendicular to the fibers as indicated by the schematic. The fibers have a diameter of $7.5 \pm .01 \mu\text{m}$. The sample received had dimensions of $254 \times 355 \text{ mm}^2$ and an average thickness of 5.8 mm. Two types of specimens were machined for performing the experiments. The specimen dimensions for quasi-static tests, illustrated in Fig. 3.2, were typically around $9.51 \pm 0.05 \text{ mm}$ in both length and width and $5.02 \pm 0.05 \text{ mm}$ in height.

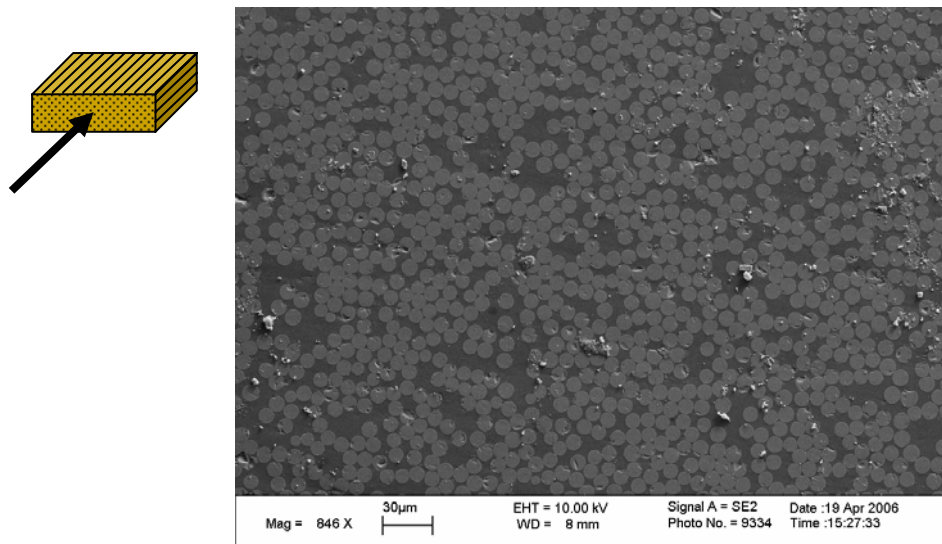


Figure 3.1. SEM micrograph of virgin specimen of S2/8552 glass/epoxy composite.

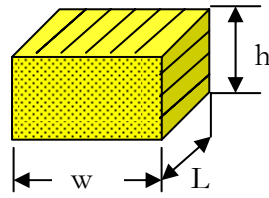


Figure 3.2. Schematic of specimen indicating its length width and height

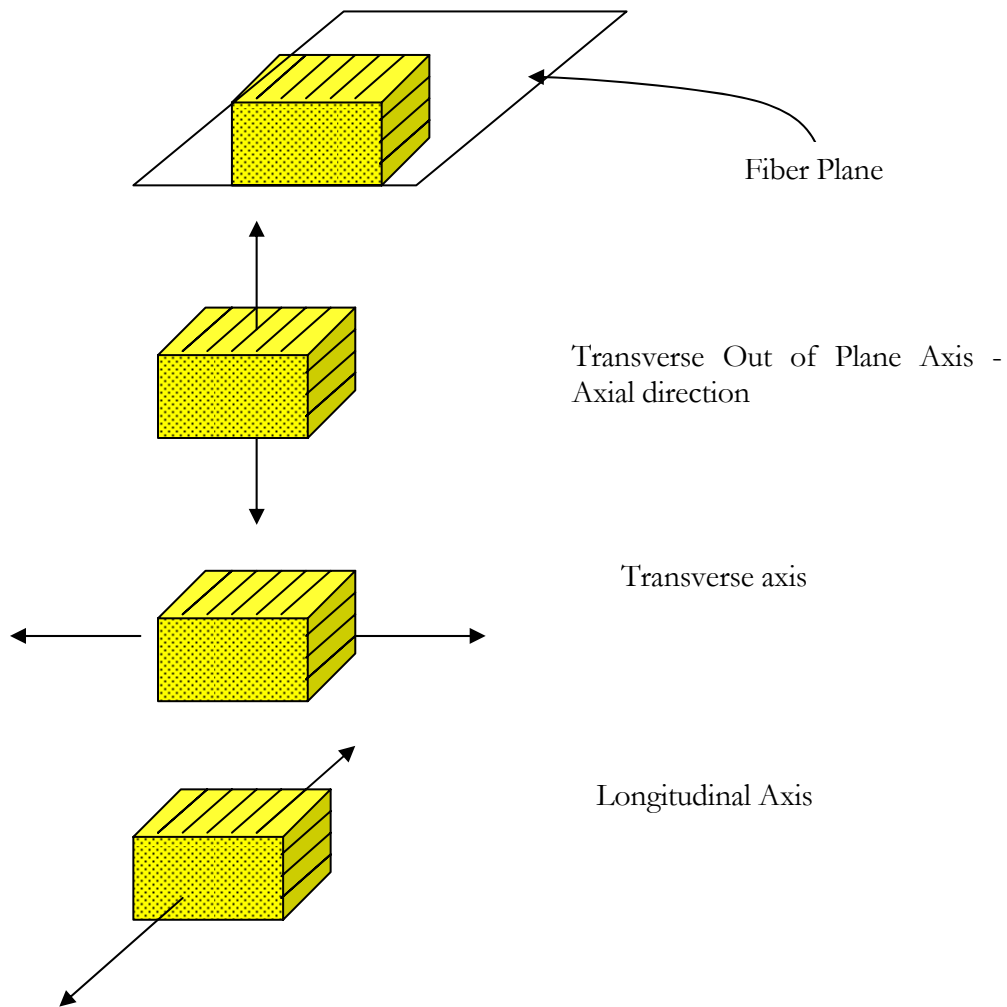


Figure 3.3. Schematic of unidirectional composite specimen with its axes defined (adapted from Daniel, 1994).

The samples were machined to have the fibers aligned along one axis of the specimen. The axis parallel with the fiber direction is defined the longitudinal axis, the axis orthogonal to the longitudinal axis and parallel with the fiber plane is defined as the transverse axis, and the axis orthogonal to the fiber plane is defined as the transverse out-of-plane axis or axial direction (Fig. 3.3).

The samples had to be prepared to the same specifications before they could be tested. The preparation process began with a large rectangular section being cut from the base material using a band saw, parallel to the fiber direction to ensure the fibers were aligned in the longitudinal direction. Then, all the edges were machined flat using a carbide end mill. Next, a slitting saw was used to cut the machined rectangle down to the final specimen size. Finally, the pieces were polished on all surfaces first using 320 grit and then 600 grit sand paper.

The specimens used in the high strain rate experiments were made by first cutting their rough shape with a band saw. They were then milled with a carbide end mill to square them, and finally, they were held in a precision vise, and ground on a surface grinder sprayed with water base synthetic coolant. The specimens used in the dynamic tests were smaller than the specimens used in the low strain rate tests, with a length and width of 6.00 ± 0.01 mm and a height of 4.00 ± 0.01 mm. These samples also had fibers running parallel to the length of the sample. All specimens were loaded perpendicular to the fiber plane.

3.3 Failure Models

Currently, design engineers predict failure in composite structures using numerous models including the Tsai-Wu (Tsai, 1971) model. The general approach, outlined by Christensen (Christensen, 2005), is to represent the failure in a polynomial expansion of the stress tensor.

$$F_i \sigma_i + F_{ij} \sigma_i \sigma_j + F_{ijk} \sigma_i \sigma_j \sigma_k + \dots = 1 \quad (3.1)$$

Einstein's tensorial notation is used to express the coefficients of the stress tensors. Voigt notation is used to represent the stress tensor as a vector. The first coefficient, F_i , is a second order tensor with 6 independent components. The second coefficient, F_{ij} , is a fourth order tensor with 21 independent components. The polynomial expansion is typically truncated after the second order terms, for practical reasons (a 6th order tensor has hundreds of components). The truncation leaves 27 independent parameters in the expression. Once plane stress conditions are assumed (making $\sigma_3=\sigma_4=\sigma_5=0$), the number of independent parameters reduces to 9.

$$f_1\sigma_1 + f_2\sigma_2 + f_6\sigma_6 + f_{11}\sigma_1^2 + f_{22}\sigma_2^2 + f_{66}\sigma_6^2 + 2f_{12}\sigma_1\sigma_2 + 2f_{16}\sigma_1\sigma_6 + 2f_{26}\sigma_2\sigma_6 = 1 \quad (3.2)$$

The linear σ_6 terms can be ignored because as Fig. 3.4 illustrates, the strength of the composite under pure shear loading along its principal material axes is independent of the sign of the shear stress.

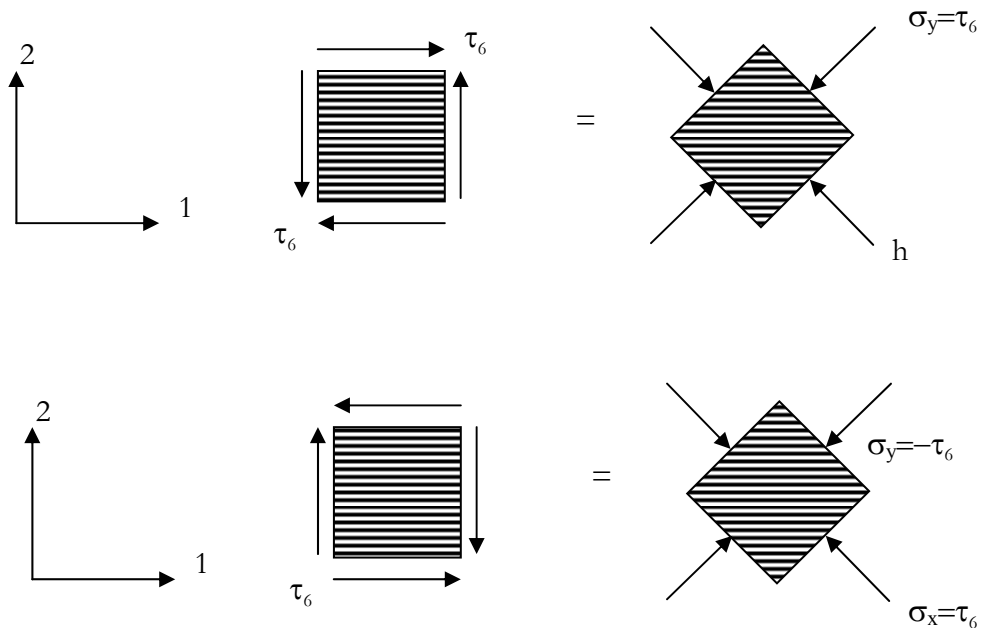


Figure 3.4. Positive and negative shear stress acting along principal material directions (adopted from Daniel, 1994)

These simplifications reduce Eq. (3.2) to,

$$f_1\sigma_1 + f_2\sigma_2 + f_{11}\sigma_1^2 + f_{22}\sigma_2^2 + 2f_{12}\sigma_1\sigma_2 = 1. \quad \text{Eq. (3.3)}$$

The remaining coefficients can be determined experimentally by performing simple uniaxial tension and compression experiments to find the strength of the lamina under these loadings. For example, consider uniaxial tension in the fiber direction, where σ_1 would equal T_{11} the longitudinal tensile strength of the composite and $\sigma_2 = \sigma_6 = 0$.

$$f_1T_{11} + f_{11}T_{11}^2 = 1 \quad \text{Eq. (3.4)}$$

Now, consider the case of uniaxial compression where σ_1 would equal C_{11} , the strength of the longitudinal compressive strength of the composite and $\sigma_2 = \sigma_6 = 0$.

$$f_1C_{11} + f_{11}C_{11}^2 = 1 \quad \text{Eq. (3.5)}$$

Solving these equations gives

$$f_1 = \left(\frac{1}{T_{11}} - \frac{1}{C_{11}} \right) \quad \text{Eq. (3.6)}$$

and

$$f_{11} = \left(\frac{1}{T_{11}C_{11}} \right). \quad \text{Eq. (3.7)}$$

If the process is repeated for uniaxial tension and compression in the transverse direction, then

$$f_2 = \left(\frac{1}{T_{22}} - \frac{1}{C_{22}} \right) \quad \text{Eq. (3.8)}$$

and

$$f_{22} = \left(\frac{1}{T_{22}C_{22}} \right). \quad \text{Eq. (3.9)}$$

If these values are then substituted back into Eq. (3.3),

$$\left(\frac{1}{T_{11}} - \frac{1}{C_{11}} \right) \sigma_1 + \left(\frac{1}{T_{22}} - \frac{1}{C_{22}} \right) \sigma_2 + \frac{\sigma_1^2}{T_{11}C_{11}} + \frac{\sigma_2^2}{T_{22}C_{22}} + 2f_{12}\sigma_1\sigma_2 + f_{66}\sigma_6^2 = 1 \quad \text{Eq. (3.10)}$$

The value of f_{12} , is difficult to obtain because it requires the biaxial tensile strength of the material; therefore, the following approximation is used instead:

$$f_{12} = -\frac{1}{2} \left(\frac{1}{T_{22}C_{22}T_{11}C_{11}} \right) \quad \text{Eq. (3.11)}$$

Table 3.1. Tensile and compressive strengths of S2/8552 composite in the fiber and transverse fiber directions.

T ₁₁ - Tensile Strength, Fiber Direction (MPa)	C ₁₁ -Compressive Strength, Fiber Direction (MPa)	T ₂₂ -Tensile Strength, Transverse Direction (MPa)	C ₂₂ -Compressive Strength, Transverse Direction (MPa)
1080	620	39	128

Using the values in Table 3.1 to compute the coefficients $f_1, f_2, f_{11}, f_{22}, f_{12}$ and substituting them into Eq. (3.3) the Tsai-Wu envelope can be plotted as shown in Fig. (3.5); the plot also has sketches of the loading modes at different points on the envelope.

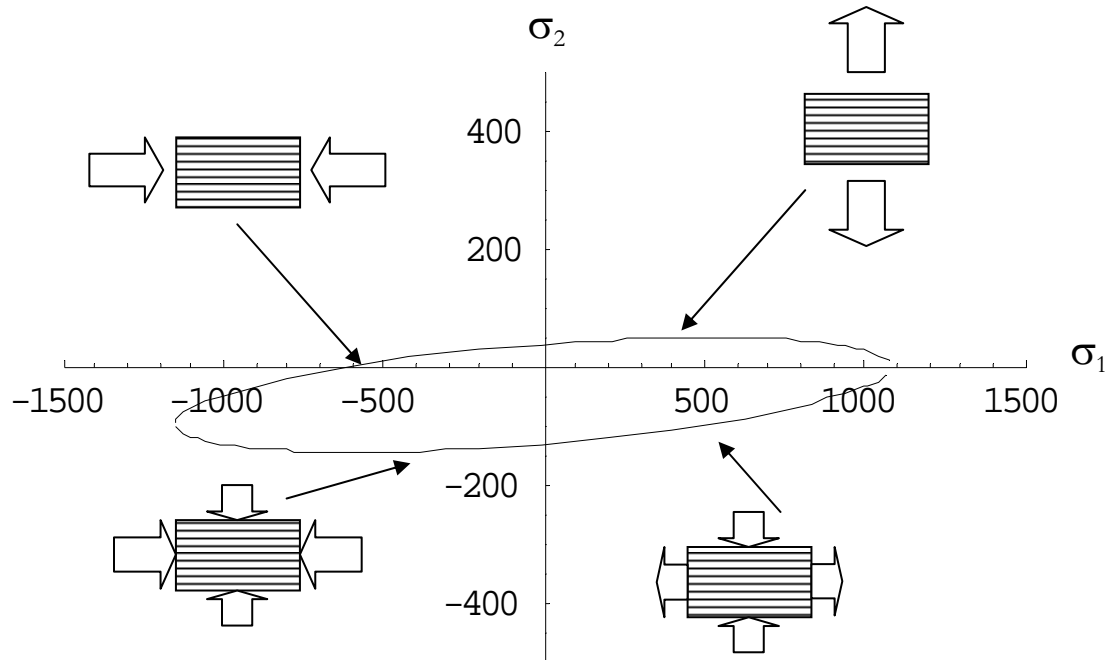


Figure 3.5. Tsai-Wu Failure Envelope for S2/8552 glass/epoxy composite.

While several models of composite failure exist, such as the Tsai-Wu, Hashin-Rotem and Christensen, their validity on the basis of experimental data must be examined. Considering Fig. 3.5, experimental data is readily gathered for the case of uniaxial tension and compression in both the fiber and transverse fiber direction. The regions of biaxial loading, however, are more difficult to explore experimentally. Two unique fixtures were developed to specifically explore the region of biaxial compression of the failure plane for quasi-static and dynamic loading. These fixtures can apply longitudinal and transverse confinement to a composite specimen. The fixtures are also able to record the stress in the longitudinal and transverse directions, i.e., σ_1 and σ_2 . The recorded data can then be plotted along side the Tsai-Wu failure model on the σ_1 and σ_2 plane, for comparison.

3.4 Low Strain Rate Experimental System

All low strain rate tests were performed on a Materials Testing System (MTS, model# 319.25). A compression fixture, shown in Fig. 3.6, was used for the quasi-static tests to ensure that the loading rods were well-aligned with one another, to minimize unwanted shear forces on the specimen. Molybdenum disulfide was also used on the contact surfaces to minimize friction on the specimen. Several strain rates were employed during the experiment. The strain rate was adjusted to between 10^{-4} to 10^{-1} s^{-1} by varying the displacement rate of the actuator. A cross head displacement transducer provided the uniaxial deformation data. These data were adjusted for machine compliance by running a test without any specimen present to determine the displacement as a function of applied load originating from the experimental set up. This correction was then subtracted from the recorded data to obtain the true deformation of the specimens.

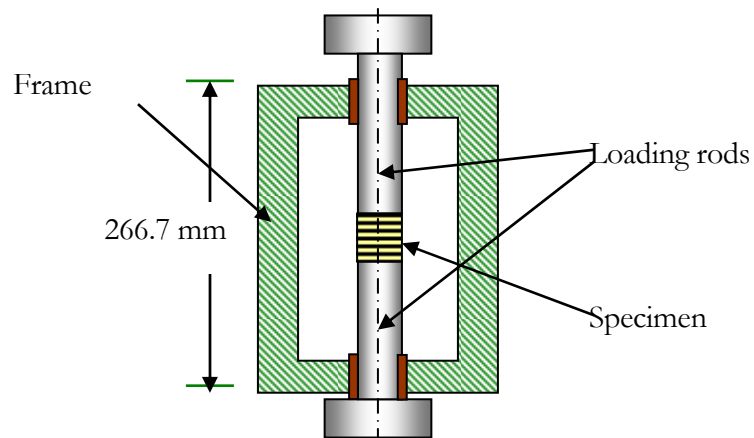


Figure 3.6. Schematic of the compression fixture used for quasi-static compression of confined and unconfined composite specimens.

3.5 High Strain Rate Experimental System

Dynamic loads were applied to the samples using the Kolsky (split Hopkinson) Pressure bar shown in Fig. 3.7. The Kolsky (1949) is bar based on one-dimensional wave

propagation and has been widely used to measure the dynamic compressive behavior of engineering materials. Two strain gauges are employed in this setup; the first measures the incident wave ($\epsilon_i(t)$), and the reflected wave ($\epsilon_r(t)$) at the center of the incident bar as shown in Fig. 3.7. The second measures the transmitted wave ($\epsilon_t(t)$) and is located at the center of the transmission bar. The Wheatstone bridge connects the strain gauges to a 4 channel digital storage oscilloscope (Nicolet, 440, LDS Test and Measurement, Charlotte, NC) with a 12 bit digitizer and 10 MHz sampling rate per channel. Assuming that the deformation in the specimen is homogeneous, the signals recorded by the strain gauges can be utilized to determine the average stress and strain in the specimen using the relations

$$\sigma(t) = \frac{AE}{A_s} \epsilon_r(t) \quad \text{Eq. (3.12)}$$

$$\epsilon(t) = -\frac{2C}{L_s} \int_0^t \epsilon_r(\tau) d\tau \quad \text{Eq. (3.13)}$$

where A , E , and C represent the cross-sectional area, Young's modulus, and the wave speed of the bar material, respectively. The variables L_s and A_s represent the specimen's length and cross-sectional area. Further details of this experimental method can be found in Gray³. The diameter of both the incident and reflected bars was 19.05 mm. The incident bar was 1215 mm in length, longer than the 1020 mm transmission bar, thus enabling specimen recovery. The striker bar had a diameter of 19.05 mm and a length of 152 mm. All rods, i.e. the striker, incident, and transmission bars were made of precision ground high strength C350 maraging steel.

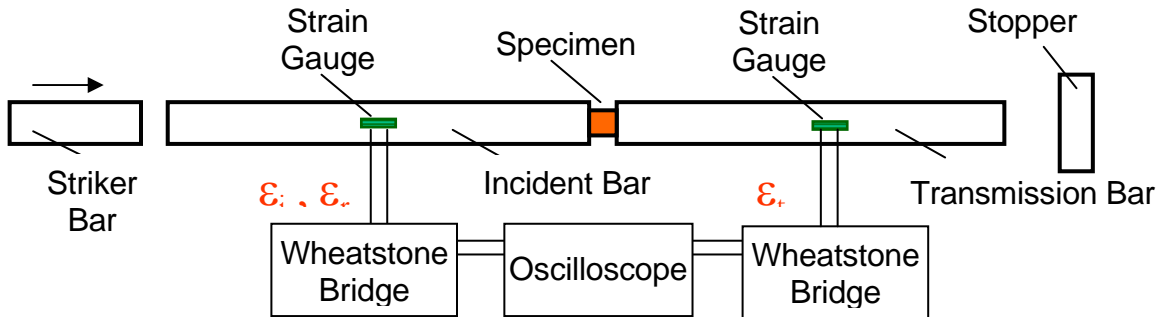


Figure 3.7. Schematic of Kolsky (split Hopkinson) bar setup for high-strain-rate testing of materials.

3.6 Confinement

Two fixtures were each designed to independently apply and measure confinement in the longitudinal and transverse fiber direction. One fixture was designed for use with the quasi-static loading system (MTS) and a second in the dynamic loading setup. The stress in the fiber direction, also known as the longitudinal direction, is labeled, σ_1 , in Fig. 3.8. The stress perpendicular to the fiber stress but still in the fiber plane, also called the transverse fiber stress is labeled, σ_2 , in Fig. 3.8. The axis coincident to the loading apparatus axis, also known as the axial stress is labeled σ_3 in the figure below. It is important to note that the composite material tested was constructed by layering several sheets of “prepreg” material. Prepreg, which stands for preimpregnated, is a sheet of epoxy which contains a single layer of fiber materials. The prepregs are layered on top of one another and then cured under pressure until the sheets merge into a single structure. Therefore, the axial load will be applied perpendicular to the inter-laminar interface plane.

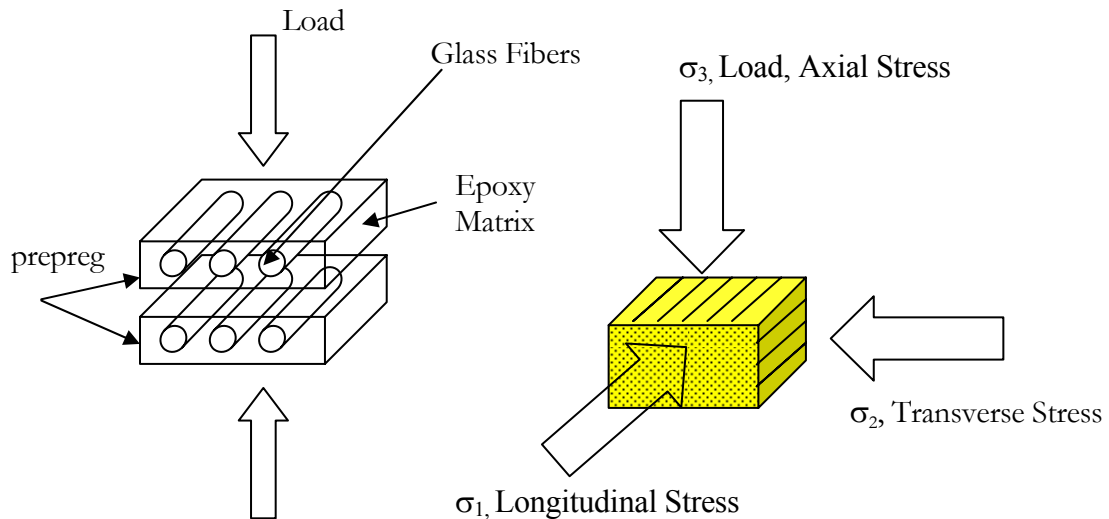


Figure 3.8. Schematic of the layered structure of the specimen and stress axis definition

3.6.1 Low strain rate confinement method

The fixture for the low strain rate tests had three major requirements to fulfill: first, to apply confinement in the longitudinal and transverse fiber directions, second, to measure the confinement on the specimen, and finally, to vary the confinement in each direction.

As stated in the previous section, the two out-of-plane transverse faces are those loaded directly by the MTS machine. To load the other four faces individually, a square frame with four metal “fingers” in a cross configuration was developed. Each rectangular “finger” had one end flush with the specimen. The other end fit into one of four rectangular slots cut into the square frame at 90 degrees to each other. The longitudinally aligned fingers were larger at one end to keep the transverse fingers aligned. The fingers prevented the specimen from elongating in the longitudinal and transverse directions, as it would normally, were the fingers absent. When the specimen is compressed in the axial direction, the fingers of the fixture effectively “confine” the specimen in the longitudinal and transverse fiber direction.

Two 350-ohm strain gauges made by Vishay Micro Measurement Groups provided the data to calculate the value of the confinement. One gauge was placed on the longitudinally aligned finger; the other on the transversely aligned finger. Both were located at the exact middle of the finger, equidistant from both ends and both sides.

Figure 3.9(a) shows a photograph of the fixture, with the axial (σ_3), longitudinal (σ_1), and transverse (σ_2), stress axes labeled. An illustration of the top of the fixture is shown in Fig. 3.9(b), and also indicates the location of the strain gauges, marked, SG-1 and SG-2 for the longitudinal and transverse measurement strain gauges, respectively.

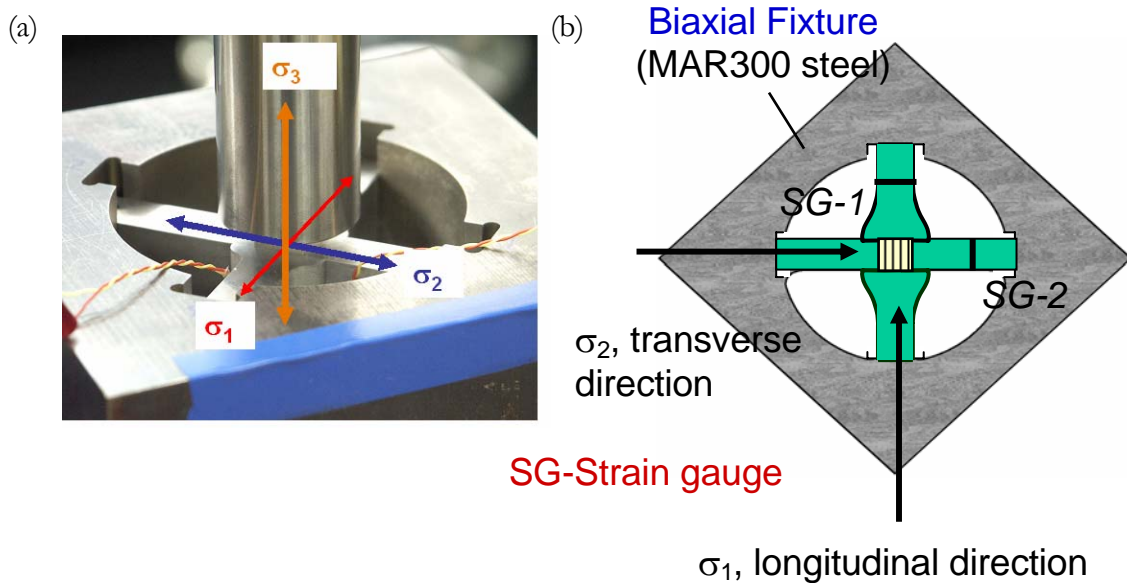


Figure 3.9. (a) Photograph of the quasi-static confinement fixture; (b) Schematic of the top view of the confinement fixture used for the quasi static test to introduce lateral confinement.

The confinement of the specimen is dependent on the material of the fingers used. A cross section of the fixture is provided in Fig. 3.10 as an example. While applying a load in the axial direction (σ_3), the specimen will exert a force (σ_2) on the fingers. The deflection in the finger will vary, depending on its Young's Modulus. Varying the material from which the finger is made varies the extent to which the specimen is allowed to expand, thus effectively varying the confinement on the material. For example, a steel finger would provide a large amount of confinement, while an aluminum finger would provide a lesser amount of confinement. The experimental set up utilized various fingers made from polycarbonate, aluminum, copper, steel, and a combination of aluminum fingers and polycarbonate pads, which will be discussed in the next section.

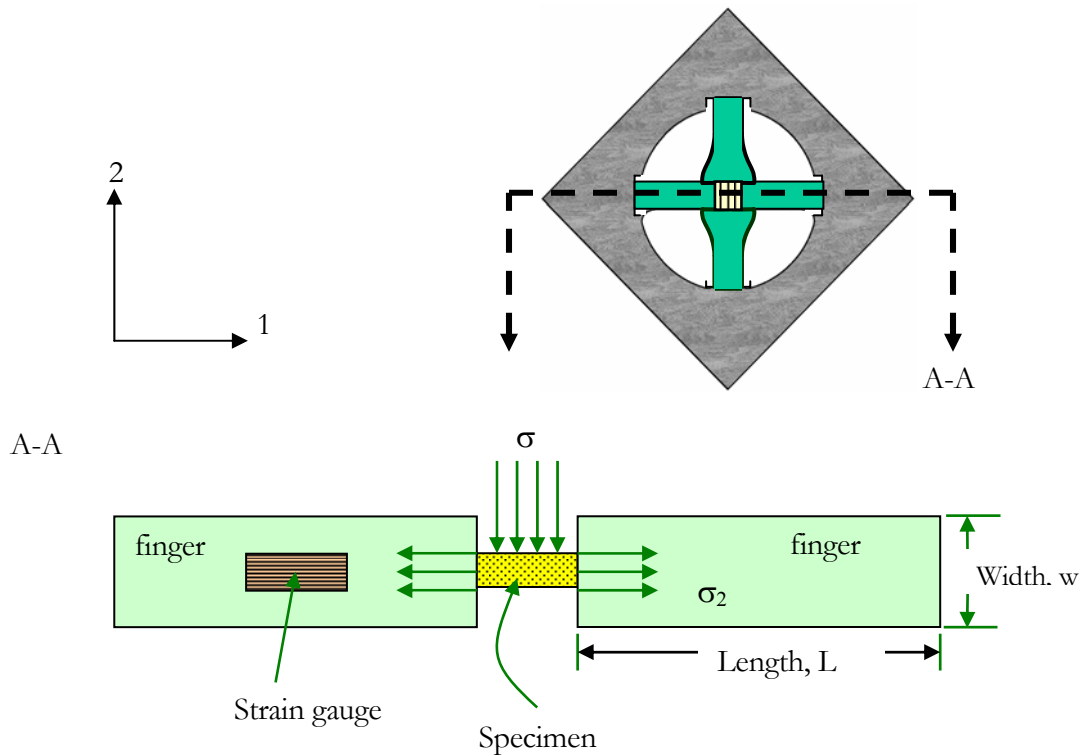


Figure 3.10. Cross section of the confinement setup, showing the transversely aligned fingers and the specimen.

The biaxial frame attaches to the loading frame by resting on the lower holder that fits over the bottom loading rod, as depicted in Fig. 3.11. Figure 3.11(a) provides a perspective view of the entire loading assembly, including the biaxial confinement frame. Figures 11(b) and 11(c) provide a cross-section of the assembly and a magnified view of the holders and fixtures, respectively. The diagram shows both the upper and lower fixture that have a 1" diameter hole, which keeps the axis of the fixture and the frame in alignment. The confining fingers rest on an upper holder that sits on the lower holder. The confining fingers are not attached to the biaxial fixture.

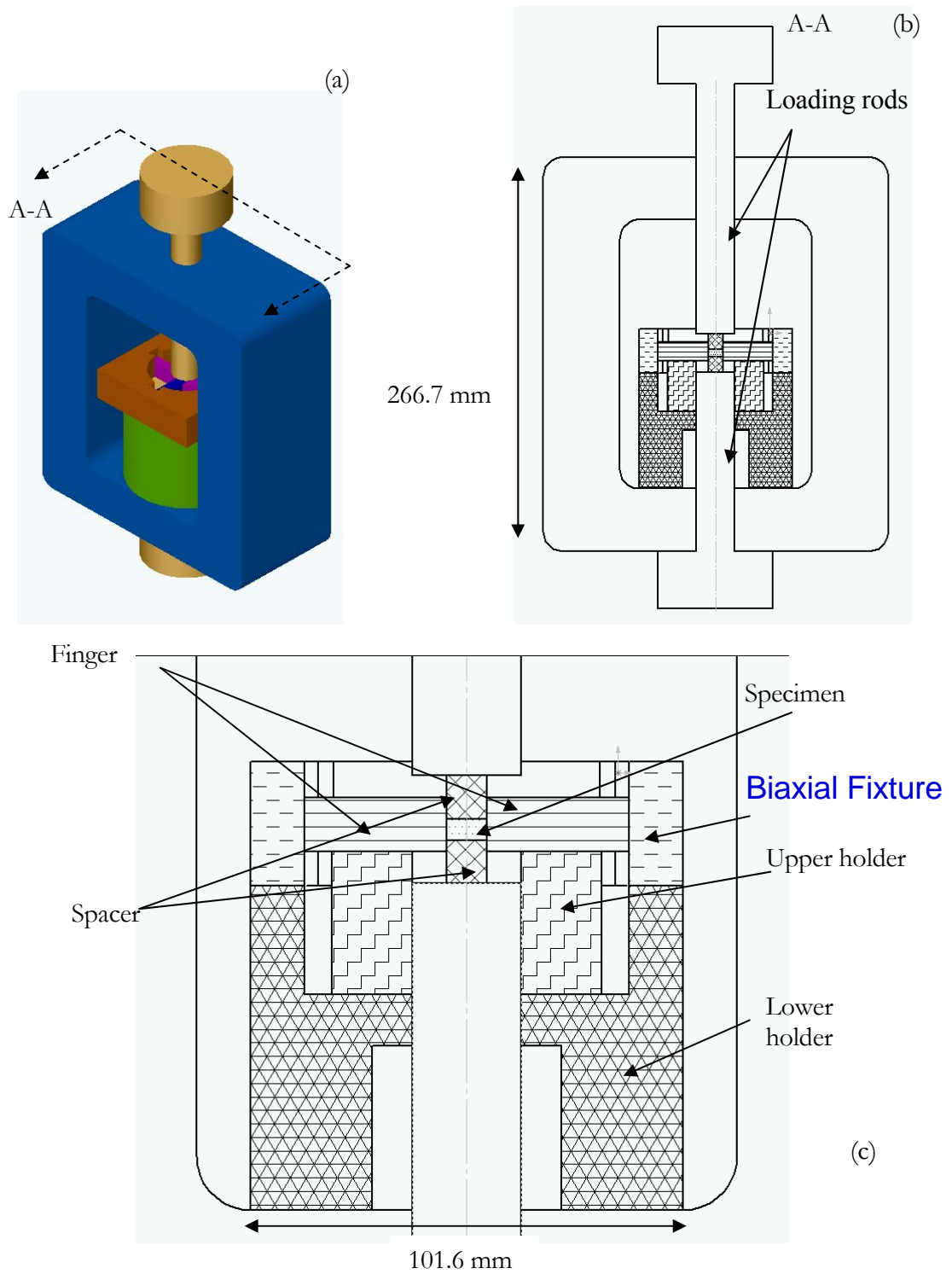


Figure 3.11. (a) Perspective view of the testing assembly; (b) section view of the testing assembly; (c) magnified view of testing assembly.

The length, width, and height of the finger were $33.35 \pm .001\text{mm}$, $9.35 \pm .01\text{mm}$, and $14.14 \pm .01\text{mm}$, respectively. The specimens' nominal height of 5 mm and the fingers' nominal height of 14 mm made the specimen thinner than the finger, creating a well configuration. Therefore, a maraging steel loading platen was employed to transfer the load from the loading rods depicted in Figure 3.11, to the specimen. Figure 3.12(a) shows the fixture and specimen without the maraging steel adapter and Fig. 3.12(b) shows the fixture with the adapter. The maraging steel adapter platen had a length and width of $9.35 \pm .01\text{mm}$ and a height of $10.40 \pm .01\text{mm}$.

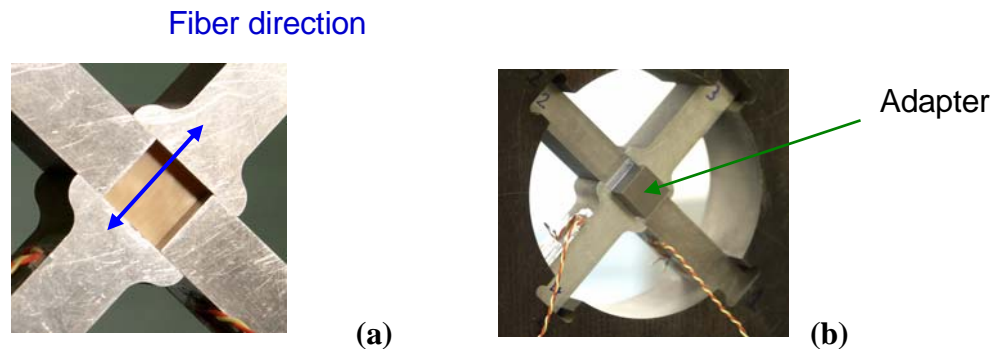


Figure 3.12. Photographs of the confinement fixture, (a) without maraging steel adapter, (b) with maraging steel adapter.

3.6.1.1 Varying Confinement with Polycarbonate Pads Inserts

In order to test confinements smaller than those provided by aluminum but greater than polycarbonate, a method was developed to combine the polycarbonate and aluminum. Variable length aluminum fingers and polycarbonate pads were used to adjust the confinement on the sample. A schematic of the finger/pad combination is depicted in Fig. 3.13. Because the total length between the frame and the sample was 33.35 mm, the thickness of pad and the length of finger, when added together, had to equal 33.35 mm. As the thickness of the pad increased, the length of the aluminum finger decreased, as did the overall confinement on the specimen.

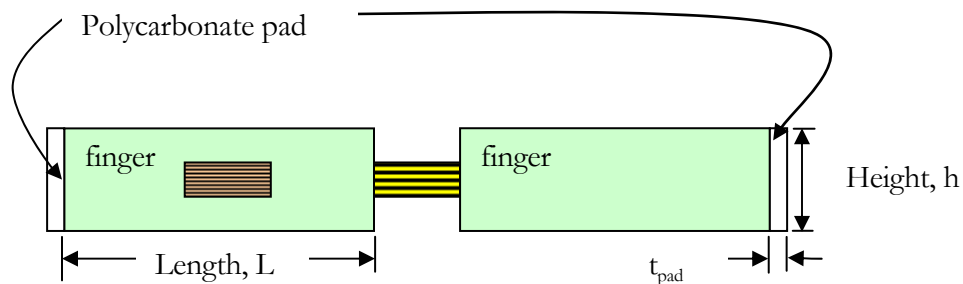


Figure 3.13. Schematic of cross section of fixture showing finger, and polycarbonate pad and specimen

With the polycarbonate pad between the finger and the frame, the total deflection was greater than that with only the solid aluminum finger. As stated earlier, confinement stress ($\sigma_{\text{conf.}}$) can be calculated from the strain gage reading on the aluminum finger. Figure 3.14 displays the results representative of an experiment using the polycarbonate pad, aluminum finger combination. The data represent a finger/pad combination with a pad thickness of 3.81 mm and a finger length of 29.54mm. As Figure 3.14 shows, the axial stress is greater than both the longitudinal and transverse stresses. In addition, because the composite has a tendency to elongate in the matrix dominated or transverse direction, as opposed to the fiber dominated longitudinal direction, the transverse confining stress is greater than the longitudinal confining stress.

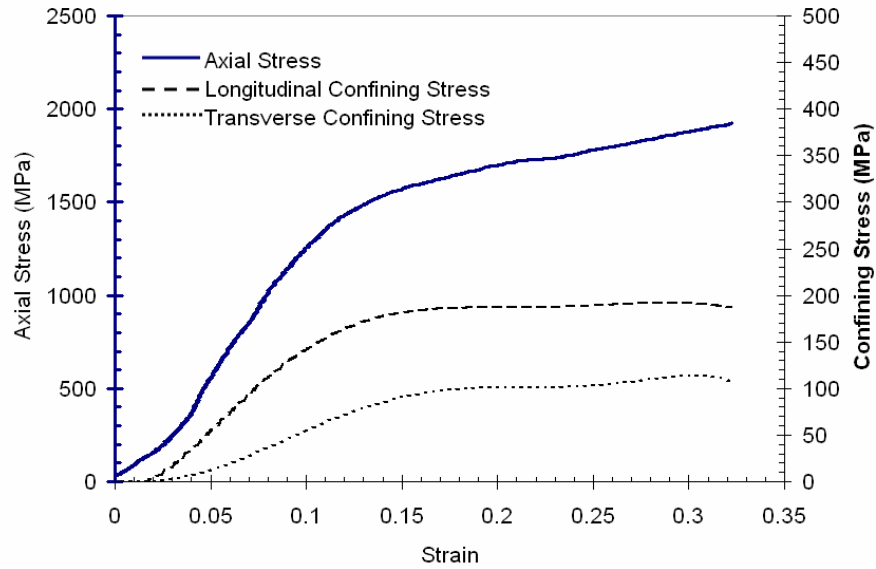


Figure 3.14. Typical result of nominal stress-strain data for transverse loading of S2/8552 glass/epoxy composite at a strain rate of 0.001/s.

3.6.1.2 Measuring Confinement with Strain gauges

Stresses on the sample are deduced from the readings of the strain gauges, which are located at the exact midpoint of the confining fingers. Figure 3.15 features a 2D cross section of the transverse finger specimen system. In order to determine the relationship between the strain gauge reading and the stress felt at the specimen-finger interface, finite element analysis using the commercial software ABAQUS was performed. The schematic of the model is presented in Fig. 3.15. A ramp displacement was applied at the end to simulate the boundary condition applied by the specimen. The displacement would ramp from 0 to 2 mm in a single time step. The other end, fixed in the x direction, was free to expand in the y direction. The finger rested on rollers, also indicated in Fig. 3.16. The aluminum finger was modeled as an elastic-perfectly plastic material with a Young's modulus of 70 GPa, Poisson's ratio of 0.34 and yield stress of 500 MPa.

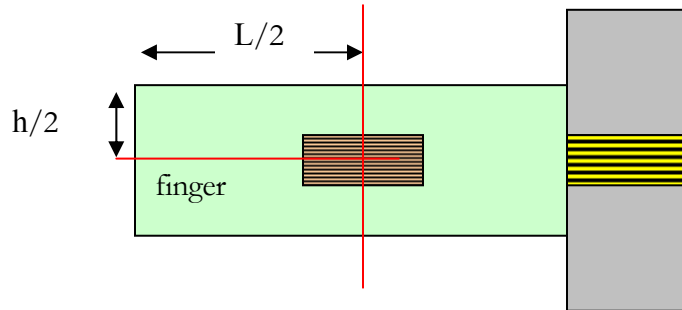


Figure 3.15. Cross Section of fixture showing finger, adapters, specimen and strain gauge location.

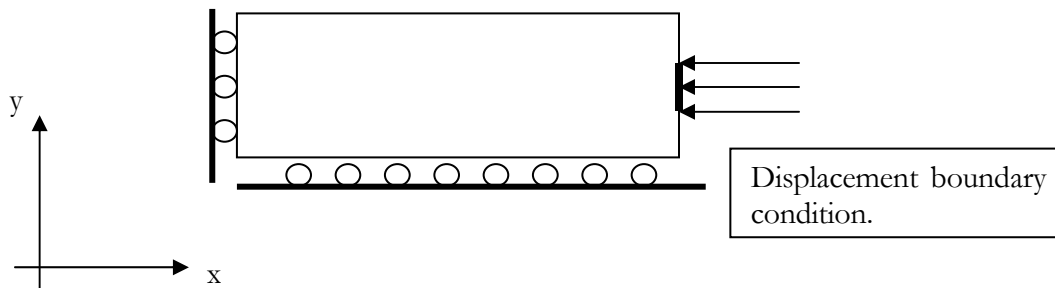


Figure 3.16. Schematic of finger with applied loads and boundary conditions used in finite element simulations.

The finite element calculations monitored the stress and strain of the finger at two different locations. The first location indicated by set# 1 in Fig. 3.17 measured the stress at the right hand end of the finger, and set# 2 monitored the stress and strain at the middle of the finger (which corresponded to the strain gauge location). The finger was discretized into a rough mesh with only 80 elements. A contour plot of the Mises stress in the finger during loading is displayed in Fig. 3.18. The nominal stress-strain curves for the elements indicated by the circles in Fig. 3.18 are graphed in Fig. 3.19. Element# 38 corresponds to the stress at the interface of the finger and sample; element# 3 corresponds to the location of the strain gauge. The maximum stress that element# 3 reaches is 248 MPa, while

element# 38 reaches a stress of 570 MPa, which demonstrates that the strain gauge reads a stress 56% less than actual stress level at the specimen. In order to compensate for this 56% lower reading, the strain gage results will be multiplied by 1.56.

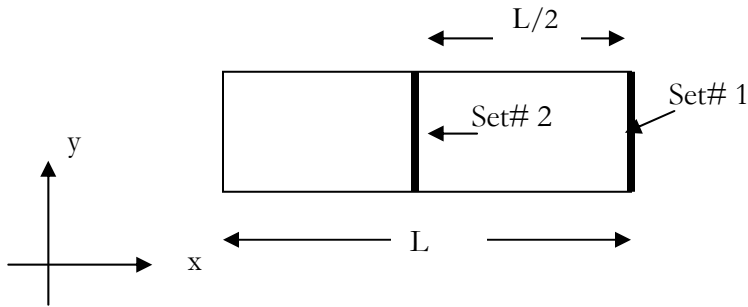


Figure 3.17. Location of monitoring sets in the finite element model.

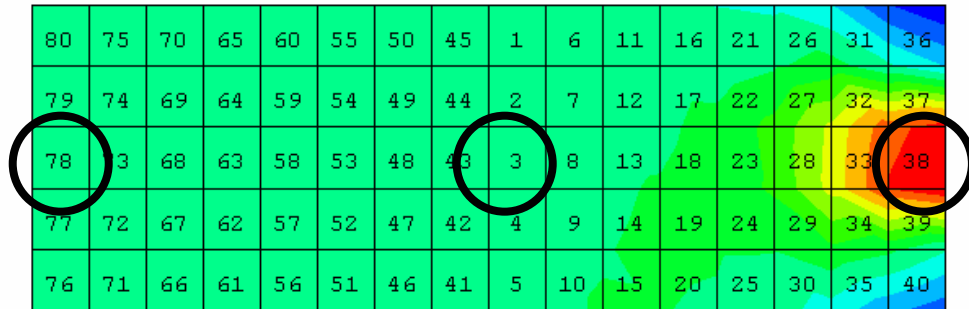
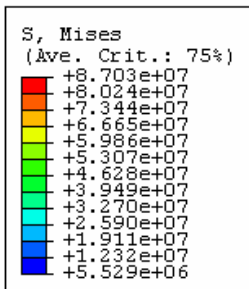


Figure 3.18. Contour plot of the Mises stress in aluminum finger under simulated loading.

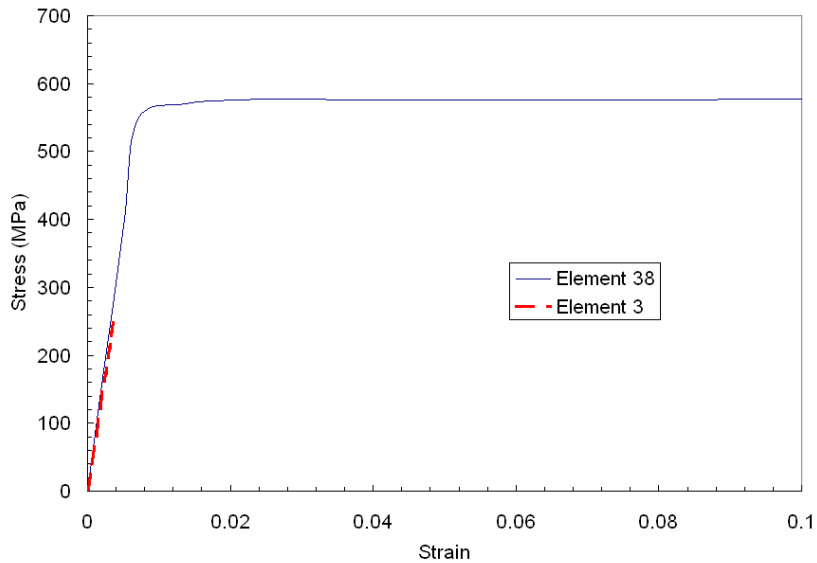


Figure 3.19. Plot of nominal stress strain curve at element# 38 and element# 3.

3.6.1.3 Indentation

Original tests were performed with the pad between the finger and the specimen, but the pad continually deformed unevenly, resulting in a non-uniform state of stress within the material. The indentation can be clearly seen in Fig. 3.20. To remedy this indentation, pad locations were changed from in between the sample and the aluminum finger to between the aluminum finger and the frame. When the tests were performed again with the change in place, the indentation was found to disappear accompanied by an increase in the compressive strength of the material. The difference in the data between these two locations is available in Fig. 3.21 while plotting the axial compressive strength as a function transverse compressive confinement.

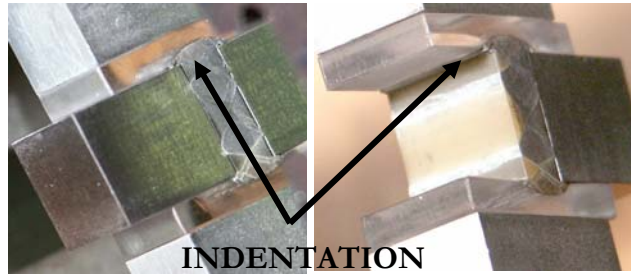


Figure 3.20. Indentation of inserts by the composite specimen

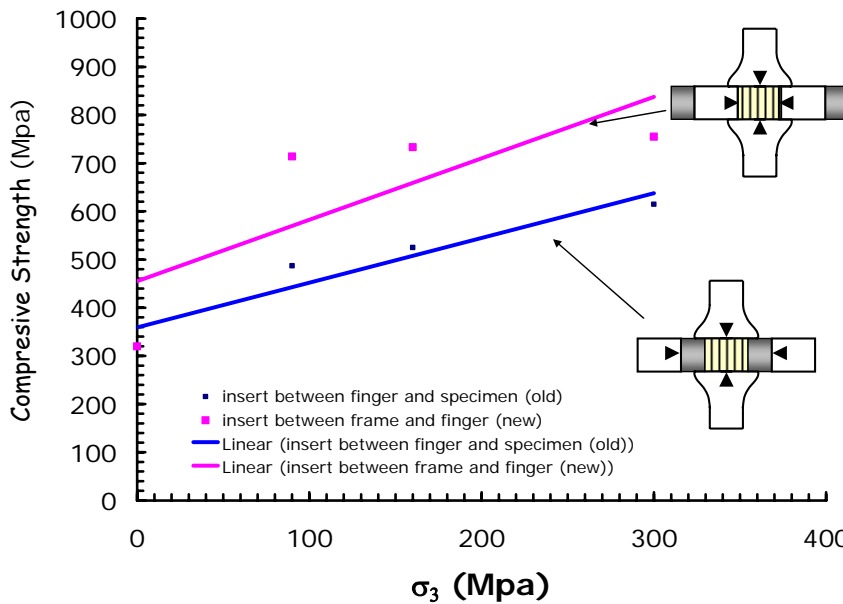


Figure 3.21. Effect of insert location on compressive strength

3.6.2 High Strain rate confinement Method

The original experimental setup for the dynamic tests called for the fixture used in the quasi-static test to be mounted on its side. However, problems arose with the implementation of the fixture into the Hopkinson bar. The fingers, which apply confinement in the quasi-static fixture, were aligned with each other by resting on the lower holder in the frame, while gravity kept the fingers in line with the specimen. With the fixture on its side, however, the fingers no longer rested on the holder. Removal of the

holder allowed the fingers to slide freely in the fixture finger slots. Because no ready solution to attach the fingers within the fixture could be found, a new fixture for the dynamic tests was developed.

Figure 3.22 shows a schematic of the fixture designed for use in the dynamic tests. The fixture consists of four parts, each removable and replaceable with components of different mechanical properties. Four different pairs of longitudinal and transverse fingers were constructed, one pair each of polycarbonate, aluminum, copper and steel. Two pairs of fingers were placed in opposing directions, allowing for 16 different configurations of longitudinal and transverse confinement. All 16 combinations were tested and the results are presented in the next section. The previous section discussed how varying the finger material varied the confinement on the specimens, through the suppression of expansion in the longitudinal and transverse fiber direction of the specimen. Figure 3.23 shows an example of the fixture with copper fingers in the longitudinal direction and steel fingers in the transverse direction. The four pieces were held together with four 3/16" steel set screws at the four corners of the fixture. As in the low strain rate fixture, the fingers themselves were thicker than the specimen, so a steel adapter transferred the load from the bar to the specimen. Strain gauges were placed on two of the fingers: the first on a longitudinally aligned finger, and the other on a transversely aligned finger. A Wheatstone bridge connected the strain gauges to a 4 channel digital storage oscilloscope with a 12 bit digitizer at a 10 MHz sampling rate per channel. Figure 3.24 presents typical measurement readout, containing the four signals gathered in a test. The first two are the incident and reflected pulses from the strain gauges located on the incident bar and the transmission bar. The second two signals are gathered from the strain gauges located on the fixture, one that measures the longitudinal response of the specimen, and the other that measures the transverse response of the specimen.

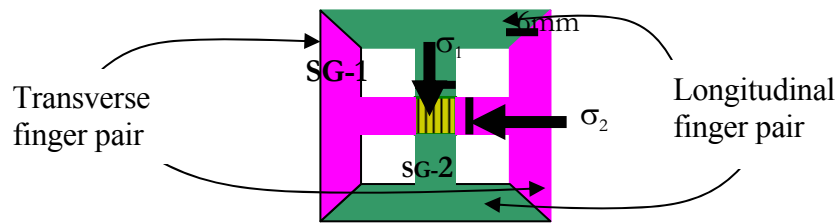


Figure 3.22. Schematic of the confinement fixture used in the dynamic test to introduce varying levels of confinement.

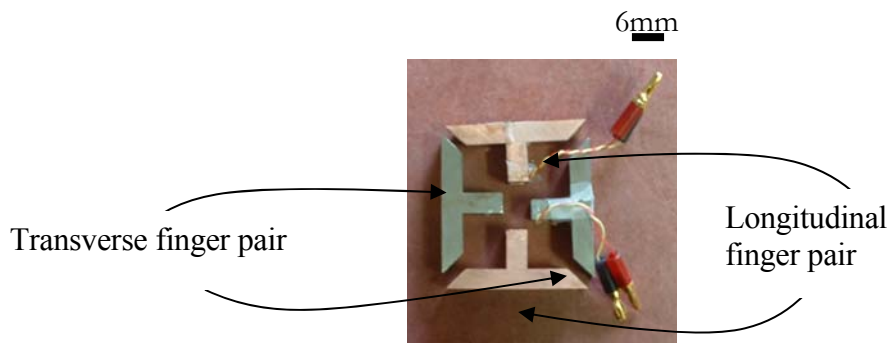


Figure 3.23. Photograph of the confinement fixture used in the dynamic test to introduce varying levels of confinement.

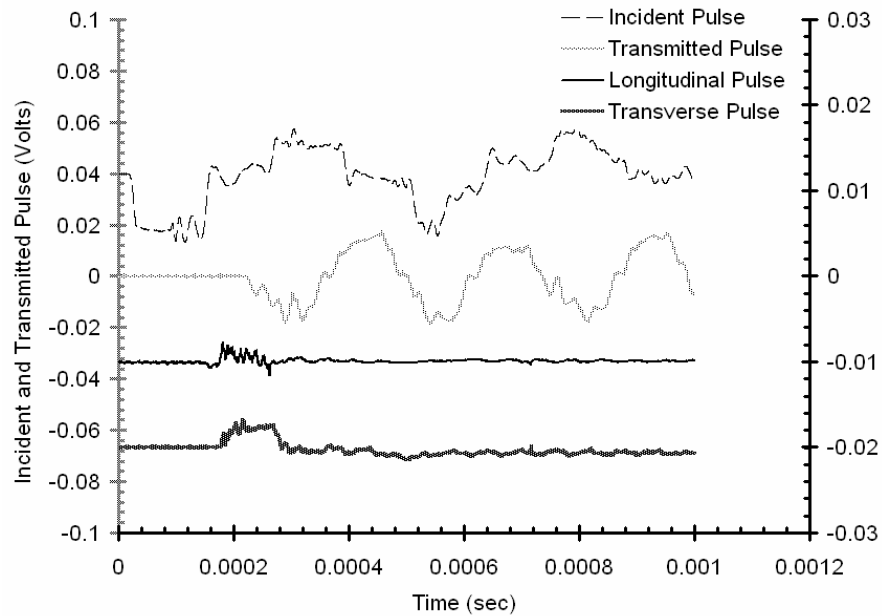


Figure 3.24. Sample output from Dynamic tests, showing incident and transmitted pulse determined from the Hopkinson bar strain gages and longitudinal and transverse strain gage output on the confinement fixture.

3.7 Experimental Results for Low Strain Rate Tests

This study was concerned with the failure behavior of s2/8552 glass/epoxy composite under multi-axial loading. The failure of a materials system is traditionally defined as the critical value of a controlling parameter that marks the limit of the materials functional range (Gould, 1994, p. 202). The stress strain curve of the unconfined unidirectional composite under simple compression dictates that when the ultimate strength of the material is reached, catastrophic failure results. The stress strain curve for the uniaxial compression with no confinement is presented in Figure 3.25. In this test, the failure value is measured at the peak stress, or 178 MPa.

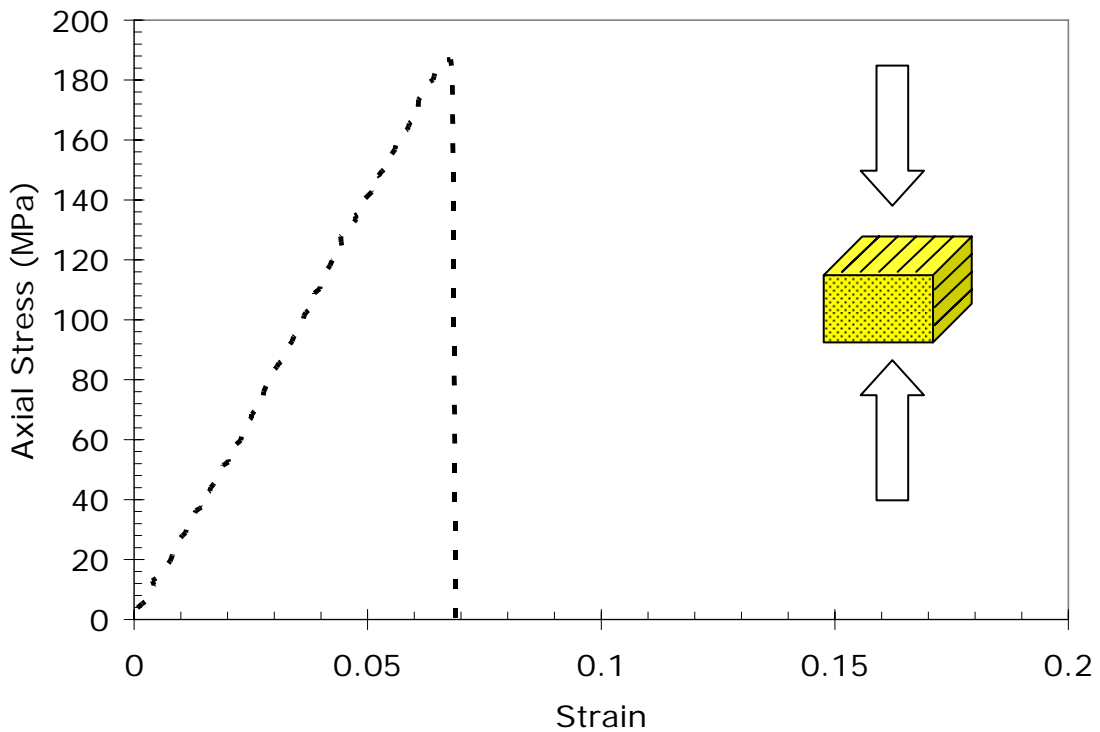


Figure 3.25 Stress strain curve of uniaxial compression of S2/8552 glass/epoxy composite

Once confinement is added, the stress strain curve reaches the yield strength and exhibits nonlinear behavior, as shown in Fig. 3.26. The failure values of σ_1 and σ_2 were taken at the intersection of the stress strain curves and the line drawn at 15% strain, indicated in Fig. 3.26.

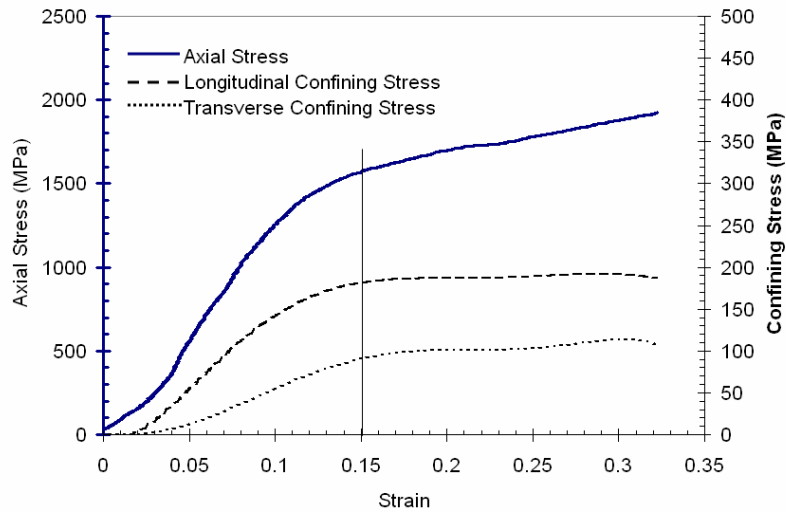


Figure 3.26 Typical result of typical nominal stress strain data from a quasistatic test conducted at 0.001/s.

The S2-glass/epoxy composite specimens were all loaded normal to the fiber plane. The low strain rate tests ($\dot{\epsilon}=10^{-3} \text{ s}^{-1}$) can be separated into two categories: tests with the pad/finger confinement, and tests with a solid finger made of different materials. The pad/finger tests will be discussed first.

The pad/finger combination tests comprised five different pad thicknesses for both the longitudinal and transverse directions. The nominal pad thicknesses were 1.27, 2.54, 3.82, 5.06 and 6.36mm, thus allowing for 25 separate pad/finger combinations. As previously discussed in section 3.6.1.1, increasing pad thickness decreases the confinement stress on the specimen. The longitudinal confinement stress on the specimen (σ_1) was

calculated using the strain gage reading on the finger. The transverse confinement stress on the specimen (σ_2) was similarly assessed.

While the pads in both the transverse and longitudinal directions exhibited permanent deformation, the aluminum fingers were not deformed. Their dimensions were measured before and after each test to confirm that they had not sustained permanent damage. Consequently, the same fingers could be used again for different pad thicknesses. The non-deformation of the aluminum fingers was also significant, in that the stresses sustained by the fingers were within the material's elastic limit.

The effect of confinement on the axial stress strain curve of the material is illustrated in Fig. 3.27. The set of tests shown have the same confinement in the longitudinal direction but varying confinement in the transverse direction. The transverse confinement ranges from no confinement to pad/finger confinement to solid aluminum finger confinement in the transverse direction. As found in previous work by Vural *et al* (2002), the longitudinal and transverse confinement suppresses the failure in the material, allowing the material to achieve higher axial stresses and failure strains. Under no confinement, the failure strain is approximately 0.6%, and when subjected to 5.08 mm pad thickness confinement, the failure strain jumps to 1.5%. As the transverse pad thickness decreases, confinement increases, as well as the failure stress and strain.

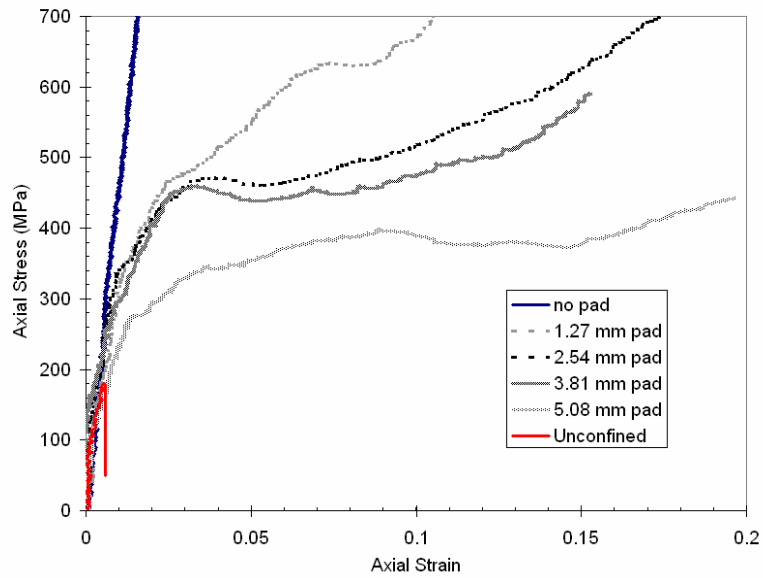


Figure 3.27. Axial Stress-strain response of S2-glass/epoxy unidirectional fiber composite with aluminum finger in longitudinal direction and varying pad thickness in transverse direction.

The pad/finger tests revealed that the axial stress was more significantly affected by transverse confinement, as opposed to longitudinal confinement. Figure 3.28 presents results with the same confinement in the transverse direction and increasing confinement in the longitudinal direction. The graph indicates that increasing longitudinal confinement has little effect on the axial strength of the material. The data presented in the previous section revealed that increasing longitudinal confinement had little effect on the transverse strength of the material. Figure 3.29 features a summary of all pad/finger combinations and shows that longitudinal confinement also has little effect on the axial strength of a material. As Fig. 3.30 shows, the dependence of axial strength on transverse confinement is much greater than that on longitudinal confinement.

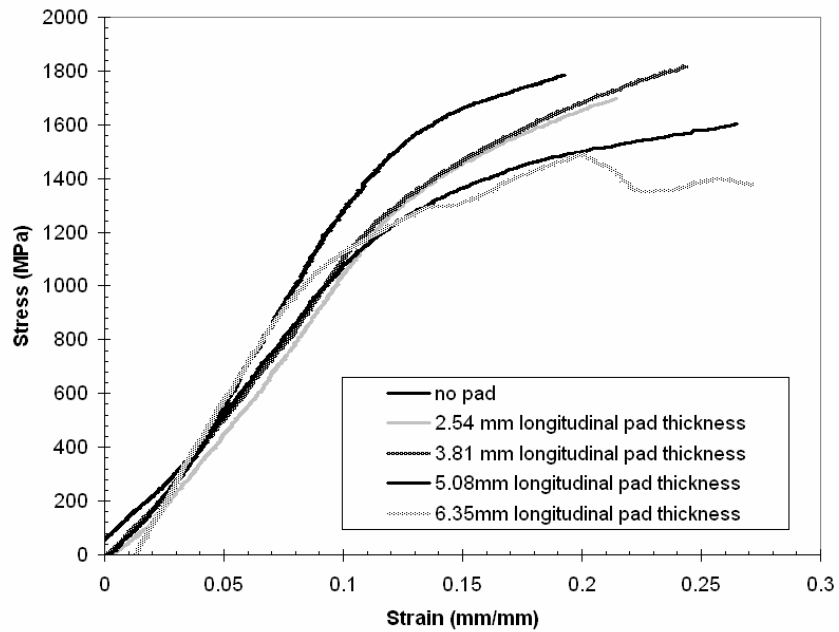


Figure 3.28. Axial Stress-strain response of S2-glass/epoxy unidirectional fiber composite with aluminum finger in transverse direction and varying pad thicknesses in longitudinal direction.

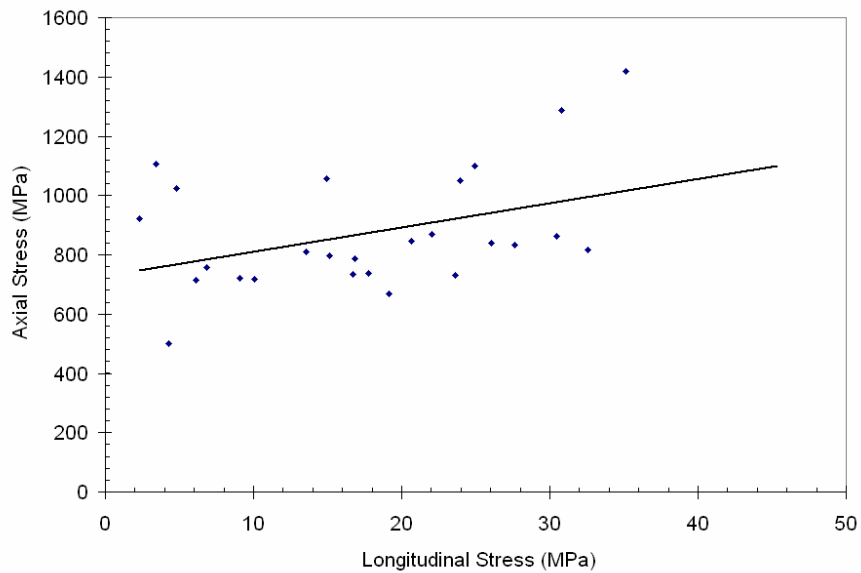


Figure 3.29. Axial strength as a function of longitudinal confinement for different pad/finger combinations.

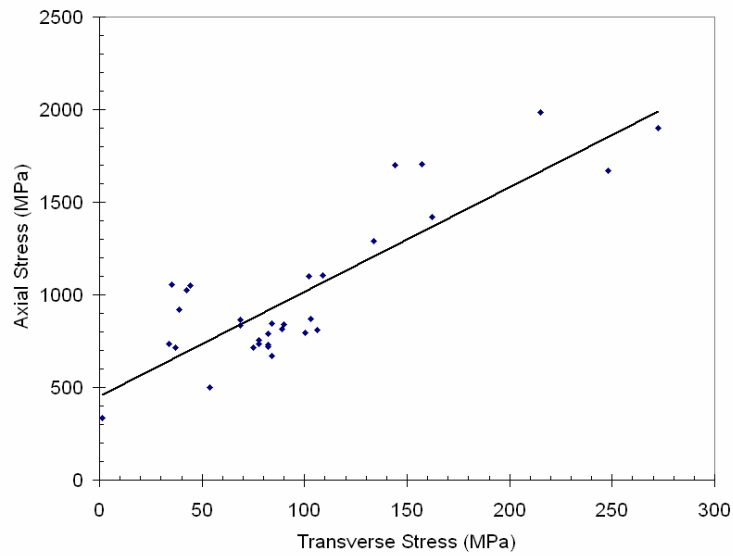


Figure 3.30. Axial Stress-strength of S2-glass/epoxy as a function of transverse strength for different pad/finger combinations

Figure 3.31 plots the absolute values of the transverse confining stress as a function of the absolute values of the longitudinal confining stress. The data indicate that the transverse confining stress does not vary with the confinement in the longitudinal direction. In addition, the confinement in the longitudinal direction is an order of magnitude lower than the confinement stress in the transverse direction. This suggests that the failure behavior of S2/8552 glass/epoxy composite is more dependent on the transverse loading of the structure than the longitudinal loading.

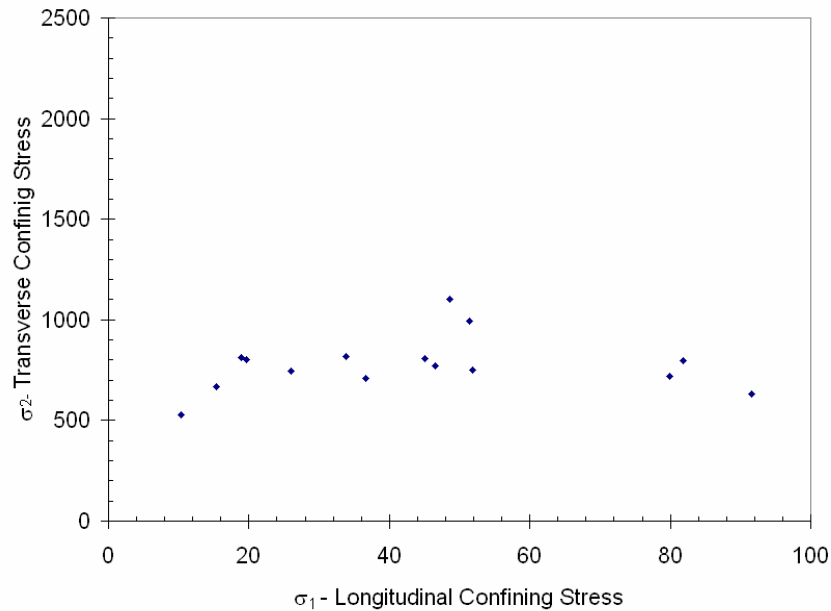


Figure 3.31. The transverse confining stress, σ_2 , as a function of the longitudinal confining stress, σ_1

Figure 3.32 shows a comparison between the Tsai-Wu and Christensen failure envelopes to the experimental data. Compression stress is designated as a negative stress so the confining stresses, σ_1 and σ_2 , are plotted as negative values. The plot demonstrates that for a given longitudinal confinement stress, the onset of failure can be delayed by increasing the transverse confinement stress. More information on how the longitudinal confining stress influences failure was desired. In order to increase the confinement on the longitudinal face, the finger/pad combination was replaced by a single finger made of a material such as aluminum, copper or steel.

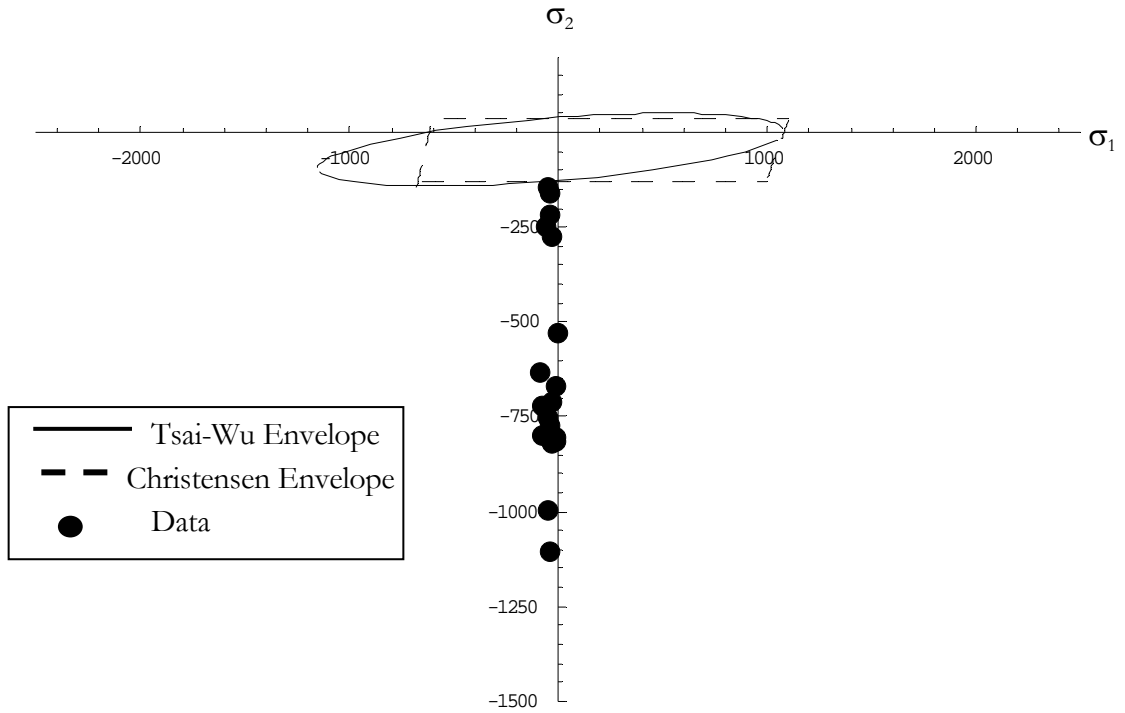


Figure 3.32. A comparison of the Tsai-Wu, and Christensen failure envelopes with experimental data for S2/8552 composite.

Variation in the confinement on the specimens in the longitudinal and transverse fiber direction was achieved by using “fingers” made of various materials. The three materials used for the fingers were aluminum, copper and steel. These three materials were chosen because they were readily available and their Young's modulus and yield strength were diverse. Test results were grouped by the material used in the finger in the longitudinal direction. Figure 3.33 shows the axial stress versus strain curves for the tests with an aluminum finger in the longitudinal fiber direction. It is readily seen that the specimens confined with copper fingers in the transverse direction exhibited the lowest axial strength, followed by aluminum and finally steel. Axial stress strain curves for tests

with copper and steel as the longitudinal confining finger, shown in Figs. 3.34 and 3.35, respectively, again revealed that the specimen confined with copper in the transverse direction exhibited lower axial strength than aluminum or steel.

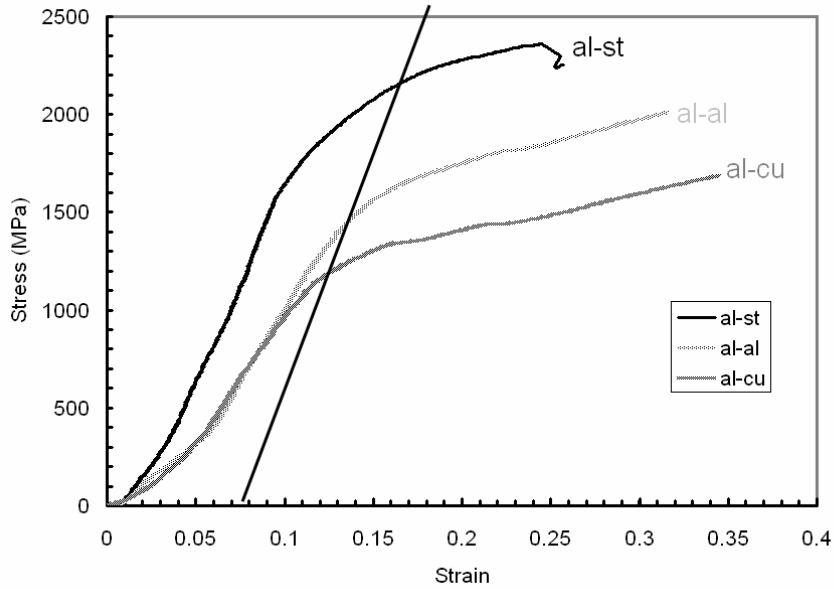


Figure 3.33. Axial Stress Strain curves for aluminum finger in longitudinal fiber direction.

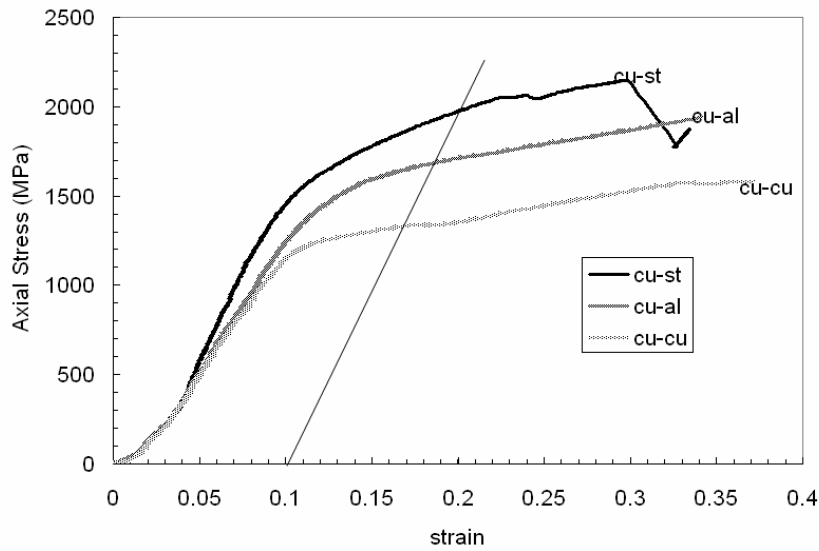


Figure 3.34. Axial Stress Strain curves for Copper finger in longitudinal fiber direction

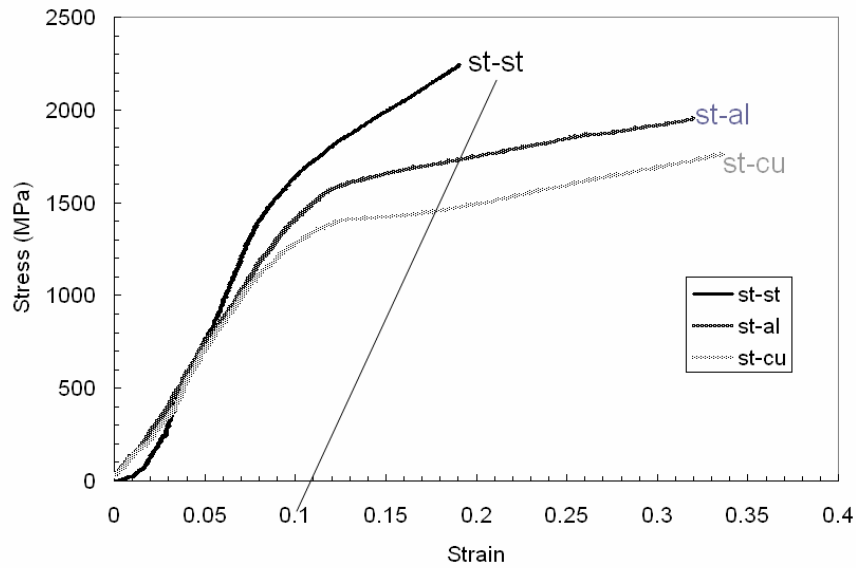


Figure 3.35. Axial Stress Strain curves for Steel finger in longitudinal fiber direction

Figure 3.361 presents the axial strength of the material (taken at 20% strain) as a function of the longitudinal confining strength. The axial strength is seen to increase with increasing longitudinal confinement strength. The plot of axial strength versus transverse confining stress in Fig. 3.37 shows the axial strength also increasing with transverse confinement strength. The Transverse strength of the material is seen to increase with longitudinal confining strength, as illustrated in Fig. 3.38.

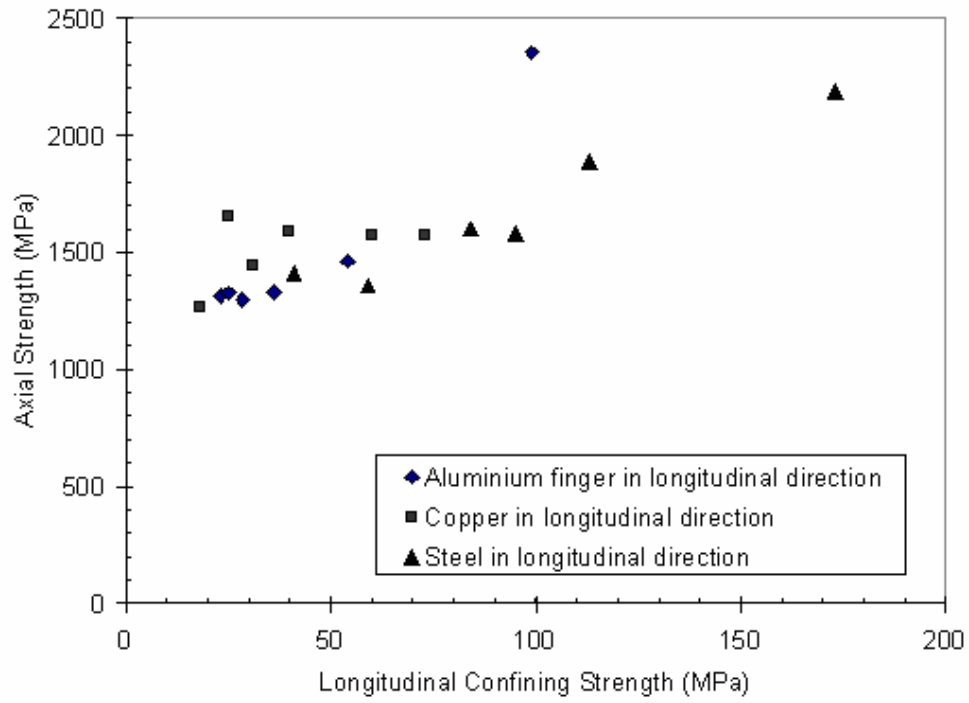


Figure 3.36. Axial Strength as a function of longitudinal confining stress of composite material for various finger combinations.

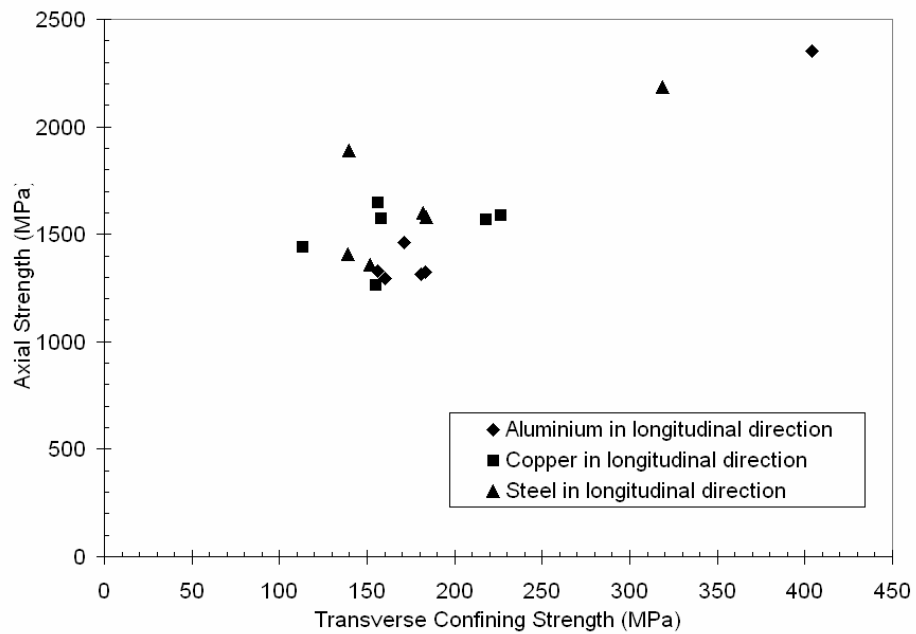


Figure 3.37. Axial Stress as a function of transverse confining stress for various finger combinations.

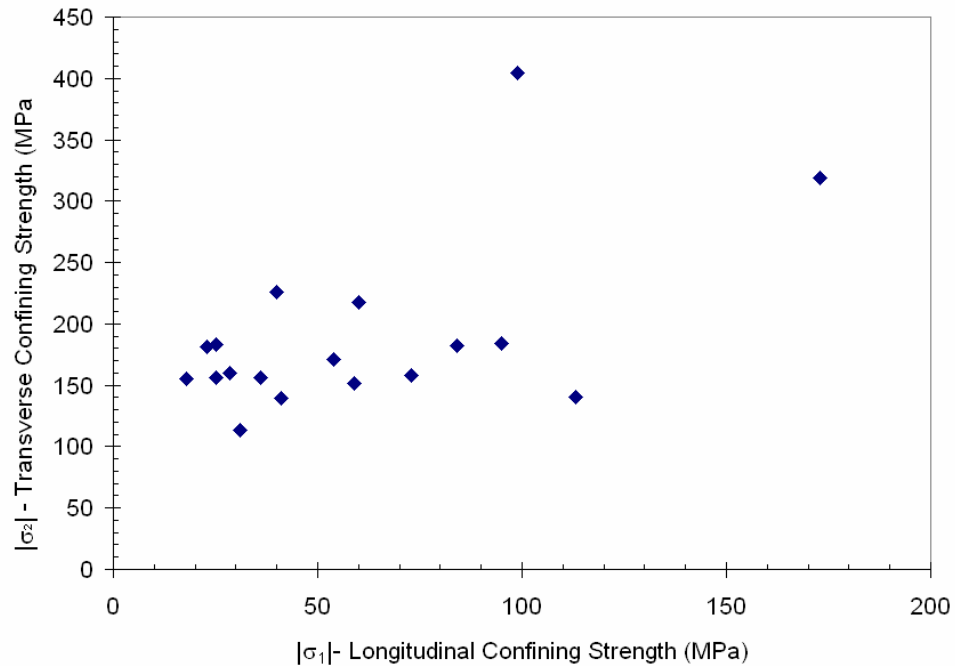


Table 3.38. Absolute value of transverse stress as a function of absolute value of longitudinal stress of composite material for various finger combinations.

The tests performed with the aluminum, copper and steel fingers were conducted to obtain higher values of longitudinal confining stress. However, values of longitudinal confinement stress did not reach values much higher than observed with the pad/finger tests. The compression strength of unidirectional S2/8552 glass epoxy in the longitudinal direction is 620 MPa. For the test with the strongest confinement in the longitudinal and transverse fiber direction, the steel-steel test, the maximum longitudinal confinement achieved was 120 MPa.

Since it seemed that the longitudinal confinement had little effect in the axial strength of the specimen, a test with no confinement in the longitudinal direction but steel in the transverse direction was conducted. The resulting axial stress strain curve for no confinement in the longitudinal direction is seen in Fig. 3.39, along with the stress strain curves for transverse steel confinement and longitudinal confinement provided by aluminum, copper and steel. This test showed however, that the case of no confinement in

the longitudinal direction was lower than the case of aluminum, copper or steel in the longitudinal direction.

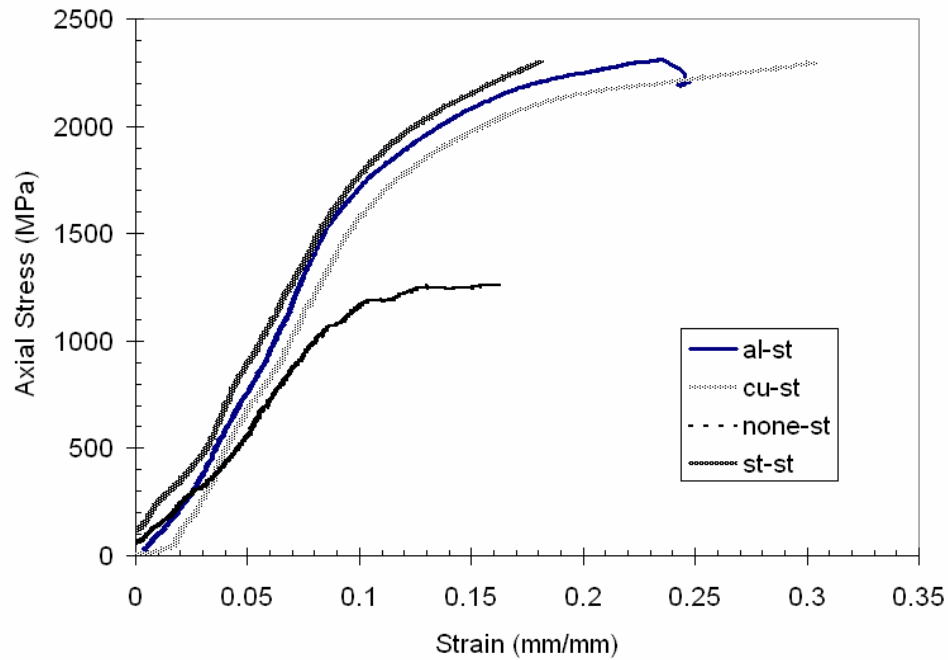


Figure 3.39. The stress strain curves for steel finger in the transverse direction with longitudinal confinement being varied by changing confining finger materials from aluminum, copper and steel and finally no confinement in the transverse direction

3.8 Micro-structural Characterization

The most obvious question arises from the fact that the case aluminum confinement has a higher axial strength than the case of copper. This is odd, since the yield strength and Young's Modulus of copper is greater than that of aluminum. Tests were performed with copper, and steel in the longitudinal fiber direction to see whether or not these same phenomena were observed at different longitudinal confinements. Indeed, for all longitudinal confinements, the copper finger in the transverse direction was lower than the case of aluminum in the transverse direction. Pictures of the specimens after tests shed some light on why the maximum axial stress was lower for the transverse copper confinement as opposed to the aluminum transverse confinement. Figures 3.40 (a) and (b) show two specimens which had aluminum finger confinement in the longitudinal direction

and different confinement in the transverse direction. Figure 3.40 (a) had aluminum confinement the transverse direction and Fig. 3.40 (b) had copper confinement in the transverse direction. The ends of both samples show a mushroom effect. The mushroom in Fig. 3.40a is smaller than one in Fig. 3.40b. This can be explained by examining a simple finite element model of the experiment.

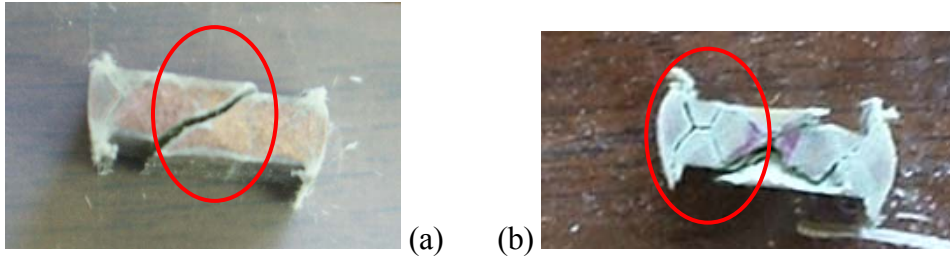


Figure 3.40. (a) Photograph of specimen with aluminum finger longitudinal confinement and aluminum finger transverse confinement. (b) Photograph of specimen with aluminum finger longitudinal confinement and copper finger transverse confinement.

The results of the finite element simulation shown below in Fig. 3.41 was for a copper finger aligned in the transverse fiber direction. The specimen is compressed it forces the finger to deflect and a gap forms between the finger and the spacer. The specimen can deform in one of two ways, it can continue to indent the finger or choose to mushroom into the space between the finger and the spacer. From Fig. 3.40 above, the specimen transversely confined with aluminum chose to indent the aluminum, increasing the confinement, thus increasing the axial stress needed for compression. The specimen transversely confined with copper chose to deform into the space between the finger and the spacer. The axial stress needed to compress the specimen into the gap was less because there was no resistance to deformation in the gap as there was into the aluminum finger. The gap formed by the specimen and copper was larger than the gap for aluminum. This would explain why the copper had higher transverse confining stress read by the strain gauge.

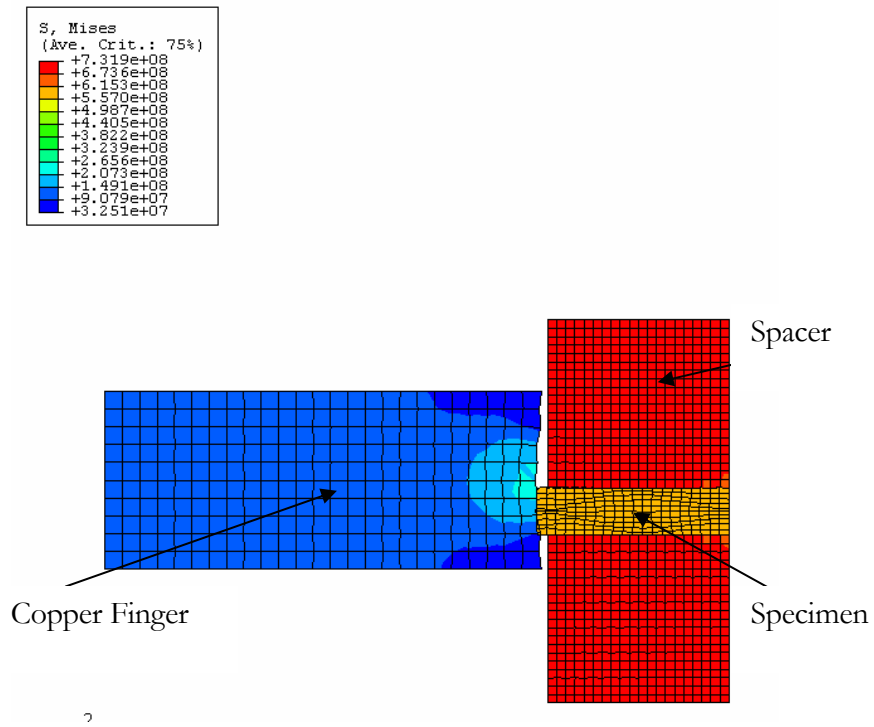
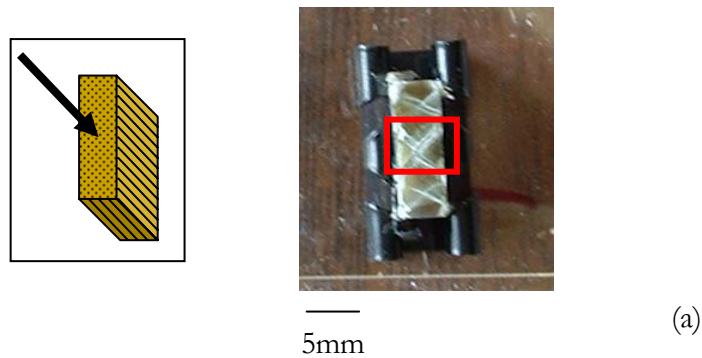


Figure 3.41. Finite element model of deforming specimen with copper transverse finger confinement.

Post-test inspection of the specimens revealed shear failure planes at $\sim 50^\circ$ to the longitudinal surface. The pictures in Fig. 3.42 are from a specimen deformed with aluminum confinement in the longitudinal and transverse fiber direction. The picture on left shows the entire longitudinal face of the sample. The SEM micrograph on the right provides a more magnified view of the region of the specimen indicated by the red box in Fig. 3.42(a). The arrows on either side of Fig. 3.42(b) show the direction of axial loading.



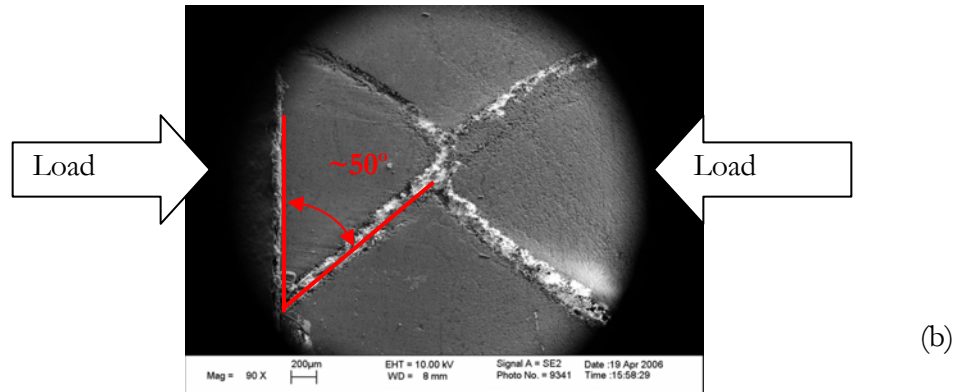
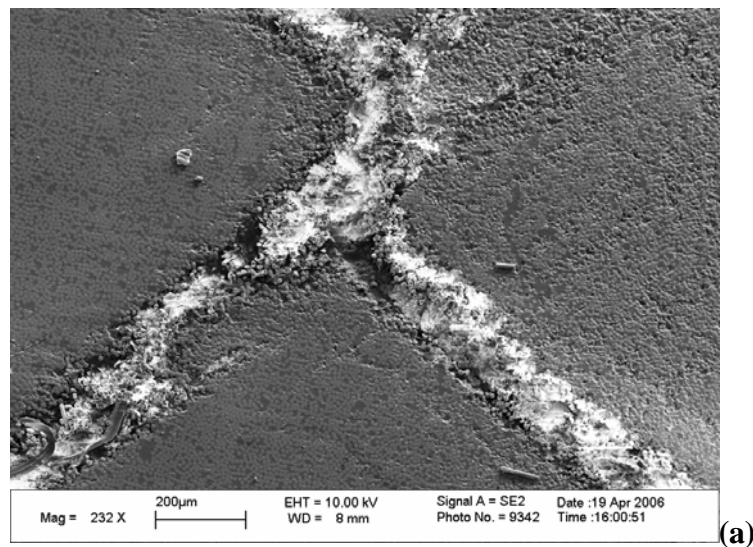
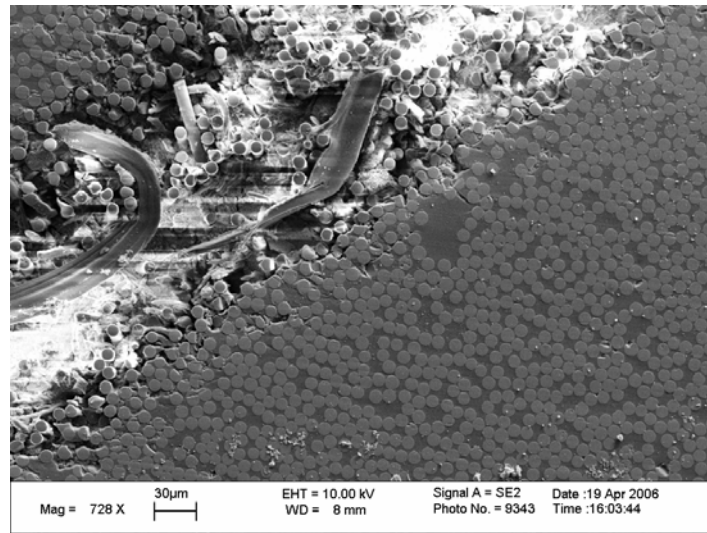


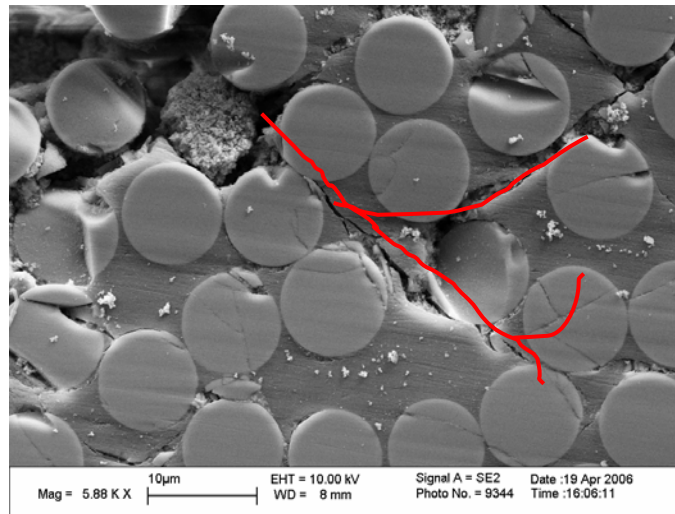
Figure 3.42. (a) Photograph of specimen with all around aluminum confinement (b) SEM micrograph of boxed area in (a) with angle of shear failure indicated

As the magnification of the failure plane is increased more, features of the failure become evident. Figure 3.43(a) shows that the fibers in the failure plane are visibly detached from the matrix material. Increasing the magnification reveals cracks emanating perpendicular to the failure plane, into the material. At the highest magnification (5800 X), the cracks traveling around the harder fibers into the matrix material are clearly seen, causing the size of the shear failure band to increase. The sequence of micrographs also clearly demonstrate the transverse failure being dominated by the flow and failure of the matrix material.





(b)

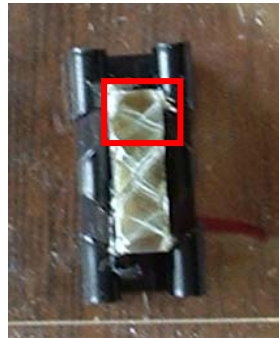


(c)

Figure 3.43. SEM micrographs of a specimen confined by aluminum at varying magnifications, (a) 232 X, (b) 728 X and (c) 5.88 KX.

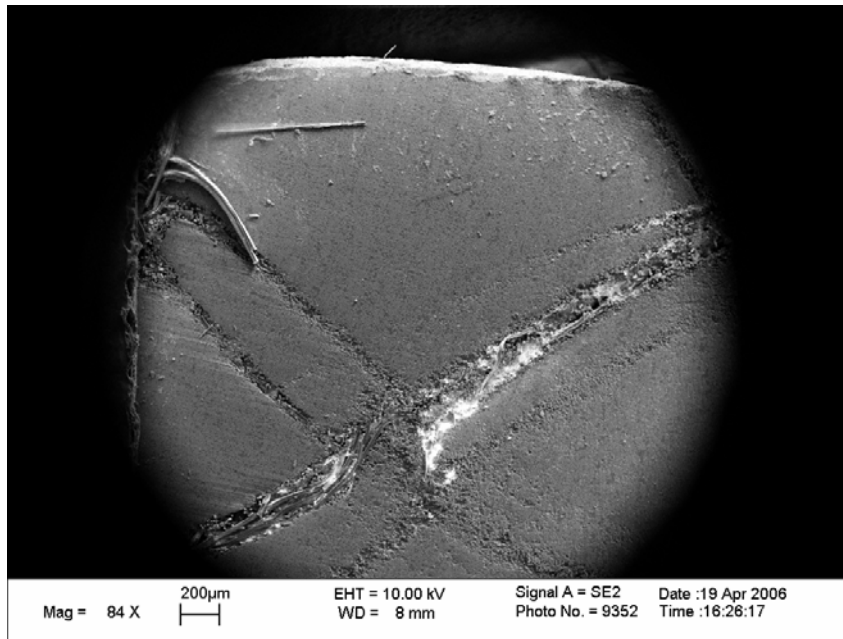
Upon further investigation of other regions on the sample, two parallel failure bands were located toward the upper edge of the sample, indicated by the box in Fig. 3.44(a). Fig. 3.44(b) is an SEM micrograph of the boxed region. It shows that there are two small cracks growing perpendicular to each of the failure bands. As the two cracks approach mid-distance between the two parallel failure bands, a third crack parallel to the failure bands is found that connects the two minor failure bands in Fig. 3.45(a). Another

crack is also seen in Fig. 3.45(a) and is encircled in the figure. Higher magnification micrograph, Fig. 3.45(b), reveals the hairline fracture running parallel to the main failure plane. Figure 3.45(b) shows the crack running between the fibers of the sample, as seen in the previous region studied. However, this crack can be followed to its initiation point and a 14640X micrograph (Fig. 3.45(c)) was taken of this region.



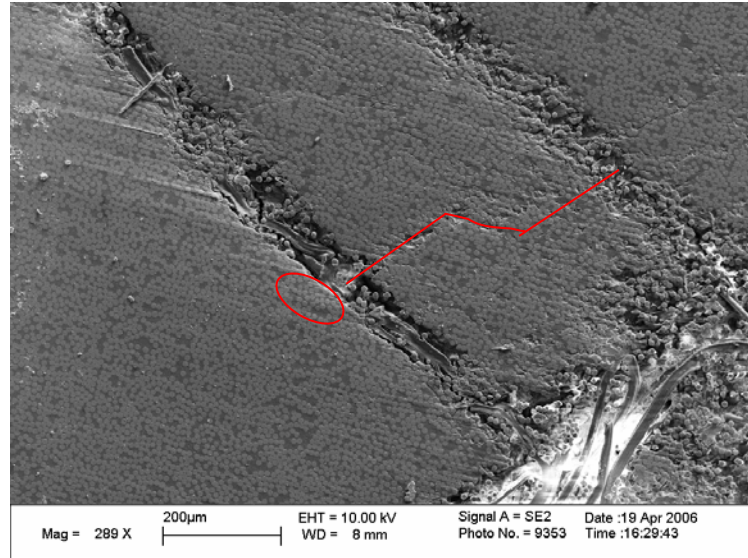
5mm

(a)

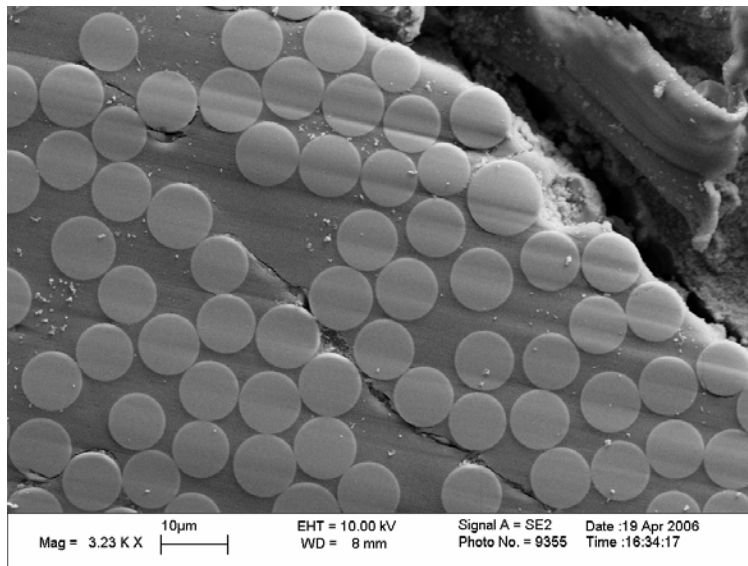


(b)

Figure 3.44. (a) Picture of the specimen confined by aluminum; (b) SEM micrograph of boxed region in (a).



(a)



(b)

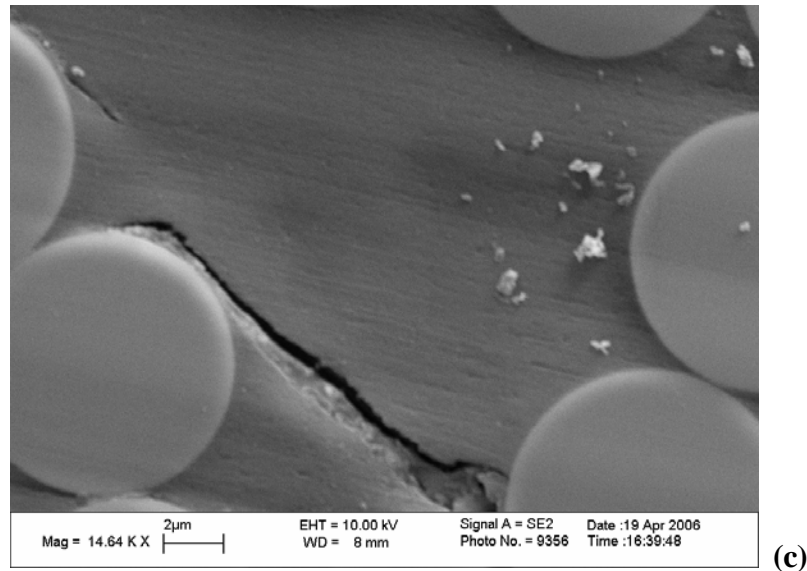


Figure 3.45. SEM micrographs of the specimen in Fig. 3.49 at (a) 289X, (b)3200 X and (c) 14640X.

The longitudinal face of the specimen that sustained the largest confinement, (Fig. 3.46) had surprisingly dissimilar features than that of the lesser confined specimens (Figs. 3.43, 3.44, and 3.45). The strongest confinement was provided by steel fingers in both the longitudinal and transverse fiber directions. Instead of the distinct failure planes seen in other tests, the photograph of the steel confined specimen shows a longitudinal face which looks very uniform. However, upon investigation in the SEM, it is clear that damage has occurred in the specimen. Instead of evenly distributed glass fibers in an epoxy matrix, regions of fiber-rich and fiber-free areas have developed, i.e. phase separation.

It is suspected that since the specimen was not allowed to deform during loading, the energy applied was converted to heat. This heated the epoxy material enough to where the fibers could pass freely through the matrix. These conditions of multi-axial loading and heating are very similar to the manufacturing process of composite materials, autoclaving. The autoclaving process heats and compresses several sheets of “prepreg” material together to form a single structure. The “prepreg” material is usually doped with extra matrix material, which is bled off during the curing process. In the case of this experiment, there

was nowhere for the excess epoxy to go once the fibers had been compacted, so it simply solidified, causing the final specimen to have fiber-rich and fiber-poor areas, resulting in a banded structure seen in Fig. 3.46(a).

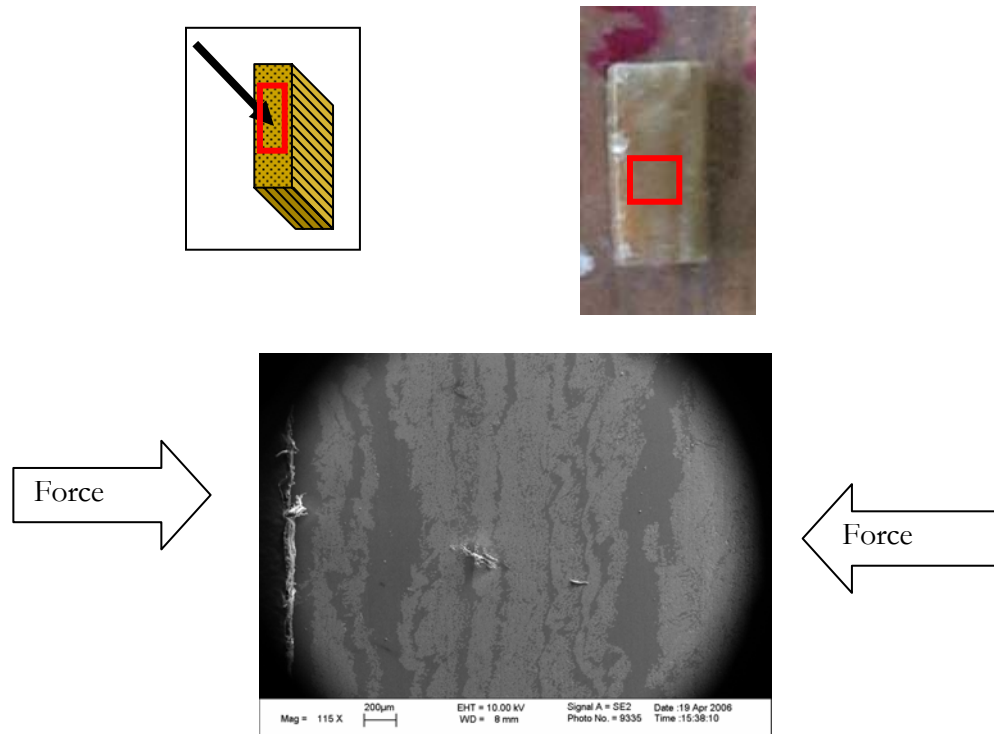
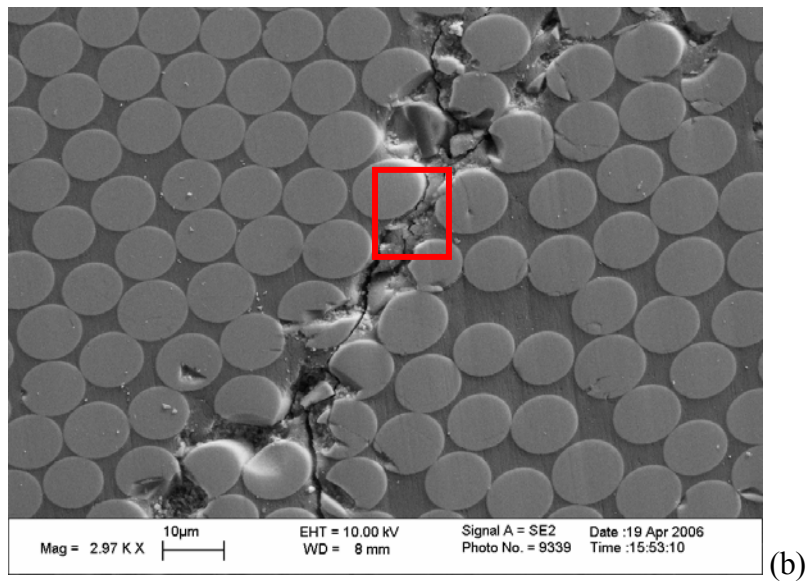
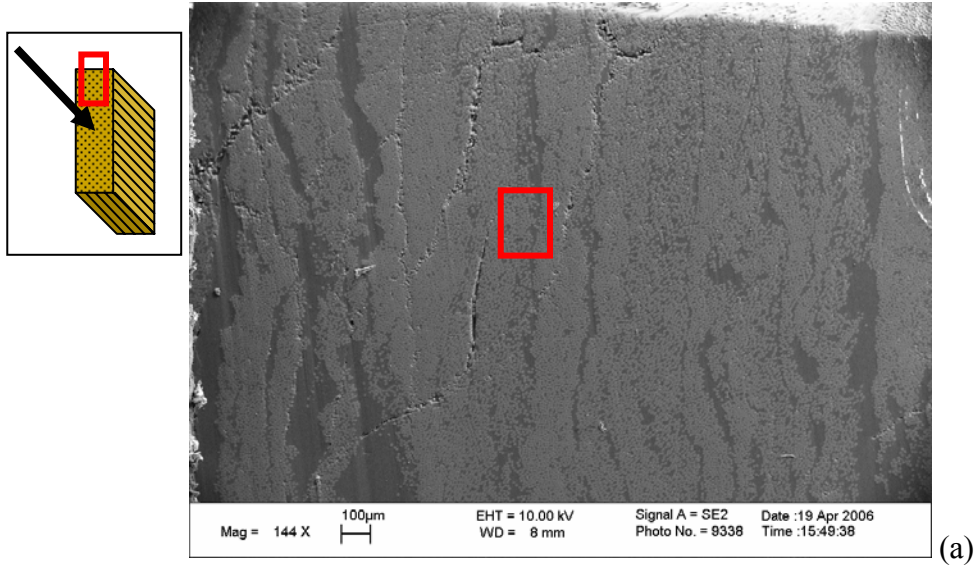


Figure 3.46. (a) Photograph of composite specimen confined by steel; (b) SEM micrograph of the specimen at higher magnification.

Upon closer inspection of the upper portion of the specimen, some small fracture surfaces were seen in Fig. 3.47. The magnified image of the region indicated by the box shows that the crack had trouble avoiding the hard fibers as it propagated, and therefore in the view of the fibers themselves, Figs. 3.48(b) and (c), there appears to be more damage to the fibers. Also, note that these cracks are much thinner, on the order of $2\ \mu\text{m}$, as opposed to the weakly-confined specimens that have a damage zone thickness of $100\ \mu\text{m}$. This observation is important because at the beginning of the chapter, it was proposed that

confining the specimen delayed failure because it suppressed the crack growth in the material.



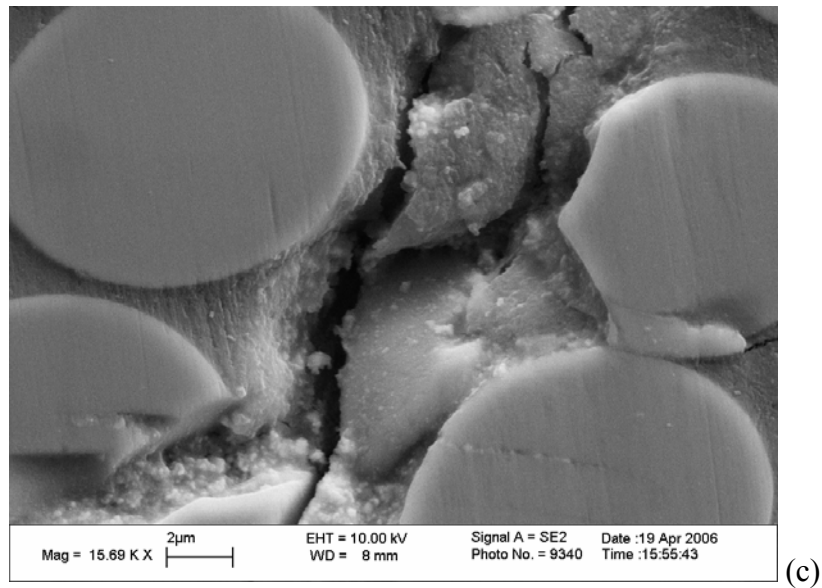


Figure 3.47. SEM micrographs of specimen confined with steel fingers in both the longitudinal and transverse fiber direction: (a) 114X, (b) 2,970 X and (c) 15,690 X.

3.9 High Strain Rate Results

The high strain rate experiments were performed using a Kolsky pressure bar setup (Fig. 3.7) described in section 3.5. The confinement fixture (Figs. 3.22 and 3.23) used in conjunction with the high strain rate experiments has been described in section 3.6.2. The experimental set-up used in the high strain rate tests involved using a spacer between the specimen and the incident bar and the output bar. The signals were unaffected by the addition of the spacers. The longitudinal and transverse confining stresses were monitored by two strain gauges, one located on the longitudinally-aligned finger and one on the transversely-aligned finger. Typical signals from the strain gauges on the bars and the confinement fingers can be seen in Fig. 3.24. Standard data reduction procedures were used to compute the axial stress and strain during high strain rate deformation.

As in the low strain rate tests, finite element simulations using Abaqus were employed to determine how the stress at the strain gauge related to the stress at the interface with the confining finger and specimen. The strain gauge was located at the center of the “leg” of the high strain rate confinement finger. The length of the leg, L_f , is label in

Fig.3.48 (a), the thickness of the leg, T_f , is labeled in the side view of the fixture in Fig. 3.48(b).

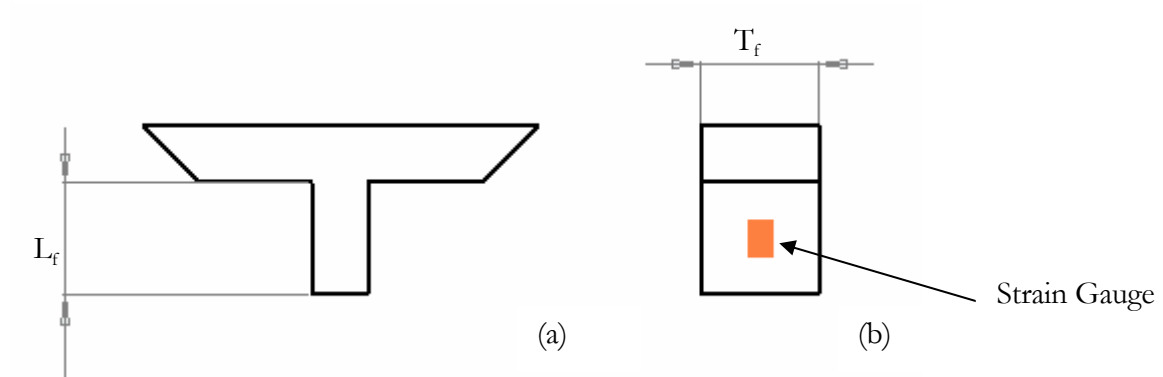


Figure 3.48. Schematic of the finger used in the high strain rate test: (a) front view and (b) side view. The side view also indicates the location of the strain gauge.

The results from the simulations are illustrated in Fig. 3.49. Figure 3.49(a) shows a cross-section of the finger as viewed in the direction of the arrow indicated in the schematic of the finger. The force applied indicated by the arrows on the right hand side of the specimen, and the left and bottom sides of the fingers were modeled to be on rollers. Figure 3.49(b) plots the stress-strain of element# 37 and element# 28 under loading. The stress in element# 28 reaches a value of 463 MPa, while in element# 37 it only reaches a value of 192 MPa. This means that the strain gauge reads a lower strain than the actual strain on the specimen. In order to correct for this, the measured strain must be multiplied by 2.41.

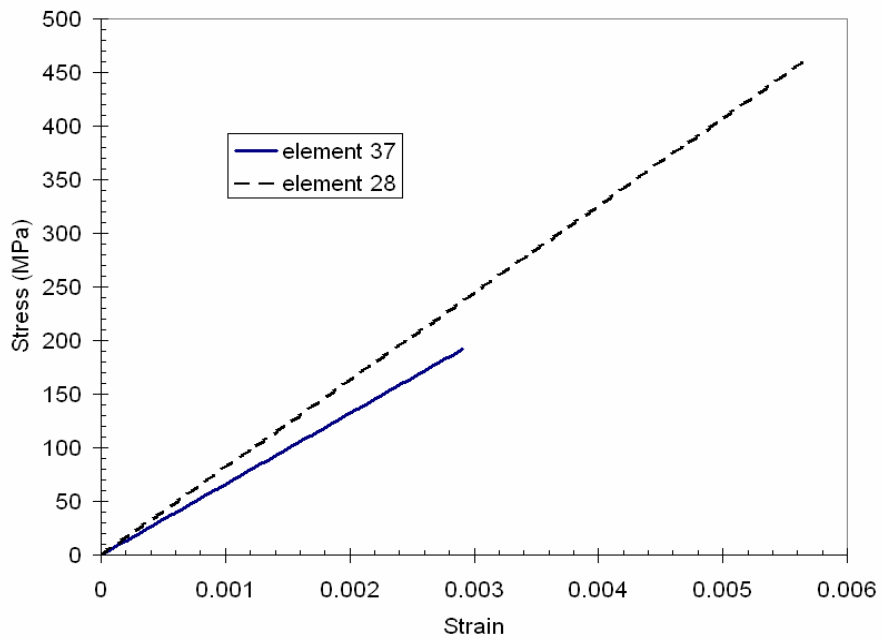
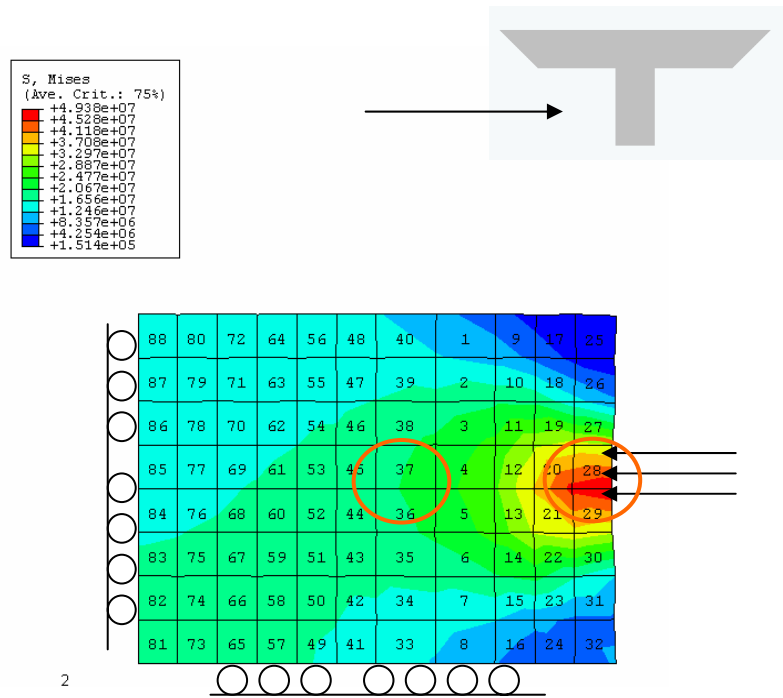


Figure 3.49. (a) Mises stress contour plot on side view of the deformed finger section, (b) plot of axial stress in element# 37 and element# 28 whose locations are marked in (a).

All experiments were performed at a nominal strain rate of 10^3 1/s. The experiments utilized a combination of fingers made from polycarbonate, aluminum, copper and steel. The shorthand al/al corresponds to a pair of aluminum fingers aligned in the longitudinal direction and a pair of aluminum finger in the transverse direction. Therefore, the pc/cu configuration stands for polycarbonate fingers used for longitudinal confinement and copper fingers used for transverse confinement. In all, 16 different configurations were employed. A graph of the axial stress as a function of the longitudinal confining stress is shown in Fig. 3.50. The figure indicates that the longitudinal stress does not have a large effect the axial strength of the material. The axial stress as a function of transverse stress is plotted in Fig. 3.51. This demonstrates that the transverse stress has a much greater effect on the axial strength of the material. This result concurs with the results from the low strain rate tests, which showed a much larger dependence on transverse strength on the axial strength of the composite. Finally, in Fig. 3.52, the transverse stress is plotted against the longitudinal stress. The graph shows that the longitudinal confinement does have an effect on the transverse stress of the material. This result also agrees with the lower strain rate results.

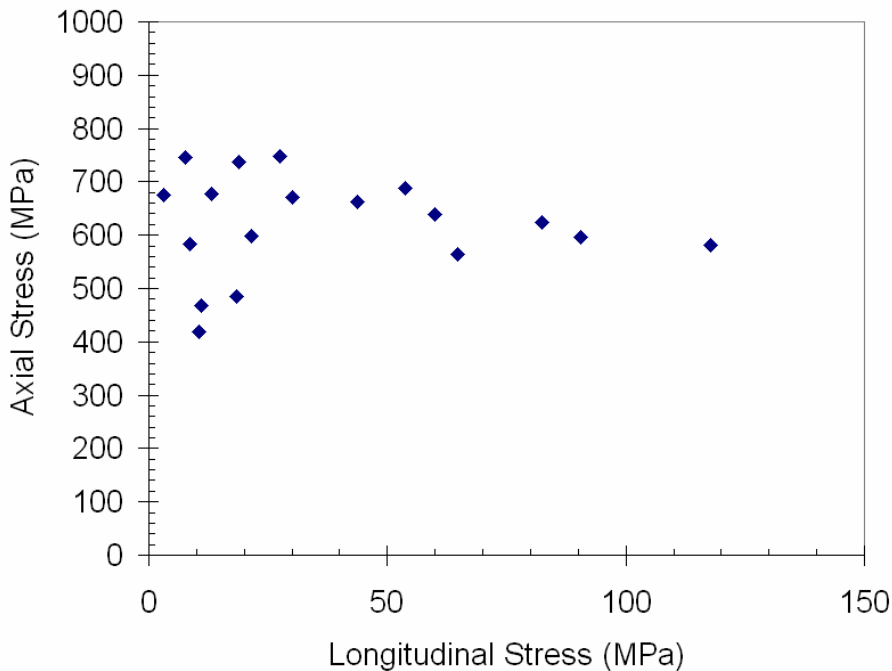


Figure 3.50. Axial Stress as a function of longitudinal confining stress.

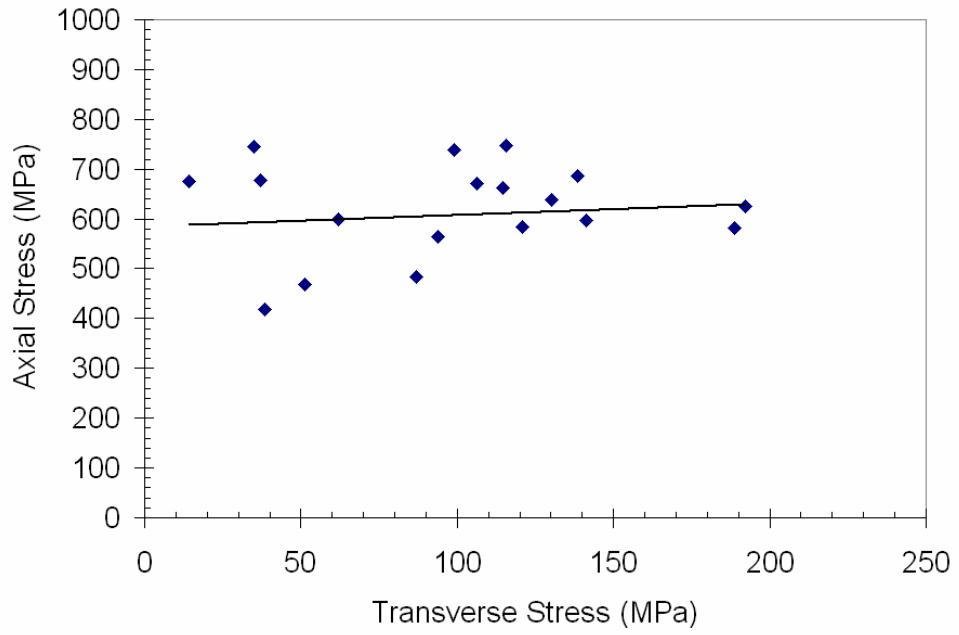


Figure 3.51. Axial Stress as a function of transverse confining stress.

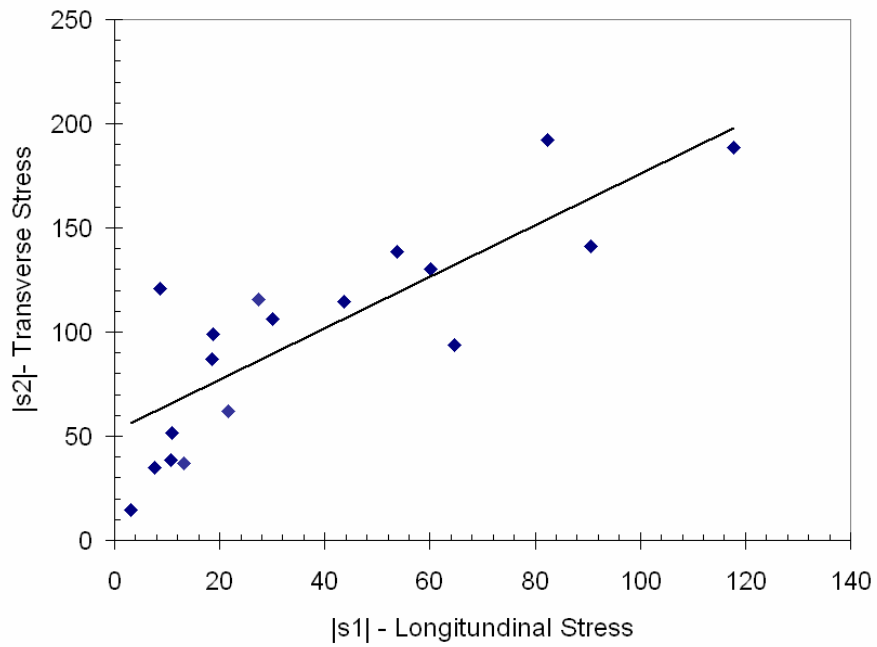


Figure 3.52. Transverse confining stress as a function of longitudinal confining stress.

3.10 Strain rate effect

Several experiments were performed with the al/al finger combination at strain rates varying from 1000 to 4000 1/s. These results, presented in Fig. 3.53, demonstrated that an increase in the strain rate produces an increase in the peak axial stress as well as failure strain.

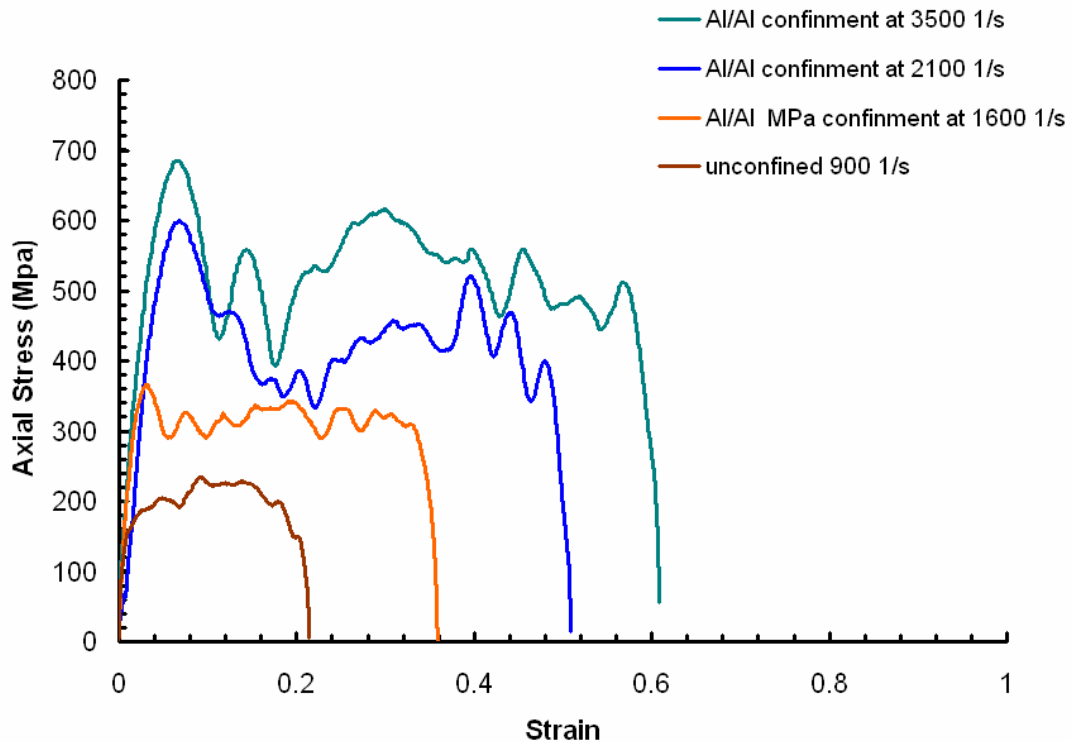


Figure 3.53. Stress-strain response of S2-glass/8552-epoxy unidirectional fiber composite for various confinements and strain rates.

Figure 3.34 shows the effect of strain rate and confinement on the maximum axial stress of the material. The failure strength has been plotted as function of strain rate and grouped based on nominally the same confinement. This graph shows that as the strain rate increases, the axial stress increases only moderately at a given confinement. Within the range of the experimental error, one could state that (i) the effect of strain rate on the

transverse strength of material is rather moderate and this effect is nearly independent of the level of confinement, i.e., the strain rate sensitivity is independent of the level of confinement and (ii) the level of confinement has a significant effect on the transverse strength of the composite, resulting in a nearly five-fold increase over the unconfined strength.

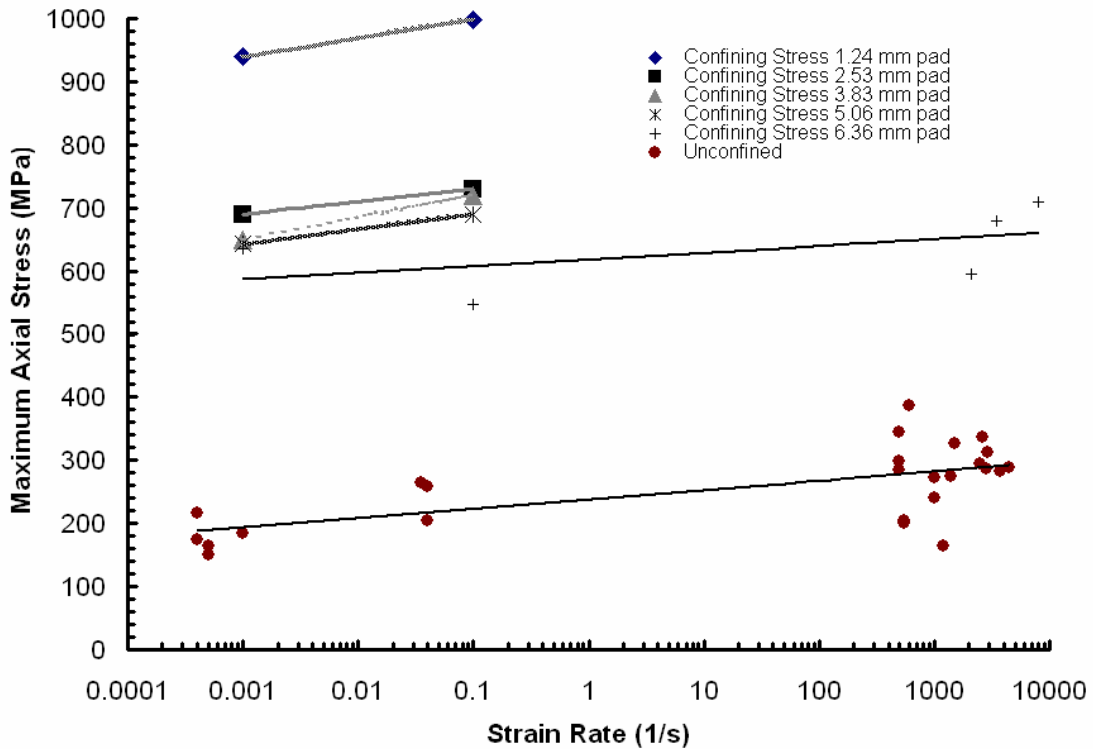


Figure 3.54. The effect of confinement and strain rate on the maximum axial stress (transverse strength) of the composite.

3.11. Summary

The quasi-static and dynamic response of the S2-glass/8552-epoxy unidirectionally fiber-reinforced composite has been studied under a wide range of confinements and strain rates. Two unique fixtures were developed to apply and measure longitudinal and transverse confinement stresses independently. The gathered experimental data was

compared with widely used phenomenological models. The low strain rate results indicated that the current failure models such as the Tsai-Wu and Christensen model act as lower and upper bounds to the failure of the material. The axial strength of the material was highly dependent on the transverse confinement. An increase in the longitudinal confinement was also found to increase the axial strength, but its effect was much less significant than the transverse confinement stress. The high strain rate results followed the same trend as the low strain rate results. The transverse confining stress had a much greater effect on the axial strength of the material in comparison to the longitudinal confining stress. Inspection of SEM micrographs of the post-mortem specimens suggested that the transverse failure of S2/8552 glass/epoxy localized in shear failure bands.

The confinement force on the sample was a reaction force to the axial loading of the material and not an applied force. For this reason, the experimental apparatus failed to explore the behavior of the composite under large longitudinal confinement. The expansion in the transverse direction was much greater than the longitudinal direction by an order of magnitude. In order to investigate the effect of large confinement in the longitudinal direction, an active loading system must be developed to apply pressure in the longitudinal fiber direction.

4. Summary and Future Work

4.1. Summary

This dissertation focused on the mechanical response and failure behavior of component materials of sandwich structures. The first part of the dissertation focused on cellular core materials such as PVC polymeric foams, while the second part was concerned with polymeric fiber-reinforced composites, namely a S2-glass/8552-epoxy unidirectional composite. In addition to developing new experimental techniques for investigating the mechanical behavior of these materials over a wide range of stress states and strain rates, the experimental results were analyzed in light of existing failure models.

4.1.1. Foam

The damage behavior in H-grade closed cell PVC foam was characterized using a newly developed *in-situ* ultrasonic measurement technique and a digital image correlation method. The ultrasonic technique developed for measurement of wave speeds in polymeric foams was able to capture the longitudinal and shear waves simultaneously. The ultrasonic method was validated by performing experiments on polycarbonate, aluminum, copper and steel samples to ensure the reliability and accuracy of the new method. Experiments were conducted on four foams with varying densities ranging from 130 to 250 kg/m³. The stress-strain response results of the experiments indicated that cell wall thickness governed the failure behavior of the material. The two lower density foams showed a sharp drop in apparent modulus during compression, while the two higher density foams showed a smooth decrease in apparent modulus under loading. A 2D hexagonal cell model was used to evaluate possible failure modes. It was determined that

the behavior of the apparent modulus in the two lower density foams corresponded to an elastic buckling failure mode, while the behavior of the two higher density foams corresponded to a plastic collapse type failure.

With the knowledge of the two potential local failure modes, predictions for the global failure behavior of each were developed. The elastic buckling behavior was expected to show rows of completely flattened cells, with neighboring cells remaining unaffected. In the case of the plastic collapse behavior, it was expected to show uniform cell deformation. A digital image correlation technique was employed to visualize the surface deformation of the foam. Imaging of the foam during deformation showed that the lower density foams with regions of large deformation surrounded by regions of very little deformation, while the higher density foam showed a more uniform deformation behavior. These results agreed with predictions made by the elastic buckling and plastic collapse models. The single cell model predicted a critical cell wall thickness of 15 μm . Foams with cell walls thinner than 15 μm were predicted to suffer from elastic buckling, while cells with walls thicker than 15 μm were to fail in a plastic collapse mode. Samples of each foam density were inspected using SEM. The micrographs revealed the lower density foams had cell wall thicknesses less than 15 μm , while the two higher density foams had wall thicknesses greater than 15 μm . Finally, ultrasonic measurements were coupled with DIC measurement; the results showed that drops in modulus corresponded directly with cell collapse in low-density foams. The type of failure behavior in foams becomes very significant when considering its use in sandwich structures. Non-uniform

deformation of foam core would induce stresses on the faceplate material. These effects could be strong enough to induce de-bonding in a sandwich structure.

4.1.2. Composite

The second half of the dissertation focused on the failure behavior of S2-8552 glass/epoxy composite under multi-axial loading. Specialized fixtures were developed, which were capable of measuring independently the 3 components of stress on the specimen. These fixtures were utilized in both low and high strain rate tests. Failure modes were characterized using optical and scanning electron microscopy, which revealed transverse failure occurring within localized bands. Based on the orientation of these bands, a Mohr-Coulomb failure criterion appears to be appropriate to describe the transverse failure of the composite. Experimental results were also compared with failure models developed by Tsai-Wu (1970) and Christensen (1997) and revealed that the existing models underestimate the strength of the material under multi-axial compression.

High strain rate experiments revealed similar behavior as compared to the low strain rate experiments, namely, that longitudinal confinement had a negligible effect on the axial strength of the material as opposed to the transverse confinement on the material. Within the high strain rate regime, data revealed that increasing strain rate resulted in a moderate increase in maximum failure stress as well as maximum strain.

This investigation introduced several novel experimental methods, which enabled the investigation of the mechanical behavior of foams and composite materials in greater detail. The development of *in-situ* ultrasonic measurement techniques provided the first measurement of wave speed in polymeric foams undergoing deformation. This method, in combination with a DIC technique, found that the 2D model of cell damage could be used

to predict the behavior of closed cell polymeric foams. For composites, previous work on the effect of multi-axial state of stress relied on experiments that superposed uniform hydrostatic pressure with uniaxial tension or compression and shear. The ability to independently measure the principal stresses of the composite provided quantitative measurements of the stresses in the material, at both low and high strain rates. This data also provided for comparison with current failure model predictions.

4.2. Recommendations for Future work

A predictive model incorporating the failure behavior of both composite and cellular materials to generate a failure envelope for sandwich structures should be a goal of future research. The development of such a model would require the investigation of the failure behavior of sandwich structures made with composite faceplates and foam cores of varying density. The experimental methods developed in this dissertation can be utilized for the study of sandwich structures. The digital image correlation method could be valuable for monitoring the behavior of the foam attached to the faceplates during deformation. Ultrasonic measurement during deformation could be conducted to monitor the wave speed during deformation to determine if damage mechanisms change due to the presence of faceplates.

The behavior of sandwich structures under multi-axial state of stress could be studied using the biaxial confinement fixtures developed in the previous study, for both quasi-static and dynamic tests. These data could be used to construct a failure envelope for sandwich structures. The shear failure behavior of sandwich structures could be studied using the digital image correlation method. This information is significant in that the foam

core carries most of the shear loading applied to a sandwich structure. In addition, a study on the energy absorption characteristics of sandwich structures due to the various failure mechanisms of the foam would provide valuable information on the protection the structure would offer.

Further investigation into the behavior of polymeric foams could involve the tracking of ultrasonic wave speed of foams under multi-axial loading. The ultrasonic fixture could be combined with the biaxial fixture such that wave speed measurements could be conducted while confinement stress was applied. These experiments could reveal new failure modes induced in the material under a combined stress state.

The characterization of composites could be extended in several ways. The range of the longitudinal confinement was limited due to the fact that confinement was indirectly applied as a reaction force to the axial loading of the material. In order to explore the effect of greater confinement in the longitudinal direction, an active system which can directly apply a force along the longitudinal axis is necessary.

It would be desirable that detailed analytical modeling and simulations to further develop the ability to predict failure modes in foams and composite materials over a wide range of stress states and strain rates. This is particularly warranted for fiber-reinforced composite materials, where a validated model development needs to take place with experiments on the same material system performed over the entire range of stress states and critically examined in light of existing failure models.

At the fifth symposium on naval structural mechanics held in 1967, Captain Jackson concluded that "A designer must be able to fashion a material to his needs with the assurance that everything is known beforehand about how the material actually performs

under a wide variety of environmental conditions and not merely how it *may* react or what its performance *could* be. Without this knowledge about it the material will not be accepted for use in the ships system.” (Jackson 1967) It can that be expected that sandwich structures will face the same scrutiny before being incorporated into ship systems. This sheds light on the need for continuing experimental research on both foams and composite materials to supply designers with models that will accurately predict their behavior.

BIBLIOGRAPHY

Abanto-Bueno, J. Lambros. J. "Investigation of crack growth in functionally graded materials using digital image correlation." *Eng. Frac. Mech.* Vol. 69 pp. 1695-1711 (2002)

Ashman, R.B., Antich, P.P., Gonzales, J., Anderson, J., Rho, J., "A comparison of reflection and transmission ultrasonic techniques for measurement of cancellous bone elasticity", *J. Biomechanics*, Vol. 27, No 9 pp 1195-1199, 1994

Ashman R. Corin, J. Turner, C., 1987 "Elastic Properties of Cancellous Bone Measurement by an Ultrasonic Technique," *J. Biomechanics*, Vol.20 No. 10, pp 979-986.

Basu, S. Waas, A., 2003 "Computational Modeling of Damage Growth in Composite Laminates" *AIAA Journal*, Vol 41. No. 6 pp. 1158-1166

Berndt H, Schniewind A P and Johnson G C 1999 "High resolution ultrasonic imaging of wood" *Wood Sci. Technol.* Vol. 33 pp. 185-98

Bruck, H.A., 2000. "A one-dimensional model for designing functionally graded materials to manage stress waves", *Int. J. Solids Struct.*, Vol. 37, pp. 6383-6395.

Bastawros A-F, Bart-Smith H, Evans AG. Experimental analysis of deformation mechanisms in a closed-cell Al alloy foam. *Journal of the Mechanics and Physics of Solids* 2000 Vol. 48 pp. 301-322.

Chevalier, J.L. "Sandwich core creep at 3 temperatures and fatigue properties of end-grain balsa and pvc", *Applying composites in the marine environment: overcoming barriers, setting standards, progressive learning*; Savannah, Georgia, November 8-10, 1993 C21-1, C21-21 1993

Christensen, R.M, 1979. "Mechanics of Composite Materials", Mineola: Dover Publications, Inc. pp199-221 (1979)

Christensen, R.M, 1997. Stress based yield/failure criteria for fiber composites. *Int. J. Solid Structures.* 34, 529-543

Daniel, I. M. and Tsai. C.L., 1991 "Analytical/Experimental Study of Cracking in Composite Laminates Under Biaxial Loading," *Composites Engineering*, Vol. 1, 1991 pp355-362

Daniel, I.M. and Ishai, O. 1994. "Engineering Mechanics of Composite Materials", New York: Oxford University Press, Inc., pp 108-129 (1994)

Daniel D. Imeokparia, Kyung W. Suh, William G. Stobby, Cellular Materials, Encyclopedia of Polymer Science and Technology, Complete rev. and update of 2nd ed, [New York] : John Wiley & Sons, Vol 5 pp 418-473 c2002

Davis NG, Teisen J, Schuh C, Dunand DC. "Solid-state foaming of titanium by superplastic expansion of argon-filled pores." J. Mater Res. 2001 Vol. 16, pp. 1508–1519.

Deka, M., "Air-Coupled Ultrasonic Transducer for NDE," *Ultrasonics Symposium, IEEE 1987*, pp. 543- 546

Edwards, Walt; Shah, Ashok C.; Mikofalvy, Bela; Cellular Plastics; Plastics engineering handbook of SPI, 4th ed, edited by Joel Frados, New York, Van Nostrand Reinhold, Chapter 20 Pp499-510, c1976

Firestone, F.A., 1940 "Flaw detection device and measuring instrument" USA-Patent # 2439130.

Freemantle R J and Challis R E 1998 Combined compression and shear wave ultrasonic measurements on curing adhesive *Meas. Sci. Technol.* 9 1291–302

Gioia, G., Wang, Y. and Cuitin~ o, A.M. (2001). The Energetics of Heterogeneous Deformation in Open-cell Solid Foams, In: Proceedings of the Royal Society of London, Series A. 457: 1079–1096.

Grandia, W.A.; Fortunko, C.M., "NDE applications of air-coupled ultrasonic transducers," *Ultrasonics Symposium, 1995. Proceedings., 1995 IEEE*, vol.1, no.pp.697-709 vol.1, 7-10 Nov 1995

Grosse. C., Weiler. B., Herb., A., Gunther S., Hofler, Kai., " Advances in ultrasonic testing of cementations materials" Institute of Construction Materials, University of Stuttgart

Grandia, W.A.; Fortunko, C.M., "NDE applications of air-coupled ultrasonic transducers," *Ultrasonics Symposium, 1995. Proceedings., 1995 IEEE*, vol.1, no.pp.697-709 vol.1, 7-10 Nov 1995

Gray, G.T. (200). Classic Split Hopkinson Bar Testing, ASM Handbook ASM international, Vol. 8, pp. 462-518, Metals Park, OH

Guilliorit E., Bacon C., Hosten B., Prediction of the Generation of Acoustic Waves due to the Penetration of Pulsed Microwaves in Multilayer Media.*Journal of the Acoustical Society of America*, Vol. 112, No. 1, pp. 65-74 (2002).

Hashin, Z., 1980. "Failure Criteria for Unidirectional Fiber Composites", J. of Applied Mechanics, Vol. 47, pp 329-334

Hashin, Z 1983 “Analysis of composite materials – a survey” J. of Applied Mechanics, Vol. 50 pp 481-505

Hiki, Y., ”Higher Order Elastic Constants of Solids,” Annual Review Material Science, Vol. 11, pp 51-73. (1981)

Jackson, L.L. “Ship System Constraints and Operational Requirement”, Proceedings of the Fifth Symposium on Naval Structural Mechanics, p19 (1967)

Kolsky, H. “An Investigation of Mechanical Properties of Materials at Very High Rates of Loading”, Proceedings of the Royal Society of London Series B62, 62: pp. 676-700. (1949)

Krautkramer,J., “Ultrasonic Testing of Materials”, Heidelberg, Springer-Verlag pp 1-61 1969

Laws, N., and Dvorack G.J., “Progressive Transverse Cracking in Composite Laminates,” J. of Composites Materials, Vol.22, 1998, pp 900-916

Lim, S.G., and Hong, C.S., 1989, “Predictions of Transverse cracking in composite laminates”, J. of Composite Materials, Vol. 23 pp 695-713

Neuschwandtner, G. S. Schwödauer, R. Vieytes, M. Bauer-Gogonea, S. S. Bauer, J. Hillenbrand, R. Kressmann, G. M. Sessler, M. Paajanen, and J. Lekkala, [Appl. Phys. Lett. 77, 3827 \(2000\)](#). [\[ISI\]](#)

Nikitin, K.E., 1983 “Ultrasonic Investigation of Specific Dislocation-structure characteristics in plastically deformed copper,” J. Ind. Lab., Vol. 49, No. 6, pp 620-624.

Oguni, K., Ravichandran, G. “A micromechanical failure model for unidirectional fiber-reinforced composites”, Int. J. of Solids and Structures, Vol.38 pp7215-7233 (2001)

O’Brien T.K. *et al*, 2001, “Influence of specimen preparation and specimen size on composite transverse tensile strength and scatter”, NASA /TM-2001-211030 ARL-TR-2540, pp. 1-80

O’Brien T.K. *et al*, 2001, “Analysis of ninety degree flexure tests for characterization of composite transverse tensile strength” NASA /TM-2001-211227 ARL-TR-2568, pp.1-53

O’Brien T.K. *et al*, 2001, “Transverse tension fatigue life characterization through flexure testing of composite materials” NASA/TM-2001-211035 ARL-TR-2544, pp. 1-68

Oguni. K. and Ravichandran G. “An Energy Based Model of Longitudinal Splitting in Unidirectional Splitting in Unidirectional Fiber-Reinforced Composites” J. of Applied Mechanics, Vol. 67, pp 437-443 (2000)

Overaker DW, Cuitiño AM, and Langrana NA (1998), Effects of morphology and orientation on the behavior of two-dimensional hexagonal foams and application in a re-entrant foam anchor model, *Mech. Mater.* **29**, 43–52

Papka, S.D., Kryriakides, S., “In-plane compressive response and crushing of honeycomb,” *J. Mech. Phys. Solids*. Vol. 42, No.10 pp 1499-1532, 1994

Peters WH, Ranson WF, “Digital image techniques in experimental stress analysis”, *Opt. Eng Vol.*, 21, (3), pp. 427-31 (1982)

Peters W.H., Ranson W.F., Sutton M.A., Chu T.C., Anderson J. “Application of digital image correlation methods to rigid body mechanics”, *Opt Eng Vol.* 22, (6), 738-42 (1983)

Pipes, R.B and Cole, B.W., “On the Off -Axis Strength Test for Anisotropic Materials” *J. of Composite Materials*, Vol. 7 pp246-256 (1973)

Rakow, J. F. ,Anthony M. Waas, [Size Effects in Metal Foam Cores for Sandwich Structures_ AIAA Journal](#) 2004 0001-1452 vol.42 no.7 pp. 1331-1337

Rakow, Joseph; Waas, Anthony “Thermal buckling of metal foam sandwich panels for actively cooled thermal protection systems” 45th AIAA/ASME/ASCE/AHS/ASC Structures, Structural Dynamics and Materials Conference; Palm Springs, CA; Apr. 19-22, (2004)

Rackers, B “Resin Transfer Moulding for Aerospace Structures edited by Kruckenberg T.”, London: Chapman & Hall pp. 1-24. (1998)

Rizzo, P. "Ultrasonic characterization and inspection of open cell foams." *Journal of engineering mechanics* Vol. 131. No.11 pp.1200-1208 (2005):

Sahnoune, A. *Ultrasonic Characterization and Rheology of Polymer Foams*. (1997).

Scheffler, M. (Editor), Paolo Colombo (Editor) “Cellular Ceramics: Structure, Manufacturing, Properties and Applications” 2005

Schmidt, W.W. “Foam filled composite sandwich structures for marine applications”, *Applying composites in the marine Environment: overcoming barriers, setting standards, progressive learning*; Savannah, Georgia, November 8-10, 1993 C21-1, C21-21 1993

Schultheisz, C.R., and Waas, A.M. (1996). Compressive failure of composites, part I: testing and micromechanical theories. *Progressive Aerospace Science* **32**, 1–42.

Steeves CA, Fleck NA. Collapse mechanisms of sandwich beams with composite faces and a foam core, loaded in three-point bending. Part II: experimental investigation and numerical modelling. *International Journal of Mechanical Sciences* 2004, in press, doi: 10.1016/j.ijmecsci.2004.04.004.

Sutton MA, Wolters WJ, Peters WH, Ranson WF, McNeill SR. Determination of displacements using an improved digital image correlation method. *Image Vision Comput* 1983;1(3):133-9

Suh, K.W. and Skochdopole, R.E., *Foamed Plastics*, Encyclopedia of Chemical Technology, Vol. 2, 3rd edn. Wiley, New York, 1980.

Talreja, R. 1985 “Transverse cracking and stiffness reduction in composite laminates,” *J. of composite Materials*, Vol. 19, 1985 pp 355-375

Tsai, C.L., and Daniel, I. M. 1992 “The Behavior of Cracked Crossply Laminate Under Shear Loading” *Int. J. Solids Structures*, Vol. 29, 1992 pp3251-3267

Tsai, S.W., Wu, E.M., 1971 A General Theory of Strength for anisotropic materials. *J. Composite Mater.* 5, 58-80.

Tsai, J.L. 2005. “Strain rate effect on in-plane shear strength of unidirectional polymeric composites.” *Fiber science and technology* Vol. 65 (13), pp 1941-1948.

Vaziri, Z. Xue, J.W. Hutchinson, “Metal Sandwich plates with polymer foam –filled cores.” *Journal of Mechanics of Materials and Structures*. Vol. 1 No. 1 (2006) pp95-125

Vural, M. and Ravichandran G. “Transverse failure in thick S2-Glass/epoxy fiber-reinforced composites”, *J. of Composite Materials*, Vol 38, No. 7/2004

Vural, M. 2005 “Dynamic Compressive Failure of Unidirectional Fiber-Reinforced Composites”

Walter, M.E. and Ravichandran, G. 1995 “An Experimental Investigation of Damage Evolution in a Ceramic Matrix Composite” *J. of Engineering Materials and Technology*, Vol 117 pp 101-108

Waas, A.M., and Schultheisz, C.R., (1996). Compressive failure of composites, part II: experimental studies. *Progressive of Aerospace Science* **32**, 43–78.

Wang, Y. and Cuitino, A.M. (2002). Full-field measurements of heterogeneous deformation patterns on polymeric foams using digital image correlation. *International Journal Solids and Structures*, 39(13–14), 3777–3796.

Winsom, M.R. 1999 “Size effects in the testing of fiber-composite materials” *Composites Science and Technology*, Vol. 59 pp 1937-1957

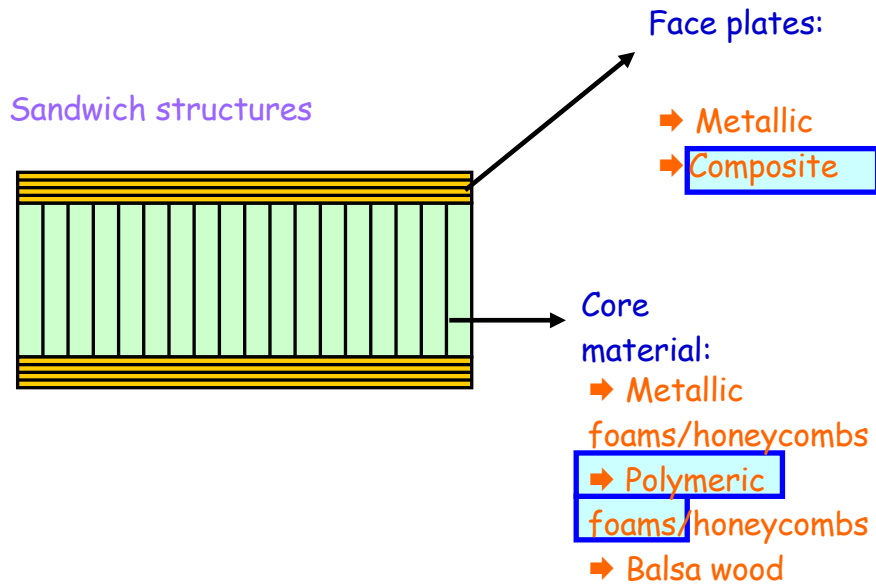
Weaire, D., Fortes, M.A., “Stress and Strain in liquid and solid foams”, *Advances in Physics* Vol 43 No 6 pp685-738 1994

Yerramalli, A., *et al.*, 2004, "A Nondimensional Number to Classify Composite Compressive Failure", *J. of Applied Mechanics*, Vol. 71, pp. 1-7

Zettl, B., Mayer, H., Stanzl-Tschegg, S. E., and Degischer, H. P., 2000, "Fatigue Properties of Aluminum Foams at High Numbers of Cycles," [Mater. Sci. Eng., A, 292, pp. 1-7.](#)

Zinoviev, P.A. Tsvetkov, S.V., Kulish, G.G., Berg, R. (2001) "The behavior of high strength unidirectional composites under tension with superimposed hydrostatic pressure" *Composite Science and Technology*, Vol. 61 pp 1151-1161

Appendix A- Sandwich Structures



E_{face} = Elastic modulus of the face plate
 E_{core} = Elastic modulus of the core
 b = Width of the beam
 d = Distance between face plate and centroid
 t = Thickness of face plate
 c = Thickness of core

$$D = EI = \frac{E_{face}bt^3}{6} + \frac{E_{face}btd^2}{2} + \frac{E_{core}bc^3}{12} \quad \text{Eq. A}$$

if $d/t > 6$
 $E_{face}/E_{core} td^2/c^3 > 17$

Equation A becomes

$$D = EI = \frac{E_{face}btd^2}{2} \quad \text{Eq. B}$$

The equation shows that the core material does not contribute to the stiffness of the beam but it does carry the shear loading. (Gundberg)

Appendix B-Biaxial Experimental Set Up

Figure A shows a diagram of the experimental apparatus with the fixture on the left. Two leads, one from each strain gauge, were connected to the Wheatstone bridge. The output was then channeled through an amplifier set to a gain of 100, after which the signal was read and recorded by the computer. The power supply provided the Wheatstone bridge with 10V DC. Several operations had to be performed on the raw data to convert the voltage output from the strain gauges to the confining stress. First, the output was divided by 100 to correct for the amplifier gain. Using Equation A, this corrected voltage output (V_{output}) was converted to a strain.

$$\varepsilon_{finger} = \frac{V_{output} * 4}{GF * V_{in}} \quad \text{Eq A}$$

The conversion calculation required the power source input voltage to the Wheatstone bridge (V_{in}) and the gauge factor. The gauge factor (GF) of the strain gauge was read from its packaging, which also provided the calibration information of the gauge. Multiplying the strain by the Young's Modulus of the finger (E_{finger}) yielded the stress in the finger, as shown below in equation B.

$$\sigma_{finger} = E_{finger} * \varepsilon_{finger} \quad \text{Eq 3.B}$$

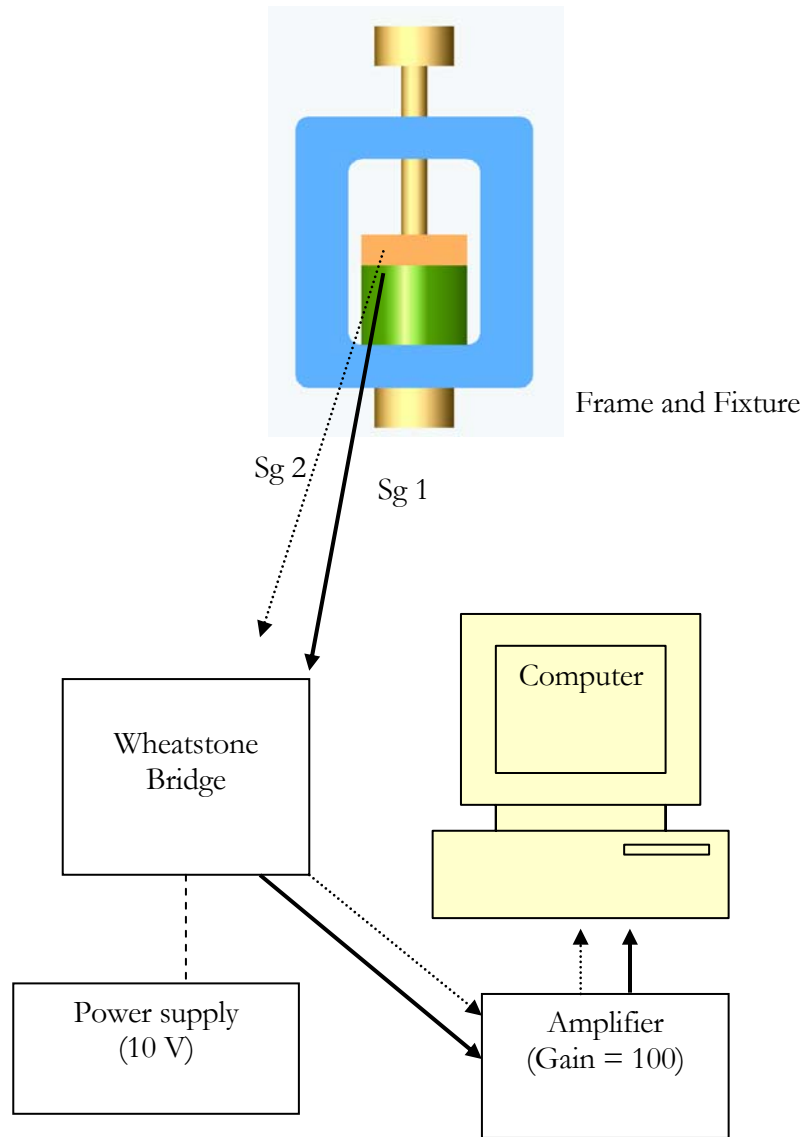


Figure A. Experimental Setup showing strain gauge input to Wheatstone bridge, amplifier and computer

In order to calculate the stress in the finger accurately, ultrasonic measurements were used to determine the Young's modulus of the finger (E_{finger}). Both the longitudinal and

shear wave transit times (t_d and t_s , respectively), as well as the height and density of the sample are necessary to calculate the value of the Young's modulus of the material correctly. Table A displays these data, along with the resulting modulus (E) calculated using Eq. C. These values were used in Eq. B to calculate the stress in the fingers.

$$E = \rho h^2 \left(\frac{4t_d^2 - 3t_s^2}{t_d^2 - t_s^2} \right) \quad \text{Eq. C}$$

Table A. Table of Specimen dimension, height, longitudinal and shear wave speed and calculated Youngs Modulus

Specimen	Density (kg/m ³)	Height (mm)	t_d (μs)	t_s (μs)	E (GPa)
Polycarbonate	1197.411	9.33	3.998	9.758	3.04
Aluminum	2627.788	9.49	1.458	2.998	67.98
Copper	8877.241	9.51	2.018	4.178	120.60
Maraging Steel	8078.02	9.54	1.598	3.178	185.75